A Group Theoretical Symmetry Filter For Improved Subsurface Imaging

A Thesis Presented

To the Faculty of Graduate Studies

By

Michael Charles Phelan

In Partial Fulfillment

of the Requirements for the Degree of

Masters of Science in Electrical Engineering

University of Manitoba

Winnipeg, Manitoba, Canada

December 2003

THE UNIVERSITY OF MANITOBA

FACULTY OF GRADUATE STUDIES
*****
COPYRIGHT PERMISSION

A Group Theoretical Symmetry Filter for Improved Subsurface Imaging

BY

Michael Charles Phelan

A Thesis/Practicum submitted to the Faculty of Graduate Studies of The University of Manitoba in partial fulfillment of the requirement of the degree

Of

MASTER OF SCIENCE

Abstract

Subsurface GPR imaging of landmines for the purpose of detection is a very challenging problem due to the inherent complications in deciphering landmines from surrounding clutter, such as rocks, shrapnel and various other electromagnetic inhomogeneities. What is more, landmines are manufactured in a plethora of sizes and shapes and can be constructed from a variety of materials and explosives. These factors make it difficult to establish a reliable feature that can be used to differentiate landmines from their surroundings. There is one feature that many landmines possess that clutter in general does not: spatial symmetry. The ergonomics of mass production often dictate that it is simpler and cheaper to manufacture objects that possess some form of geometric (spatial) symmetry and the manufacturing of landmines is no exception. In this thesis, the principles of group theory are used in conjunction with electromagnetic theory to exploit the geometric symmetry of mine-like targets and their scattered electromagnetic fields. A novel subsurface imaging algorithm in the form of a symmetry filter is proposed that takes advantage of target symmetry to enhance subsurface images of symmetric targets. The effectiveness of the algorithm is shown through a series of real GPR measurements in a controlled environment. The results show that symmetry can be used as an effective feature to enhance GPR images to discriminate landmines from natural and manmade clutter in the subsurface.

Keywords: Ground penetrating radar, subsurface imaging, group theory, symmetry, object recognition, landmine detection, synthetic aperture radar.

Acknowledgements

The author would like to thank his research advisor Dr. Joe Lovetri for his encouragement, guidance, patience and his commitment to this project. This research would not have been possible without his suggestions and criticisms. Many thanks to Dr. Gabriel Thomas for his help on signal processing matters. Thanks are given to Eduardo Corral and Su Hong for their work on establishing a suitable measurement system and to Scott Peters and Arturo Solis for their help in implementing the control circuits for the stepper-motor. "Mucho gracias" to Daniel Flores for his aid in matters regarding data acquisition. And finally, a round of thanks to the department of Electrical and Computer Engineering for supplying necessary materials and help.

Dedication

To Галина.

Moi je t'offrirai
Des perles de pluie
Venues de pays
Où il ne pleut pas
Je creuserai la terre
Jusqu'après ma mort
Pour couvrir ton corps
D'or et de lumière
Je ferai un domaine
Où l'amour sera roi
Où l'amour sera loi
Où tu seras reine...
(Brel)

Table of Contents

Table of Figures

CHAPTER 1
Introduction and Motivation

1.1 The Landmine problem

The global landmine crisis is one of the most pervasive problems facing the world today. It is estimated that there are between 45 and 50 million landmines in the ground in at least 70 countries. Landmines reportedly maim or kill 10,000 civilians every year. Those victims that survive endure a lifetime of physical, psychological, and economic hardship.

Figure 1.1 Various landmines and other unexploded ordinance [1]

1.2 GPR and SAR in Landmine Detection

Ground penetrating radar (GPR) extracts electromagnetic information from subsurface objects by measuring the scattered electromagnetic radiation from obstacles in the radar beam's path. Electromagnetic scattering occurs as a result of boundary conditions being satisfied by Maxwell's equations at the boundaries that define the scattering object and the surrounding medium. A subsurface target such as a landmine will possess given electromagnetic properties which will generally be different from the electromagnetic properties of the surrounding medium, in this case the earth. It is the requirement of the validity of Maxwell's equations at the geometric and electromagnetic discontinuity at the target/medium boundary that gives rise to both transmitted and reflected fields.

The basic topology of a GPR system requires two antennae arranged in a bistatic transmitting and receiving capacity at or near the ground surface in a ground-coupled configuration as shown in Figure 1.2. Individual measurements at discrete locations yield information pertaining to target range from the antenna network. In order to generate target information in more than one spatial dimension, further measurements along a path must be recorded at predetermined locations. When radar measurements are taken in such a manner, the recorded data may be subjected to a post-processing procedure whereby the spatial measurements together may be combined to form a synthetic aperture. Synthetic aperture radar (SAR) is a well documented method of providing radar resolution in the cross-range (along the path of the radar) without having to resort to large, bulky physical arrays of antennae [2]. The radar system implemented to take readings in this thesis is a bistatic stepped frequency continuous wave (SFCW) system designed and developed at the University of Manitoba.

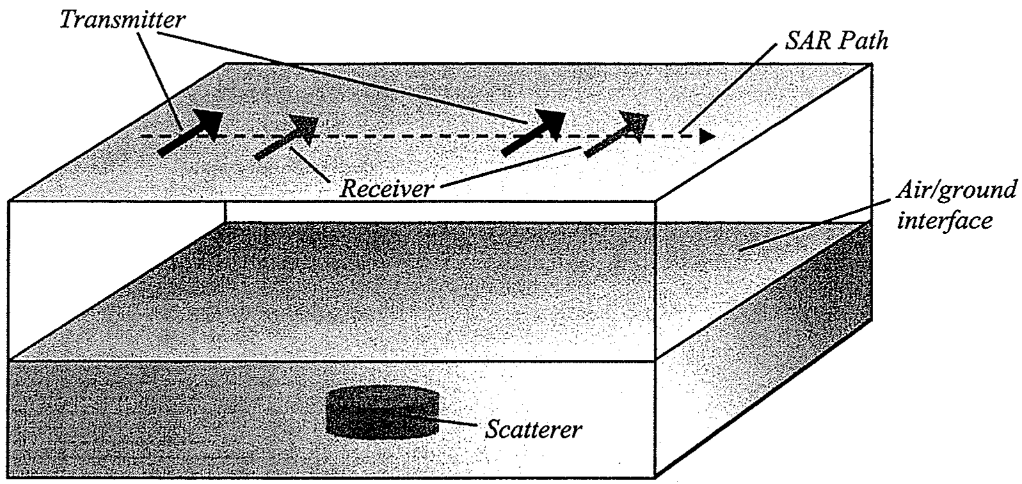

Figure 1.2 Typical setup for a bistatic GPR network for SAR applications

1.2.1 Radar Target Reconstruction, Identification and Classification

At microwave frequencies, scattering can be very complicated and the resulting scattering patterns can be extremely convoluted and disparate with respect to the target's physical geometry. The Uniqueness Theorem of classical electromagnetics stipulates that the forward scattering problem is unique given a fixed geometry and radar scattering source [3]. Unfortunately, the inverse scattering problem is in general not so straightforward and many attempts have been made to resolve the ill-posedness of the inverse scattering problem [4] [5] [6]. Many very complicated and computationally expensive algorithms involving, among other things, optimization with large matrices have been developed. The repercussions of the non uniqueness is that although a given scatterer illuminated by a given field will exhibit a single, unique scattering response, knowledge of the scattered electromagnetic field is in general not sufficient to determine the exact scattering object.

In order to effect target identification without having to perform the lengthy process of inversion, the scattered response of the target must be known a priori so that identification algorithms can assess the correlation between what is observed and what is known about the target in advance. Some very innovative identification algorithms have been developed that make use of measured or calculated scattering information to recognize the identity of subsurface targets [7] [8]. The seemingly unavoidable problem faced by any target identification system, however, is the enormous diversity in landmine target responses owing to the vast number of types of landmines that have been, or are being produced. Moreover, the scattering response from landmines is dependent on the highly variable environmental conditions such as type of soil, moisture and surface roughness of the earth in which the landmines are buried in. It can be seen that the possibilities are virtually endless for subsurface landmine scattering responses. Given these realities, a system capable of landmine classification, rather than identification might be more feasible. This is to say that a more sensible method of achieving landmine clearance might not lie in the identification of specific landmines through identification algorithms designed to recognize specific landmines but rather in a scheme designed simply to designate a target as a landmine (of no particular variety) or as clutter (of no particular interest).

1.3 Motivation For Using Symmetry As A Discriminant

The task of applying GPR for landmine detection is a precarious one; there is little room for mistakes since failure to identify a target can have lethal repercussions. It is because of these lethal repercussions that GPR systems for landmine detection must always err on the side of caution. The required probability of detection is virtually 100%. This demanding specification can unfortunately lead to undesirably high false-alarm rates due to shell-casings, rocks and other sources of clutter which seriously impedes progress in mine clearance operations. False-alarm ratios of 100:1 to 1000:1 are not uncommon in mine clearance and because of this, clearance operations can be painfully slow [9]. A scattering response common to virtually all landmines but distinct from almost all clutter would be valuable in the effort to develop an efficient landmine detection algorithm. If such a distinct response (discriminant) were made available, a processor independent of mine variety could be implemented.

Recently, a target scattering discriminant that is in fact unique to landmines has been discovered; geometric symmetry of the target. The argument for geometric symmetry as a target discriminant is an ergonomic one; geometric symmetry can be associated with objects produced by human beings. There are various reasons for this ergonomic reality including ease of fabrication and storage, simplicity of analysis (by the designer/fabricator) and performance characteristics such as aerodynamic/hydrodynamic properties and detonation and fragmentation pattern. Given these realities a functional hypothesis may be made in the form of an implication[10]:

$$\begin{aligned} \textit{Symmetry in target} &\rightleftharpoons \textit{Man made object} \\ &\rightleftharpoons \textit{Further investigation} \end{aligned} \tag{1.1}$$

The two-way equivalence connotes that a perceived lack of symmetry is equivalent to the inverse hypothesis that asymmetrical targets are naturally occurring (therefore not a landmine) and do not warrant further investigation.

The hypothesis indicated in (1.1) and its inverse should not be taken to signify that symmetry implies a landmine, since it is not inconceivable for symmetrical geometries to occur randomly in nature. Some possible naturally occurring symmetrical targets include animal shells, bird eggs and particularly nearly symmetrical geological objects such as rocks that may by chance exhibit some form of symmetry.

1.4 Thesis Outline

The purpose of this thesis is to set out the means to employ the existence of geometric symmetry in a scatterer as a method to improve GPR classification of landmines by enhancing radar images of symmetrical scatterers while suppressing images of non-symmetrical scatterers. It is because of this symmetry enhancement/suppression rationale that the resulting system may be considered a "symmetry filter". In order to develop and implement such a method, several founding principles on radar, Fourier imaging and symmetry must be discussed. Once these principles have been laid down, they will be exploited in a new algorithm to achieve the goals of this research. Once implemented, several experiments will be carried out to validate the hypothesis and to test the algorithm on real data collected in a controlled environment at the University of Manitoba. The path taken, chapter by chapter will proceed thusly:

Chapter 2: The Physics of GPR and Radar Imaging

In this chapter a brief description of fundamental GPR principles will precede a more in-depth mathematical discussion of the finer details of scattering and imaging radar in terms of the available mathematical, electromagnetic and signal processing tools such as Maxwell's equations and Fourier analysis.

Chapter 3: Symmetry and Group Theory

The principle of symmetry is alive and in use in many aspects of daily life in a plethora of seemingly unrelated domains such as art, architecture and music. These institutions have their own set of rules and guidelines for analysing and employing symmetry to various ends, however, in this thesis we are strictly concerned with the notion of symmetry as a mathematical tool and as such a set of mathematical rules for investigating symmetry are required. These tools come under the guise of a branch of abstract algebra called Group theory. Chapter 3 will be an introduction to Group theoretical notions of symmetry as required to serve to purposes of this research.

Chapter 4: Target Symmetry and the Scattering Dyadic

Chapter 4 is dedicated to relating the concepts of Group theory to classical electromagnetic scattering in order to bridge the notions of target symmetry and scattering symmetry. Rigorous mathematical arguments will be given to show that geometric symmetry in a scattering target can in fact make itself available as an electromagnetic response. It is this "symmetry" response that we are interested in. It will be shown that geometrical symmetry can translate to symmetry in the scattering dyadic. This symmetry information is maintained through the application of the temporal Fourier transform. This is important because all measurements will be obtained in the frequency domain.

Chapter 5: Symmetry Filter Algorithm

The final stage of the theoretical campaign is to seize the knowledge developed in Group theory, electromagnetic scattering and Fourier imaging and use these foundations to construct a working algorithm that makes use of target symmetry to filter unsymmetrical scatterers and enhance symmetrical targets in radar images. In order to accomplish this task, a method must be developed that will allow the otherwise abstract notion of symmetry to be exploited in a mathematical algorithm. A means must be found to make symmetry both observable and measurable. This implies that the target symmetry information contained in the scattered fields must be accessible and quantifiable. In this chapter, a scheme for both measuring and quantifying target symmetry is developed. This algorithm is then implemented in a custom designed radar image signal processing algorithm to complete the symmetry filtering in the range domain. The end result will be an image that clearly exhibits symmetrical targets which should be investigated further for the presence of a landmine while suppressing unwanted clutter that would otherwise obscure the image.

Chapter 6: Experiments and Results

The efficacy of the symmetry filter algorithm is put to the test in this chapter where various experiments are undertaken to simulate a variety of different problems that may occur in GPR measurements. First the algorithm is implemented for strongly reflective targets in order to gain a sense of how it behaves for symmetric and asymmetric targets. Other more complex experiments follow to validate the method in more realistic scenarios.

Chapter 7: Conclusions

The final chapter of the thesis will summarize the theory and development of the proposed symmetry filter. The major results and findings will be discussed and several issues and complications will be studied. The implications of the research in a more general context are considered and the possibilities for future research on this topic will be outlined.

CHAPTER 2
The Physics of GPR and Radar Imaging

2.1 Introduction to GPR and RADAR

GPR senses electromagnetic inhomogeneities, for example, by the conductive contrast of a metallic mine in the presence of a far-less-conducting soil background. A more difficult problem is to sense the electrical contrast caused by a dielectric (plastic/explosive) landmine buried in a ground-like medium. Often this contrast is very weak, implying that the landmine GPR signature is very small. The problem is exacerbated by the fact that there are many electrical contrasts that may exist in the landmine problem, which significantly complicates detection. For example, the largest contrast typically exists at the air/ground interface and therefore GPR is typically characterized by a very large reflection at this interface. If a landmine is buried at a shallow depth, and the available bandwidth provides limited resolution, the often weak landmine signature will be lost in the very strong ground reflection signature. This implies that bandwidth (resolution) plays an important role in defining the target depths at which a landmine may be observed by GPR. We also note that natural subsurface inhomogeneities, such as rocks, roots, surface roughness, and soil heterogeneity (e.g., pockets of wet soil), also yield a signature to a GPR sensor; such clutter represents the principal source of false alarms. In conflict zones, where landmines are all too often found, another significant source of clutter are the usual remnants of war such as shrapnel, shell casings and the like.

The major design variable in a GPR system is the frequency and bandwidth of operation. The scale at which GPR can detect objects is proportional to the wavelength of the radar signal in the medium of propagation, so the quality of the image improves as the wavelength decreases and the frequency increases. However, at high frequencies, penetration of the incident wave into the soil can be poor. As a result, the designer must make a tradeoff between quality of the image and required penetration depth. The optimal design for maximizing image quality while ensuring sufficient depth of penetration changes with environmental conditions such as soil type, mine size, and mine position. Also critical in the design of a GPR system are signal-processing algorithms, which filter out clutter signals and make the job of target identification more straightforward. The main concern of this thesis is a new form of post-processing that exploits special symmetry in the scattered fields to enhance GPR images of landmines in order to identify them.

GPR has a number of advantages relative to other available subsurface imaging technologies. Rather than characterizing its response solely on the basis of metal content, as is the case in conventional electromagnetic induction metal detection, GPR can sense contrast in dielectric medium and therefore possesses the capacity to detect landmines that are entirely made of plastic (no metal). Also with recent advances in the development of microwave technology and antenna technology, GPR systems are relatively inexpensive to construct and the possibility of manual portability is not excluded [11].

The major drawback with current GPR technology is the difficulty in differentiating mine from clutter in conditions where inhomogeneities (natural or otherwise) are prevalent. GPR performance is highly sensitive to soil moisture, smoothness of the ground and the consistency of the ground medium. Flora, fauna and insects in a given environment create further undue hardships in discerning landmines from the surrounding medium.

There are many concepts at work in radar imaging and the goal of this chapter is to introduce some of the mathematical and physical principles of GPR. Specifically, the principles of electromagnetic scattering and radar imaging and the required mathematical background to comprehend these principles will be reviewed.

2.2 Dyadic Analysis

2.2.1 Introduction to Dyadics

Dyadic algebra is a convenient device contrived for situations where vectors in a given orthogonal basis prescribed in three dimensional Euclidean space $\mathbb{R}^3$ need be mapped by means of a linear transformation to another orthogonal basis in $\mathbb{R}^3$ [12]. For electromagnetic radar problems where linear transformations between sources and fields are often necessary, dyadic notation can be very useful. Stated in the language of linear algebra, a dyadic is a matrix operator in $\mathbb{R}^3$ that maps the tangential component of the induced surface field in a given coordinate basis to the scattered field in a different coordinate basis. In the language of tensor analysis, scalars and vectors may be considered as tensors of rank zero and one respectively, while a dyadic may be considered a tensor of second rank. This implies that electromagnetic scattering may be considered as a second rank tensor transformation from a tensor element of first rank (i.e. an incident vector field) to another tensor element of first rank (i.e. a scattered vector field). The main advantage of dyadic notation is that the basis vectors in $\mathbb{R}^3$ of the incident and transformed (scattered) fields may be chosen arbitrarily to coincide with the physical problem at hand in a most convenient way. In fact, it will be shown in section 2.5 that by making use of dyadic algebra, it is possible to construct a single dyadic representation of a scattering object that contains all of the target's scattering information in one neat package [13].

Consider two vectors $\vec{\mathbf{A}}$ and $\vec{\mathbf{B}}$ in the three-dimensional Euclidean space R^3 with basis $B^3 = \langle \hat{e}_1, \hat{e}_2, \hat{e}_3 \rangle$ in the space then in vector notation

$$\vec{\mathbf{A}} = \hat{\mathbf{e}}_1 a_1 + \hat{\mathbf{e}}_2 a_2 + \hat{\mathbf{e}}_3 a_3, \tag{2.1}$$

$$\vec{\mathbf{B}} = \hat{\mathbf{e}}_1 b_1 + \hat{\mathbf{e}}_2 b_2 + \hat{\mathbf{e}}_3 b_3. \tag{2.2}$$

The vectors may also be represented in matrix form as

$$\overleftarrow{\mathbf{A}} = \begin{pmatrix} a_1 \\ a_2 \\ a_3 \end{pmatrix}, \qquad \overleftarrow{\mathbf{B}} = \begin{pmatrix} b_1 \\ b_2 \\ b_3 \end{pmatrix}. \tag{2.3}$$

The inner (scalar) product of these vectors is denoted as

$$\vec{\mathbf{A}} \cdot \vec{\mathbf{B}} = \overleftarrow{\mathbf{A}}^T \overleftarrow{\mathbf{B}} = a_1 b_1 + a_2 b_2 + a_3 b_3. \tag{2.4}$$

Suppose that $\vec{\mathbf{A}}$ is to be mapped linearly to $\vec{\mathbf{B}}$ by means of a matrix transformation. In R^3 such a transformation consists of a 3×3 matrix $\overleftarrow{\mathbf{C}}$ where

$$\overleftarrow{\mathbf{C}} = \begin{pmatrix} c_{11} & c_{12} & c_{13} \\ c_{21} & c_{22} & c_{23} \\ c_{31} & c_{32} & c_{33} \end{pmatrix}. \tag{2.5}$$

In *dyadic notation* the transformation matrix $\overleftarrow{\mathbf{C}}$ is denoted $\overline{\overline{\mathbf{C}}}$. It is considered to be a tensor of second rank and the relationship is expressed as

$$\vec{\mathbf{B}} = \overline{\overline{\mathbf{C}}} \bullet \vec{\mathbf{A}} . \tag{2.6}$$

Like a vector, a dyadic is defined and has meaning independently of any basis in the vector space. And like a vector, it may be represented with reference to a specific basis. With respect to the Euclidean vector space B^3, $\overline{\overline{\mathbf{C}}}$ is represented as

$$\begin{aligned} \overline{\overline{\mathbf{C}}} &= \sum_{m=1}^{3} \sum_{n=1}^{3} c_{mn} \hat{\mathbf{e}}_m \hat{\mathbf{e}}_n \\ &= c_{11} \hat{\mathbf{e}}_1 \hat{\mathbf{e}}_1 + c_{12} \hat{\mathbf{e}}_1 \hat{\mathbf{e}}_2 + c_{13} \hat{\mathbf{e}}_1 \hat{\mathbf{e}}_3 \\ &+ c_{21} \hat{\mathbf{e}}_2 \hat{\mathbf{e}}_1 + c_{22} \hat{\mathbf{e}}_2 \hat{\mathbf{e}}_2 + c_{23} \hat{\mathbf{e}}_2 \hat{\mathbf{e}}_3 \\ &+ c_{31} \hat{\mathbf{e}}_3 \hat{\mathbf{e}}_1 + c_{32} \hat{\mathbf{e}}_3 \hat{\mathbf{e}}_2 + c_{33} \hat{\mathbf{e}}_3 \hat{\mathbf{e}}_3 \end{aligned} , \tag{2.7}$$

where it should be noted that there is no vector operator between the unit vector elements in the dyadic. Instead, the dyadic is defined by the juxtaposition of two vectors $\hat{\mathbf{e}}_m \hat{\mathbf{e}}_n$ consisting of an *anterior* vector $\hat{\mathbf{e}}_m$ and a *posterior* vector $\hat{\mathbf{e}}_n$. This notation implies that the dyadic does not in fact represent a physical quantity, but is in fact an operator that represents a mapping [14].

Using this notation, it is possible to determine the algebra of a dyadic mapping of a vector to another vector. When the dyadic $\overline{\overline{\mathbf{C}}}$ is the anterior element of the inner product with **A** as in (2.6), the elements of $\overline{\overline{\mathbf{C}}}$ can be re-ordered to facilitate the calculation

$$\begin{aligned} \overline{\overline{\mathbf{C}}} &= \sum_{m=1}^{3} \hat{\mathbf{e}}_m \left(\sum_{n=1}^{3} c_{mn} \hat{\mathbf{e}}_n \right) \\ &= \hat{\mathbf{e}}_1 \left(c_{11} \hat{\mathbf{e}}_1 + c_{12} \hat{\mathbf{e}}_2 + c_{13} \hat{\mathbf{e}}_3 \right) \\ &+ \hat{\mathbf{e}}_2 \left(c_{21} \hat{\mathbf{e}}_1 + c_{22} \hat{\mathbf{e}}_2 + c_{23} \hat{\mathbf{e}}_3 \right) \\ &+ \hat{\mathbf{e}}_3 \left(c_{31} \hat{\mathbf{e}}_1 + c_{32} \hat{\mathbf{e}}_2 + c_{33} \hat{\mathbf{e}}_3 \right) \end{aligned} . \tag{2.8}$$

The calculation of the inner product can then proceed as follows

$$
\begin{aligned}
\vec{\mathbf{B}} &= \overline{\overline{\mathbf{C}}}\bullet\vec{\mathbf{A}} \\
&= \hat{\mathbf{e}}_1\left(c_{11}\hat{\mathbf{e}}_1 + c_{12}\hat{\mathbf{e}}_2 + c_{13}\hat{\mathbf{e}}_3\right)\bullet\vec{\mathbf{A}} \\
&\quad + \hat{\mathbf{e}}_2\left(c_{21}\hat{\mathbf{e}}_1 + c_{22}\hat{\mathbf{e}}_2 + c_{23}\hat{\mathbf{e}}_3\right)\bullet\vec{\mathbf{A}} \\
&\quad + \hat{\mathbf{e}}_3\left(c_{31}\hat{\mathbf{e}}_1 + c_{32}\hat{\mathbf{e}}_2 + c_{33}\hat{\mathbf{e}}_3\right)\bullet\vec{\mathbf{A}} \\
&= \hat{\mathbf{e}}_1\left(c_{11}a_1 + c_{12}a_2 + c_{12}a_3\right) \\
&\quad + \hat{\mathbf{e}}_2\left(c_{21}a_1 + c_{22}a_2 + c_{32}a_3\right) \\
&\quad + \hat{\mathbf{e}}_3\left(c_{31}a_1 + c_{32}a_2 + c_{33}a_3\right)
\end{aligned}
\tag{2.9}
$$

This representation of a posterior dyadic inner product (where the vector is to the right of the dyadic) is particularly telling since it shows that in the mapping of $\vec{\mathbf{A}}$ to $\vec{\mathbf{B}}$, each vector element of $\vec{\mathbf{A}}$ is operated on by three individual vector elements.

2.2.2 Properties of Dyadics

Since dyadic algebra can be considered to be a method that linearly maps a vector to another vector, it is not surprising that many concepts in dyadic analysis are similar to matrix algebra. Some of these concepts include non-commutativity and the existence of an identity element. Furthermore, several operations applicable in vector algebra are available in dyadic analysis such as the divergence and curl relationships.

Using (2.7) it is easy to show the non-commutative nature of dyadics in the inner product,

$$
\overline{\overline{\mathbf{C}}}\bullet\vec{\mathbf{A}} \neq \vec{\mathbf{A}}\bullet\overline{\overline{\mathbf{C}}}
\tag{2.10}
$$

The *idemfactor*, denoted $\overline{\overline{\mathbf{I}}}$, is a unit dyadic that corresponds to the identity matrix with reference to a given vector basis in matrix algebra and its inner product with a vector or dyadic leaves the vector or dyadic unchanged. In R^3 the idemfactor is

$$\overline{\overline{\mathbf{I}}} = \hat{\mathbf{e}}_1\hat{\mathbf{e}}_1 + \hat{\mathbf{e}}_2\hat{\mathbf{e}}_2 + \hat{\mathbf{e}}_3\hat{\mathbf{e}}_3 \tag{2.11}$$

and its identity properties are exhibited by noting that

$$\begin{aligned} \overline{\overline{\mathbf{I}}}\bullet\vec{\mathbf{A}} &= \vec{\mathbf{A}}\bullet\overline{\overline{\mathbf{I}}} = \vec{\mathbf{A}} \\ \overline{\overline{\mathbf{I}}}\bullet\overline{\overline{\mathbf{C}}} &= \overline{\overline{\mathbf{C}}}\bullet\overline{\overline{\mathbf{I}}} = \overline{\overline{\mathbf{C}}} \end{aligned}. \tag{2.12}$$

The vector divergence and curl operations can be performed on dyadics in a similar fashion as they are applied to vectors. The dyadic divergence in R^3 is denoted as $\nabla\bullet\overline{\overline{\mathbf{C}}}$ and is defined by

$$\nabla\bullet\overline{\overline{\mathbf{C}}} = \sum_i^3\sum_j^3 \frac{\partial c_{ij}}{\partial e_i}\hat{\mathbf{e}}_j, \tag{2.13}$$

which is a vector function. The curl of a dyadic operator is denoted by $\nabla\times\overline{\overline{\mathbf{C}}}$ and is defined by

$$\nabla\times\overline{\overline{\mathbf{C}}} = \sum_i^3\sum_j^3 \left(\nabla\times c_{ij}\hat{\mathbf{e}}_i\right)\hat{\mathbf{e}}_j, \tag{2.14}$$

which is a dyadic operator.

2.3 Maxwell's Equations

Electromagnetic phenomena are described mathematically using Maxwell's equations of classical electromagnetic theory. Maxwell's equations are neatly summarized in the three independent partial differential equations:

$$\nabla\times\vec{\mathbf{E}}(\vec{\mathbf{r}},t) = -\frac{\partial\vec{\mathbf{B}}(\vec{\mathbf{r}},t)}{\partial t} \tag{2.15}$$

$$\nabla\times\vec{\mathbf{H}}(\vec{\mathbf{r}},t) = \vec{\mathbf{J}}(\vec{\mathbf{r}},t) + \frac{\partial\vec{\mathbf{D}}(\vec{\mathbf{r}},t)}{\partial t} \tag{2.16}$$

$$\nabla \cdot \vec{\mathbf{J}}(\vec{\mathbf{r}},t) = -\frac{\partial \rho(\vec{\mathbf{r}},t)}{\partial t} \tag{2.17}$$

and two dependent differential equations that are derivable from (2.15) through (2.17)

$$\nabla \cdot \vec{\mathbf{B}}(\vec{\mathbf{r}},t) = 0 \tag{2.18}$$

$$\nabla \cdot \vec{\mathbf{D}}(\vec{\mathbf{r}},t) = \rho \tag{2.19}$$

where:

$\vec{\mathbf{E}} \equiv$ electric field intensity [V/m]

$\vec{\mathbf{B}} \equiv$ magnetic flux density [Wb/m^2]

$\vec{\mathbf{J}} \equiv$ electric current density [A/m^2]

$\vec{\mathbf{H}} \equiv$ magnetic field intensity [A/m]

$\vec{\mathbf{D}} \equiv$ electric flux density [C/m^2]

$\rho \equiv$ charge density [C/m^3]

The field densities are related to the flux densities via the constitutive relations:

$$\vec{\mathbf{D}} = \varepsilon \vec{\mathbf{E}} \tag{2.20}$$

$$\vec{\mathbf{B}} = \mu \vec{\mathbf{H}} \tag{2.21}$$

$$\vec{\mathbf{J}} = \sigma \vec{\mathbf{E}} \tag{2.22}$$

where:

$\varepsilon \equiv$ electric permittivity [F/m]

$\mu \equiv$ magnetic permeability [H/m]

$\sigma \equiv$ conductivity [S/m]

The constitutive parameters (μ, ε, σ) and their relations account for the macroscopic effects of matter on the electromagnetic fields and model microscopic considerations such as molecular and atomic structure, lattice geometry and charge distributions. In this thesis, it is assumed that all materials can be modelled with a polarization vector $\vec{\mathbf{P}}$ and magnetization vector $\vec{\mathbf{M}}$ that are linear, isotropic and homogeneous. These parameters are then defined through the following relationships

$$\vec{\mathbf{D}} = \varepsilon_0 \vec{\mathbf{E}} + \vec{\mathbf{P}} = \varepsilon \vec{\mathbf{E}} \tag{2.23}$$

$$\vec{\mathbf{B}} = \mu_0 \left(\vec{\mathbf{H}} + \vec{\mathbf{M}} \right) = \mu \vec{\mathbf{H}} \tag{2.24}$$

where:

$$\varepsilon = \varepsilon_0 \left(1 + \chi_e \right)$$

$$\mu = \mu_0 \left(1 + \chi_m \right)$$

$$\varepsilon_0 = 10^{-9} / 36\pi \, [\text{F/m}]$$

$$\mu_0 = 4\pi 10^{-7} \, [\text{Henry/m}]$$

Assuming time harmonic fields, Maxwell's equations simplify with the use of the time-harmonic factor $e^{j\omega t}$ which produces a factor $j\omega$ under time differentiation. With the help of the constitutive parameters, and assuming a homogeneous medium, equations (2.15) through (2.19) can thus be rewritten as:

$$\nabla \times \vec{\mathbf{E}}(\vec{\mathbf{r}}, \omega) = -j\omega\mu \vec{\mathbf{H}}(\vec{\mathbf{r}}, \omega) \tag{2.25}$$

$$\nabla \times \vec{\mathbf{H}}(\vec{\mathbf{r}}, \omega) = \vec{\mathbf{J}}(\vec{\mathbf{r}}, \omega) + (\sigma + j\omega\varepsilon) \vec{\mathbf{E}}(\vec{\mathbf{r}}, \omega) \tag{2.26}$$

$$\nabla \bullet \vec{\mathbf{J}}(\vec{\mathbf{r}},\omega) = -j\omega\rho \tag{2.27}$$

$$\nabla \bullet \vec{\mathbf{H}}(\vec{\mathbf{r}},\omega) = 0 \tag{2.28}$$

$$\nabla \bullet \vec{\mathbf{E}}(\vec{\mathbf{r}},\omega) = \frac{\rho}{\varepsilon} \tag{2.29}$$

In the remainder of this thesis only time-harmonic fields will be considered and the $e^{j\omega t}$ factor will be suppressed.

The wave equation for the electric fields are developed by applying the curl operation to both sides of (2.25) to get

$$\nabla \times \nabla \times \vec{\mathbf{E}}(\vec{\mathbf{r}},\omega) = -j\omega\mu\left(\nabla \times \vec{\mathbf{H}}(\vec{\mathbf{r}},\omega)\right). \tag{2.30}$$

Substitution of (2.26) into (2.30) yields the *complex vector wave equation* for the time harmonic electric field intensity:

$$\nabla \times \nabla \times \vec{\mathbf{E}} + \gamma^2 \vec{\mathbf{E}} = -j\omega\mu\vec{\mathbf{J}}, \tag{2.31}$$

where

$$\gamma^2 = j\omega\mu(\sigma + j\omega\varepsilon) \tag{2.32}$$

is the propagation constant of the medium.

Solutions to (2.31) are generally in the form of electromagnetic waves (either evanescent or travelling), the form of which is subject to the constitutive parameters of the medium as contained in (2.32). If the medium is lossy ($\sigma \neq 0$), the fields will decay according to the real portion of γ. The distance a wave must travel in a lossy medium to reduce the magnitude of $\vec{\mathbf{E}}$ by a factor of e^{-1} is called the skin depth of the medium. This distance is

$$\delta_{skin} = \frac{1}{\mathrm{Re}\{\gamma\}} = \frac{1}{\omega\sqrt{\mu\varepsilon}\left(\frac{1}{2}\left[\sqrt{1+\left(\sigma/\omega\varepsilon\right)^2}-1\right]\right)^{1/2}} \tag{2.33}$$

2.4 Near and Far-fields

Scattered or radiated electric fields for any given time-harmonic electromagnetic problem can be calculated with Maxwell's equations subject to boundary conditions. In general, the electromagnetic phenomena associated with a given problem such as radiation or scattering appear in two distinctive forms: the near (reactive) fields and the far (radiated) fields. Solutions to (2.31) will in general take the form of spherical wave functions such that each field component possesses amplitude variations of the form $1/r^n$ (n=1,2,3...). The radiated far-fields decay as $1/r$ while the near-fields vary with higher orders of n. Because the near-fields follow an inverse square (or higher order) law, they exist only in significant measure within the immediate vicinity of the radiator or scatterer, where in fact they may dominate. In the near-field zone, electromagnetic fields do not radiate because most of the power is reactive, however due to the time harmonic factor $e^{j\omega t}$ they do oscillate. The far-fields radiate outwardly whereas the complex Poynting vector associated with the near-fields is dominated by their imaginary component. In the near-field, the ratio between the magnetic and electric field intensities is not dictated exclusively by the far-field intrinsic impedance of the medium, $\eta = \sqrt{\mu/\varepsilon}$, and the ratio may be related in a complicated way. Because the near-fields and far-fields of an electromagnetic problem are fundamentally different, it is reasonable to expect that the radar response in the near-field will be different than in the far-field. The near-field (Fresnel zone) and far-field (Fraunhofer zone) are traditionally demarcated by the radius about the antenna/scatterer defined by

$$R_{ff} = {2D^2}/{\lambda}. \tag{2.34}$$

where D is the maximum spatial span of the antenna or scatterer and λ is the wavelength.

A field measurement at a point $|\vec{\mathbf{r}}|$ from an antenna/scatterer such that $|\vec{\mathbf{r}}| \le R_{ff}$ may be effected by near-field components as depicted in Figure 2.1. At typical GPR frequencies, this is often the case.

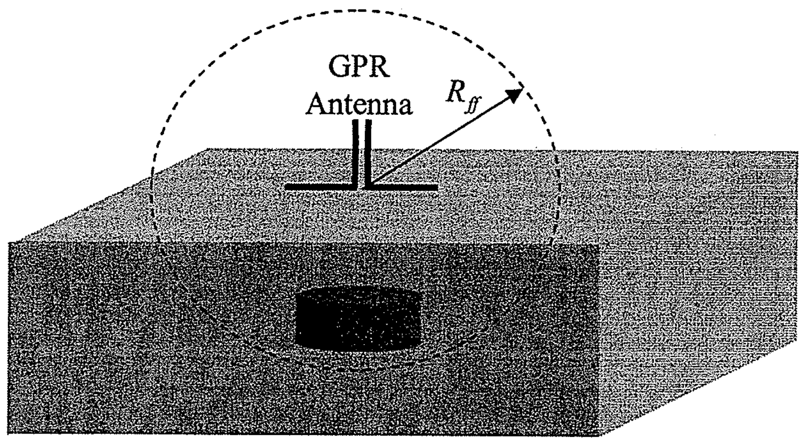

Figure 2.1 GPR target inside the Fresnel zone that is demarcated by a radius about the antenna of R_{ff}

Additionally, if a radar system operates over a wide bandwidth, such as an ultra-wideband (UWB) radar system, the scattering object may drift in and out of the near-field zone of the antennas. For these reasons, far-field approximations that usually greatly simplify electromagnetic formulations cannot be relied upon in the formulation of a ground coupled GPR scattering problem. It is common in the literature to find electromagnetic discussions on GPR scattering that focus on the near-fields in lieu of the radiated far-fields [15],[16].

2.5 Dyadic Green's Function

The solution to equation (2.31) can be formulated as an integral equation with a dyadic Green's function as a kernel [17][18][19]. For a given scattering problem, information regarding the nine scalar components of the dyadic Green's function can be determined by calculation or by direct measurement [34]. In general, both methods of derivation are complicated and at times impractical. In this thesis, the actual derivation of dyadic Green's functions for the landmine problem is not the principal goal, however some in-depth knowledge of the behaviour of the dyadic Green's function will prove necessary in the derivation of a group theoretical scattering model. We seek not the exact form of the dyadic Green's function per-sé, rather we wish to develop knowledge of the behaviour of the dyadic Green's functions and their relation to scattering in GPR applications.

A Green's function is an integral equation kernel that can be used to solve an inhomogeneous differential equation with boundary conditions. It serves roughly an analogous role in partial differential equations as does the Dirac impulse function in the solution of ordinary differential equations [20]. The dyadic Green's function for electromagnetics is the solution of (2.31) and it represents the complete scattering response of a target as a function of time/frequency, spatial location, and polarization. The dyadic Green's function of a buried target such as a landmine is dependant on the target size, shape, and materials of the scatterer as well as being dependent on the target depth and electromagnetic properties of the soil medium. What the dyadic Green's function does not take into account is the excitation by which the radar problem is realized. This is to say that the dyadic Green's function is independent of target excitation and therefore is valid for all radar topologies: monostatic, bistatic and all polarizations.

The geometry of the landmine problem is shown in Figure 2.2. The current source point and receiver observation point which correspond to the transmitting and receiving antennae are located in the free-space upper half-plane region R_1 with free-space constitutive parameters $\varepsilon_1 = \varepsilon_0$ and $\sigma_1 = 0$. All permeabilities are assumed to be μ_0. The landmine scatterer is buried in the lower half-space medium in region R_2 characterized by ε_2 and σ_2. The landmine itself is a target in the region denoted R_Ω and characterized by ε_Ω and σ_Ω such that a contrast exists between R_2 and R_Ω at the interface Γ_Ω between R_Ω and R_2. This is to say

$$\sigma_2 + j\omega\varepsilon_2 \neq \sigma_\Omega + j\omega\varepsilon_\Omega . \tag{2.35}$$

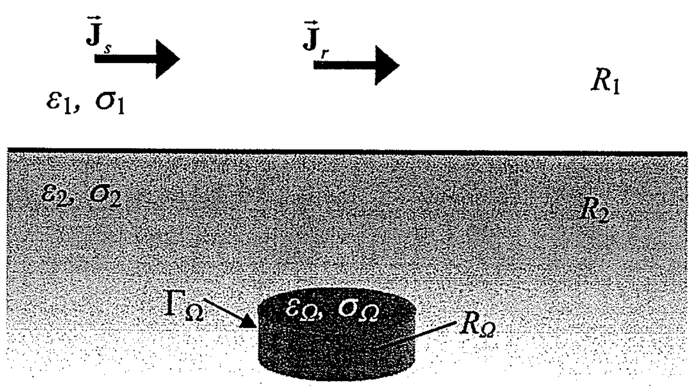

Figure 2.2 Geometry of the subsurface landmine scattering problem. $\vec{\mathbf{J}}_s$ is the source and $\vec{\mathbf{J}}_r$ is the receiver.

For this problem, (2.31) can be restated to formally to describe the electric fields in R_1 by

$$\nabla \times \nabla \times \vec{\mathbf{E}}^{(1)} - \kappa_0^2 \vec{\mathbf{E}}^{(1)} = -j\omega\mu \vec{\mathbf{J}}_s \tag{2.36}$$

where

$$\kappa_0^2 = \omega^2 \varepsilon_0 \mu_0 \tag{2.37}$$

is the free space propagation constant.

The solution of (2.31) in R_1 is [17][18][19]

$$\vec{\mathbf{E}}^{(1)}(\vec{\mathbf{r}}, \omega) = -j\omega\mu_0 \iiint_{V'} \overline{\overline{\mathbf{G}}}_e^{11}(\vec{\mathbf{r}}, \vec{\mathbf{r}}'; \omega) \cdot \vec{\mathbf{J}}_s(\vec{\mathbf{r}}', \omega)\, dv'. \tag{2.38}$$

where $\vec{\mathbf{r}}$ is the observation point and $\vec{\mathbf{r}}'$ is the source point and the integration is over a region V' in R_1 containing the source.

This equation defines the total electric field $\vec{\mathbf{E}}^{(1)}$ at a receiver located at $\vec{\mathbf{r}}$ and is valid anywhere in R_1. $\vec{\mathbf{J}}_s$ represents the source current in the transmitting antenna and $\overline{\overline{\mathbf{G}}}_e^{11}$ is the electric dyadic Green's function for the problem where the source and observation point are located in R_1. The dyadic Green's function satisfies the condition

$$\nabla \times \nabla \times \overline{\overline{\mathbf{G}}}_e^{11}(\vec{\mathbf{r}}, \vec{\mathbf{r}}') - \kappa_0^2 \overline{\overline{\mathbf{G}}}_e^{11}(\vec{\mathbf{r}}, \vec{\mathbf{r}}') = -\overline{\overline{\mathbf{I}}}\delta(\vec{\mathbf{r}} - \vec{\mathbf{r}}') \tag{2.39}$$

where $\delta(\vec{\mathbf{r}} - \vec{\mathbf{r}}')$ is the Dirac delta function and is equal to infinity when $\vec{\mathbf{r}} = \vec{\mathbf{r}}'$ and is zero elsewhere, such that the sifting property is upheld:

$$\iiint_{V'} f(\vec{\mathbf{r}})\delta(\vec{\mathbf{r}} - \vec{\mathbf{r}}')dv' = f(\vec{\mathbf{r}}') \tag{2.40}$$

The total field given by (2.36) may be separated into incident and scattered fields according to

$$\vec{\mathbf{E}}^{(1)} = \vec{\mathbf{E}}^{(s)} + \vec{\mathbf{E}}^{(i)}. \tag{2.41}$$

Consequently, the dyadic Green's function $\overline{\overline{\mathbf{G}}}_e^{11}$ may also be separated into components that contribute to the incident and scattered fields [19][21]. Inserting (2.41) into (2.31) gives

$$\nabla\times\nabla\times\left(\vec{\mathbf{E}}^{(i)} + \vec{\mathbf{E}}^{(s)}\right) - \kappa_0^2\left(\vec{\mathbf{E}}^{(i)} + \vec{\mathbf{E}}^{(s)}\right) = -j\omega\mu\vec{\mathbf{J}}_s. \tag{2.42}$$

This equation can then be separated into two corresponding vector Helmholtz equations

$$\left\{\nabla\times\nabla\times\vec{\mathbf{E}}^{(i)} - \kappa_0^2\vec{\mathbf{E}}^{(i)}\right\} + \left\{\nabla\times\nabla\times\vec{\mathbf{E}}^{(s)} - \kappa_0^2\vec{\mathbf{E}}^{(s)}\right\} = -j\omega\mu\vec{\mathbf{J}}_s. \tag{2.43}$$

The first component in (2.43) represents the radiation from the source antenna, the second component represents the scattered radiation. The incident radiation from the source antenna in free space is defined as the radiation with no scatterers or ground present [19]

$$\nabla\times\nabla\times\vec{\mathbf{E}}^{(i)} - \kappa_0^2\vec{\mathbf{E}}^{(i)} = -j\omega\mu\vec{\mathbf{J}}_s. \tag{2.44}$$

The solution to this equation is in the form of (2.38) and is given by

$$\vec{\mathbf{E}}^{(i)}(\vec{\mathbf{r}},\omega) = -j\omega\mu_0 \iiint_{V'} \overline{\overline{\mathbf{G}}}_0(\vec{\mathbf{r}},\vec{\mathbf{r}}';\omega)\cdot\vec{\mathbf{J}}_s(\vec{\mathbf{r}}',\omega)\,dv' \tag{2.45}$$

where $\overline{\overline{\mathbf{G}}}_0$ represents the *free space Green's function* given by the established equation

$$\overline{\overline{\mathbf{G}}}_0(\vec{\mathbf{r}},\vec{\mathbf{r}}') = \left(\overline{\overline{\mathbf{I}}} + \frac{1}{\kappa_0^2}\nabla\nabla\right)\frac{e^{-j\gamma|\vec{\mathbf{r}}-\vec{\mathbf{r}}'|}}{4\pi|\vec{\mathbf{r}}-\vec{\mathbf{r}}'|}. \tag{2.46}$$

For convenience, the notation can be simplified by dropping the frequency variable ω.

The term $\nabla\nabla$ is a dyadic operator with elements $\partial\partial/\partial x_i\,\partial x_j$. Because of this operator, the non-asymptotic free space Green's function $\overline{\overline{\mathbf{G}}}_0$ is not a diagonal dyadic.

$\vec{\mathbf{E}}^{(i)}$ is simply the radiation from the source antenna $\vec{\mathbf{J}}_s$ as it would normally radiate in free space. The dyadic Green's function for the scattered field is derived by substitution of equations (2.38) and (2.45) into (2.41) by means of the principle of *scattering superposition* [21] so that

$$\vec{\mathbf{E}}^{(s)}(\vec{\mathbf{r}}) = -j\omega\mu\iiint\limits_{V'}\overline{\overline{\mathbf{G}}}_s(\vec{\mathbf{r}},\vec{\mathbf{r}}')\cdot\vec{\mathbf{J}}_s(\vec{\mathbf{r}}')\,dv' \tag{2.47}$$

where the scattering dyadic Green's function is

$$\overline{\overline{\mathbf{G}}}_s(\vec{\mathbf{r}},\vec{\mathbf{r}}') = \overline{\overline{\mathbf{G}}}(\vec{\mathbf{r}},\vec{\mathbf{r}}') - \overline{\overline{\mathbf{G}}}_0(\vec{\mathbf{r}},\vec{\mathbf{r}}'). \tag{2.48}$$

For problems involving electromagnetic phenomena interacting in two or more media, such as the problem of a buried landmine in a half-space, the type of dyadic Green's function involved in the integral equations (2.38) and (2.45) are the dyadic Green's functions of the third kind [21]. These integral equations are only valid in the prescribed region R_1 when the source $\vec{\mathbf{J}}_s$ is also located in R_1.

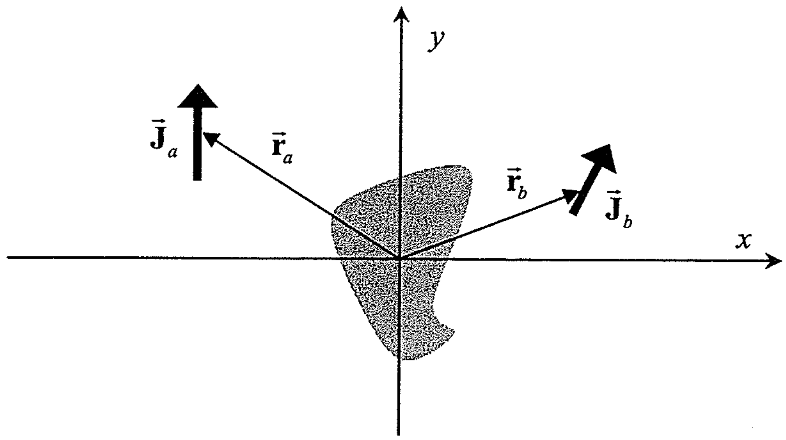

Figure 2.3 Geometry of bistatic measurement system for GPR. The ground surface lies on the z = 0 plane and the target is located z < 0 while both antenna elements $\vec{\mathbf{J}}_a$ and $\vec{\mathbf{J}}_b$ are located above ground z > 0.

Figure 2.3 shows the geometrical description of a general bistatic radar system. The system has two current elements $\vec{\mathbf{J}}_a$ located at $\vec{\mathbf{r}}_a$ and $\vec{\mathbf{J}}_b$ located at $\vec{\mathbf{r}}_b$ so that two bistatic observations are possible. One observation has $\vec{\mathbf{J}}_a$ as the source antenna and $\vec{\mathbf{J}}_b$ as the receiving antenna and the second observation has the reciprocal case where $\vec{\mathbf{J}}_b$ is the source and $\vec{\mathbf{J}}_a$ is the receiver.

The reciprocity theorem for a bistatic system such as the system shown in Figure 2.3 can be expressed via the reaction theorem of Rayleigh-Carson which for this case is written as

$$\iiint_V \vec{\mathbf{J}}_a(\vec{\mathbf{r}})\cdot\vec{\mathbf{E}}_b(\vec{\mathbf{r}})dv = \iiint_V \vec{\mathbf{J}}_b(\vec{\mathbf{r}})\cdot\vec{\mathbf{E}}_a(\vec{\mathbf{r}})dv, \tag{2.49}$$

where $\vec{\mathbf{E}}_a$ and $\vec{\mathbf{E}}_b$ represent the fields radiated by $\vec{\mathbf{J}}_a$ and $\vec{\mathbf{J}}_b$ respectively. Equation (2.47) and (2.49) can be combined to yield

$$\iiint_V \vec{\mathbf{J}}_a \bullet \left(\iiint_V \overline{\overline{\mathbf{G}}}_s \bullet \vec{\mathbf{J}}_b dv' \right) dv = \iiint_V \vec{\mathbf{J}}_b \bullet \left(\iiint_V \overline{\overline{\mathbf{G}}}_s \bullet \vec{\mathbf{J}}_a dv' \right) dv . \quad (2.50)$$

If the current sources are assumed to be Hertzian dipoles (i.e. infinitesimal sources) (2.50) reduces to

$$\vec{\mathbf{J}}_a(\vec{\mathbf{r}}_a) \bullet \overline{\overline{\mathbf{G}}}_s(\vec{\mathbf{r}}_a, \vec{\mathbf{r}}_b) \bullet \vec{\mathbf{J}}_b(\vec{\mathbf{r}}_b) = \vec{\mathbf{J}}_b(\vec{\mathbf{r}}_b) \bullet \overline{\overline{\mathbf{G}}}_s(\vec{\mathbf{r}}_b, \vec{\mathbf{r}}_a) \bullet \vec{\mathbf{J}}_a(\vec{\mathbf{r}}_a) . \quad (2.51)$$

These relationships express the fact that if one interchanges the role of transmit and receive antennas in the experiment, one will expect to arrive at the same result. Equation (2.50) is valid for any arbitrary current densities and scatterers. This relationship suggests that the dyadic Green's function must be symmetric:

$$\overline{\overline{\mathbf{G}}}_s(\vec{\mathbf{r}}, \vec{\mathbf{r}}') = \left[\overline{\overline{\mathbf{G}}}_s(\vec{\mathbf{r}}', \vec{\mathbf{r}}) \right]^T . \quad (2.52)$$

One convenient advantage of (2.52) is that when constructing the dyadic Green's function for a given bistatic problem, one need not calculate all of the elements of the dyadic since the dyadic symmetry requires that only the diagonal and upper (or lower) triangular elements be calculated.

Equation (2.47) illustrates that a scattered response from a subsurface target reveals information regarding the target's geometry and constitutive parameters contained in the Green's function. Unfortunately, due to the absence of the uniqueness properties in the inverse scattering problem, an absolute determination of the target's boundary conditions is elusive. It is possible to rewrite (2.47) in operator notation as [22]

$$\vec{\mathbf{E}}^{(s)}(\vec{\mathbf{r}}) = \overline{\overline{\mathbf{\Lambda}}}(\vec{\mathbf{r}}, \vec{\mathbf{r}}') \bullet \vec{\mathbf{J}}_s(\vec{\mathbf{r}}') \quad (2.53)$$

where $\overline{\overline{\Lambda}}$ is a dyadic integral operator such that (2.47) is satisfied. In a radar experiment it is assumed that $\vec{\mathbf{J}}_s$ is known a priori and that $\vec{\mathbf{E}}^{(s)}$ is determined experimentally. The inverse problem is essentially the problem of determining $\overline{\overline{\Lambda}}$. Unfortunately due to the very nature of GPR measurements, any attempt to acquire complete and flawless information regarding $\vec{\mathbf{E}}^{(s)}$ is bound to fail since measurements can not be taken at all perspectives and frequencies, and target measurements will be perturbed by weak soil inhomogeneities. Incomplete knowledge of $\vec{\mathbf{E}}^{(s)}$ and $\vec{\mathbf{J}}_s$ with no a priori information regarding the target leads to an *ill-posed* problem in the reconstruction of the target [3]. This is not to say that no useful information can be extracted about the form of the dyadic Green's function from a GPR experiment, however the ill-posedness of the problem necessarily impedes the direct determination of the target boundary conditions. Perhaps more importantly without proper radar signal processing, a collection of GPR measurements of the form (2.47) will not yield any tangible information regarding the location of the target.

2.6 Range Processing of GPR Data

2.6.1 GPR Data Collection

In practical electromagnetic experiments, one does not usually deal directly with field quantities, but rather with the voltages induced at the antenna terminals as measured by a vector network analyzer (VNA). As shown in Figure 2.4 the role of the VNA in radar experiments is to determine scattered fields indirectly by measuring the induced voltage on the receiving antenna with respect to the voltage supplied by the VNA to the transmitting antenna, which is assumed to remain constant. Neglecting the coupling between the transmitting and receiving antennas, the voltage induced at the terminals of the receiving antenna due to the scattered field defined in (2.47) can be described as [34]

$$v_{Rx}(f) = \iiint_V \vec{\mathbf{w}}(\vec{\mathbf{r}}, f) \cdot \vec{\mathbf{E}}^{(s)}(\vec{\mathbf{r}}, f)\, dv. \tag{2.54}$$

where $\vec{\mathbf{w}}$ describes the receiving antenna's spatial and frequency domain behavior. In principle, $v_{Rx}(f)$ is dependent entirely on radar system and target parameters.

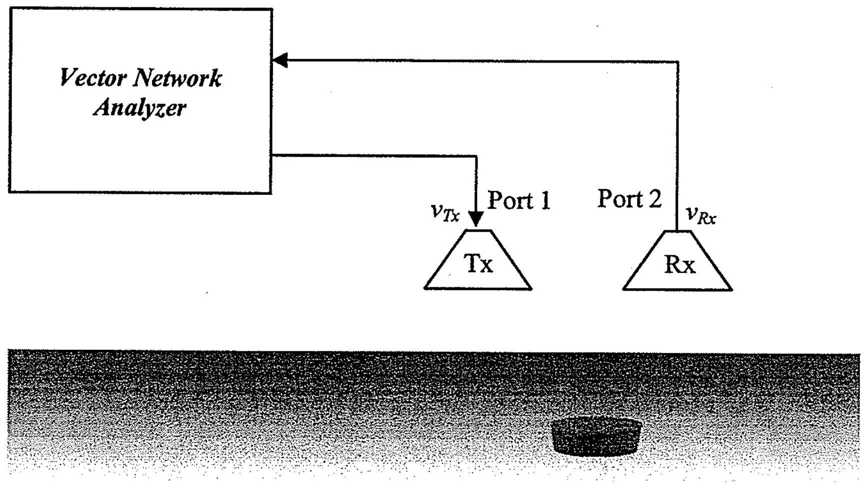

Figure 2.4 GPR measurements using a vector network analyzer

Assuming the usual two port model as shown in Figure 2.4 and that the VNA has been properly calibrated to take the electrical length of the cables into consideration (i.e. the s-plane has been moved to the end of the cables), we may consider the transmitted voltage v_{Tx} as the outgoing voltage wave from port 1 while the received voltage v_{Rx} induced from the scattered radiation defined in (2.54) may be considered as the ingoing wave into port 2. In this context, the radar signal recorded by the VNA is the S_{12} parameter as defined by:

$$S_{12}(f) = \frac{v_{Rx}(f)}{v_{Tx}(f)} = I(f) + jQ(f), \tag{2.55}$$

where I and Q represent the real and imaginary components of S_{12}. In the case of monostatic radar, v_{Rx} and v_{Tx} are measured from the same port and it is the S_{11} parameter that is recorded.

2.6.2 Range Processing for Stepped Frequency Radar

The primary objectives of a GPR system in landmine detection is to answer the two key questions regarding a subsurface scatterer: what is the target made of and where is the target located? The electromagnetic theory presented in section 2.5 dealt with how information regarding a target's boundary conditions can make itself available in the scattered field. Although accurate imaging for identification purposes is difficult, because of the problems previously mentioned, techniques for predicting the target's location can be developed. This section is devoted to the methods of determining via imaging the location of a target. The I and Q data collected by the vector network analyzer is in the frequency domain and in itself has little predictive value to the casual observer. In order to resolve the location of a target in the downward (range) direction for a given stepped frequency radar system, a matched filter is implemented in the form of an inverse Fourier transform IFFT algorithm.

The stepped-frequency radar first emits one continuous sinusoidal signal at a given initial frequency f_i and measures the steady-state response as shown in (2.55). The radar system then steps up the frequency by Δf to a new frequency of $f_2 = f_i + \Delta f$ and then repeats the process. For a stepped frequency system with N frequency steps that operates over a given bandwidth BW up to a given maximum frequency f_{max}, the frequency location in the range are defined by

$$f_n = f_i + (n-1)\Delta f, \quad n = 1,2\ldots,N \tag{2.56}$$

where

$$f_{\max} = f_N = f_i + (N-1)\Delta f \tag{2.57}$$

The data collected by one *burst* of frequencies (all frequencies defined in (2.56) for $n = 1,2\ldots,N$) is denoted

$$U_n = S_{12}(f_n) = I(f_n) + jQ(f_n), \quad n = 1,2\ldots,N. \tag{2.58}$$

U_n can be transformed into the time domain by an inverse Fourier transform via the IFFT algorithm such that

$$u(m) = \frac{1}{N}\sum_{n=1}^{N} U_n e^{-2\pi(m-1)(n-1)/N}, \quad m = 1,2,\ldots,N. \tag{2.59}$$

The resulting IFFT processed data can be smoothed by interpolation if U_n is zero padded before the IFFT is applied. Although no new useful information is gained by zero padding, the results may be more appealing to the eye.

The signal can be scaled into the appropriate temporal time range by setting

$$s(t_m) = u\left(\frac{t_m}{\Delta t} + 1\right) = u(m) \tag{2.60}$$

where $\Delta t = \frac{1}{2BW}$ and $t_m = \Delta t(m-1)$. The resulting time domain signal can be transformed into the range domain, where radar information is ultimately of service, by means of the simple linear relationship

$$d_m = \frac{c}{\sqrt{\varepsilon_r}} t_m. \tag{2.61}$$

where $c/\sqrt{\varepsilon_r}$ represents the speed of light in the medium and d_m represents the distance that the electromagnetic waves have traveled from the transmitter, to a point in space and back to the receiver. In the monostatic radar case where the transmitter and receiver are co-located, the range R_m from the antenna to a point in space is simply $R_m = d_m/2$. It will be shown later on that this equation may be used as an approximation for range in a bistatic situation when the antenna pair are close together and adequately far from the region under observation.

In the range domain, the separation between successive *range bins* (i.e. the distance between R_m and R_{m+1}) is called the *range resolution* and is denoted by

$$\Delta R = \frac{c/\sqrt{\varepsilon_r}}{2BW}. \tag{2.62}$$

This value represents the minimum distance in the range domain between two point scatterers such that the radar can resolve the targets separately. It measures the radar system's ability to "see clearly" and is considered a figure of merit in the sense that a small ΔR is more desirable than a large ΔR. It is instructive to note that the range resolution is dependent only on the speed of light in the medium and on the system bandwidth. That said, (2.60) may be rewritten in the range domain to give:

$$s(R_m) = u\left(\frac{R_m}{\Delta R}+1\right) = u(m), \quad R_m = \Delta R(m-1) \tag{2.63}$$

The meaning of the above equation can be made clearer by considering an example where an ideal monostatic stepped frequency radar system with a bandwidth BW= 4GHz over N=128 frequency steps operating in free space (ε_r=1) is employed to analyze a point target located 0.5m from the *Tx-Rx* antenna as shown in Figure 2.5.

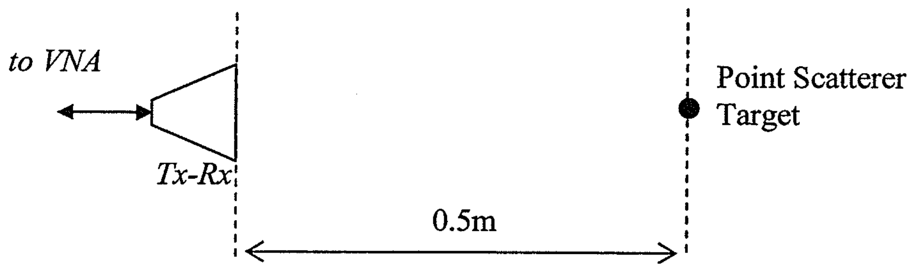

Figure 2.5 Setup for a SFCW radar and target with parameters of N=128 frequency steps, BW=4GHz operating in free space, ε_r=1.

Disregarding physical concerns such as the $1/r$ decay, the frequency dependence of the antenna and target etc., the raw data recorded by the VNA could be expected to resemble the simulated data in Figure 2.6.

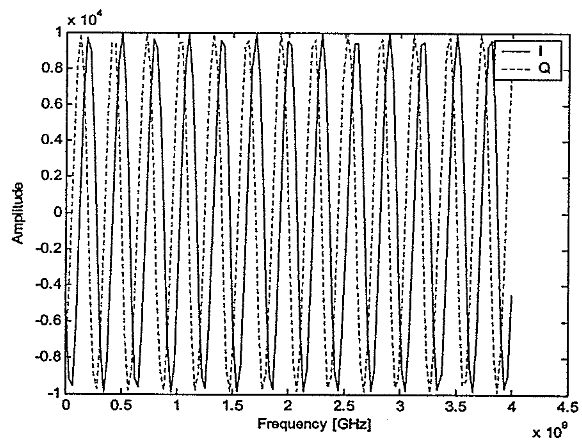

Figure 2.6 Simulated raw I and Q data for the scenario shown in Figure 2.5.

Applying the IFFT as in (2.59) and transforming to the range domain via (2.63) for the monostatic case, the range profile is calculated from the data as shown in Figure 2.7. The result demonstrates that the range profile represents the proverbial radar "blip" on the screen that identified the location of the target. In the vernacular of radar signal processing, Figure 2.7 represents the *A-scan* of the data when the radar system is at a given position.

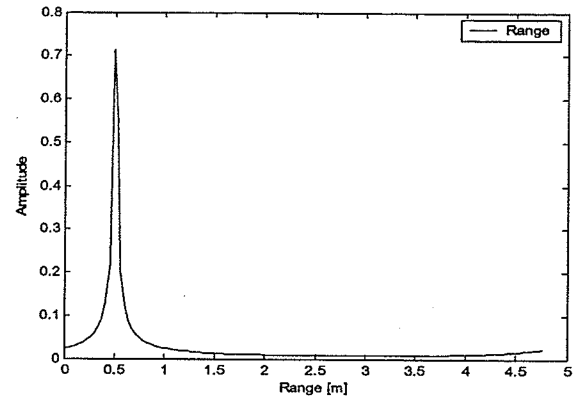

Figure 2.7 A-scan of radar data. The peak indicates the location of the object in the range domain

Consider now the setup shown in Figure 2.8 when a second point scatterer is added at a distance Δd from the first and the radar experiment is repeated:

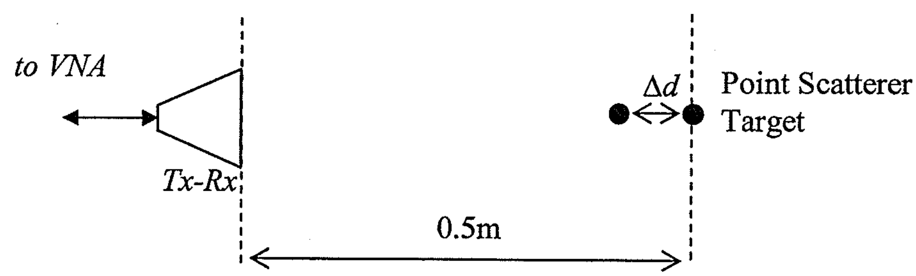

Figure 2.8 Scenario involving two point scatterers spaced Δd from one another

The corresponding A-scan for this experiment is simulated in Figure 2.9 for the cases when $\Delta d < \Delta R$ and $\Delta d > \Delta R$. The results show that when the target spacing is less than the range resolution, the radar system can not differentiate between targets. This corresponds to a blurring effect in many radar applications.

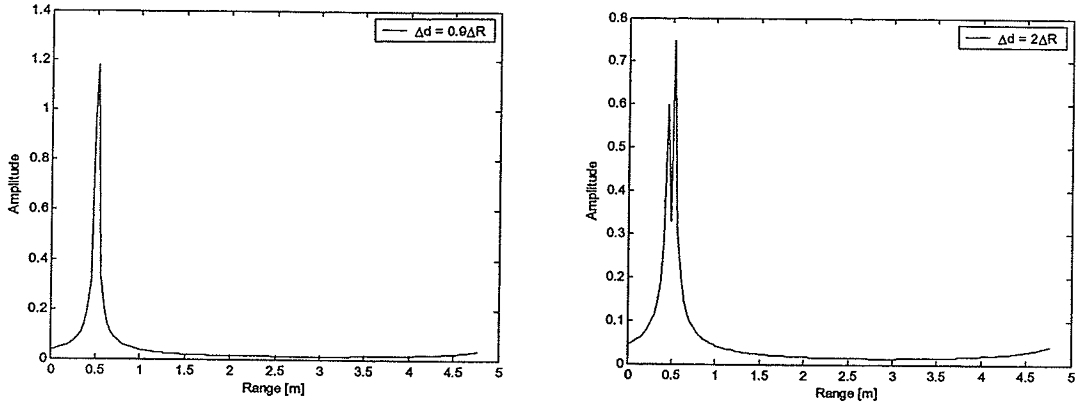

(a) (b)

Figure 2.9 The effects of range resolution on closely spaced point scatterers separated by distance Δd: (a) $\Delta d = 0.9\Delta R$, (b) $\Delta d = 2\Delta R$

2.6.3 Bistatic Range Error

Ultimately, the job of the GPR transceiver is to measure the target response as a function of distance from the transceiver. Under the bistatic conditions however, the distance is not measured along a single path, but rather from the transmitter to the target and back to the receiver. Figure 2.10 shows the essential geometry for a subsurface GPR range imaging measurement. For a given measurement, the transmitter is located at $\vec{\mathbf{r}}_{Tx}$, the receiver is located at $\vec{\mathbf{r}}_{Rx}$ and target is located at $\vec{\mathbf{r}}_{\zeta}$. The distance the signal must travel is given by

$$d = \left|\vec{\mathbf{r}}_{Tx} - \vec{\mathbf{r}}_{\zeta}\right| + \left|\vec{\mathbf{r}}_{Rx} - \vec{\mathbf{r}}_{\zeta}\right| \tag{2.64}$$

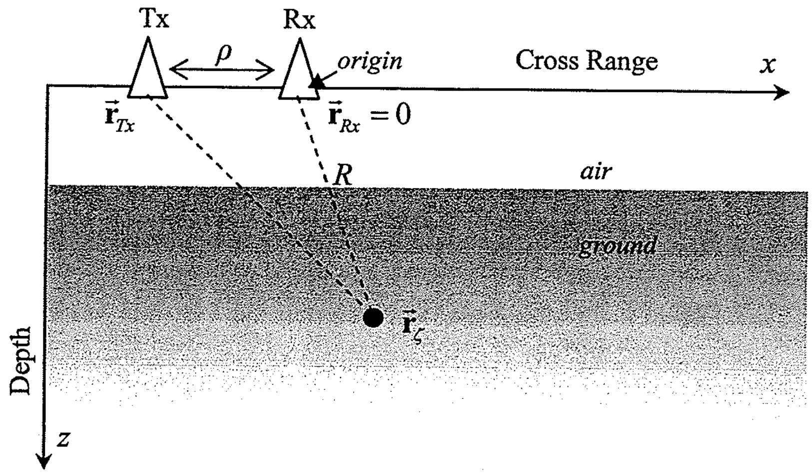

Figure 2.10 Geometry of GPR measurement

The distance d is a scalar quantity and the distance of the target from the receiver antenna R is not linearly related to d because of the antenna separation ρ in the bistatic geometry. If we let the receiver antenna as the coordinate origin so that $\vec{\mathbf{r}}_{Rx} = 0$ then $\left|\vec{\mathbf{r}}_{\zeta}\right| = R$ and $\left|\vec{\mathbf{r}}_{Tx}\right| = \rho$ and (2.64) reduces to

$$d = \left|\vec{\mathbf{r}}_{Tx} - \vec{\mathbf{r}}_{\zeta}\right| + R. \tag{2.65}$$

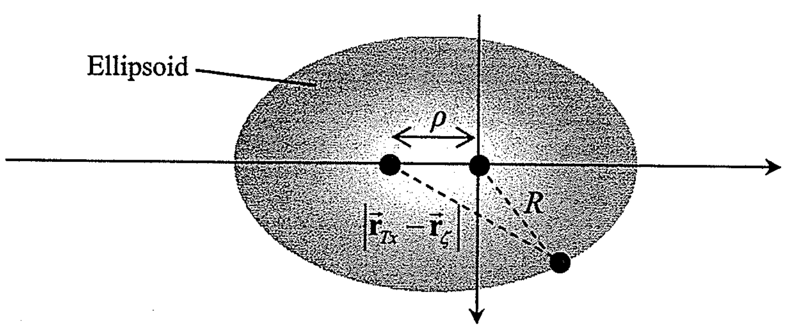

Figure 2.11 Ellipsoidal locus of bistatic range measurement: The ellipsoid is an ellipse revolved around an axis containing $\vec{\mathbf{r}}_{Tx}$ and $\vec{\mathbf{r}}_{Rx}$. All points on the ellipsoid represent equal travel path distance *d*.

This relationship implies that once d is measured, the target may be anywhere on a three dimensional ellipsoid with $\vec{\mathbf{r}}_{Tx}$ and $\vec{\mathbf{r}}_{Rx} = 0$ as the foci as shown in Figure 2.11, where the ellipsoid represents the locus of equal travel distance d [23].

This nonlinear relationship between the detected distance d and R will manifest itself as an error in the detected range of the scatterer. This error is in general a function of the axial ratio of the ellipse in Figure 2.11. For the case of GPR, all targets are assumed to be located in the lower half of the ellipsoid. The range error associated with the bistatic arrangement will become negligible if ρ is made sufficiently small or if R is made sufficiently large so that the ellipse axial ratio converges to that of a circle. Under these conditions $\left|\vec{\mathbf{r}}_{Tx} - \vec{\mathbf{r}}_{\varsigma}\right| \to R$ and the measured distance can be approximated as the monostatic case

$$d \approx 2R. \tag{2.66}$$

This approximation may not always be accurate and, as a result, some range error may affect the outcome of the measurement. This effect can be somewhat countered by incorporating directive antennas so that targets at oblique incidence from either antenna will not be range profiled. Further reductions in error will result if the antennas are both raised slightly above the ground to increase R and therefore improve the approximation.

2.6.4 Range Migration

The range R of a point target as measured by the GPR on a synthetic aperture on the x-axis is

$$R = \left|\vec{\mathbf{r}}_{Rx} - \vec{\mathbf{r}}_{\varsigma}\right| \tag{2.67}$$

where the coordinate origin is no longer necessarily fixed at the receiver. For a synthetic aperture along the x-axis, $\vec{\mathbf{r}}_{Rx} = x\hat{\mathbf{r}}_x$ and (2.67) can be rewritten as

$$R = \sqrt{\left(x - x_\varsigma\right)^2 + y_\varsigma^2 + z_\varsigma^2} \tag{2.68}$$

where $\langle x_\varsigma, y_\varsigma, z_\varsigma \rangle$ are the Cartesian coordinates for the target. This is the equation of a hyperbola. The implications of (2.68) are that for a stationary subsurface point target located at $\vec{\mathbf{r}}_\varsigma$ in R^3 the measured distance between the receiver and the target R will vary hyperbolically along the aperture in the range domain and (except for measurements directly above the target) the measured range is not linearly related to target depth z_ς. If the A-scans for successive range measurements of a target along a synthetic aperture are stacked along the cross range, the resulting image of the target will exhibit a hyperbolic contour as shown in Figure 2.12.When successive A-scans are stacked in this manner, the resulting image is called a *B-scan*.

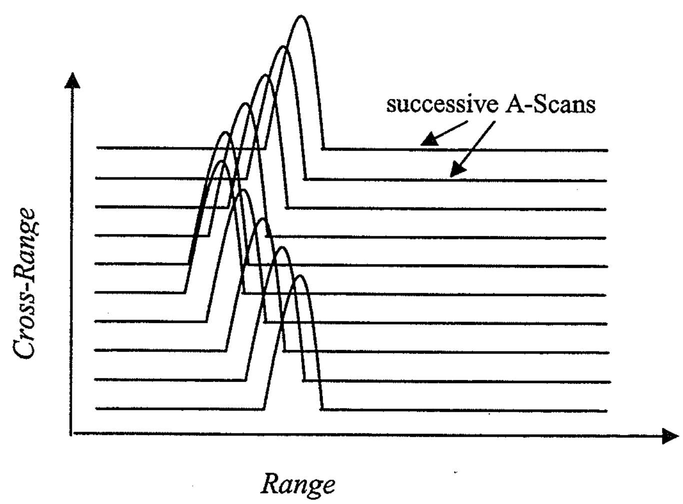

Figure 2.12 Construction of a B-scan from successive A-scans

This hyperbolic relationship between range and cross-range is shown graphically in Figure 2.13.

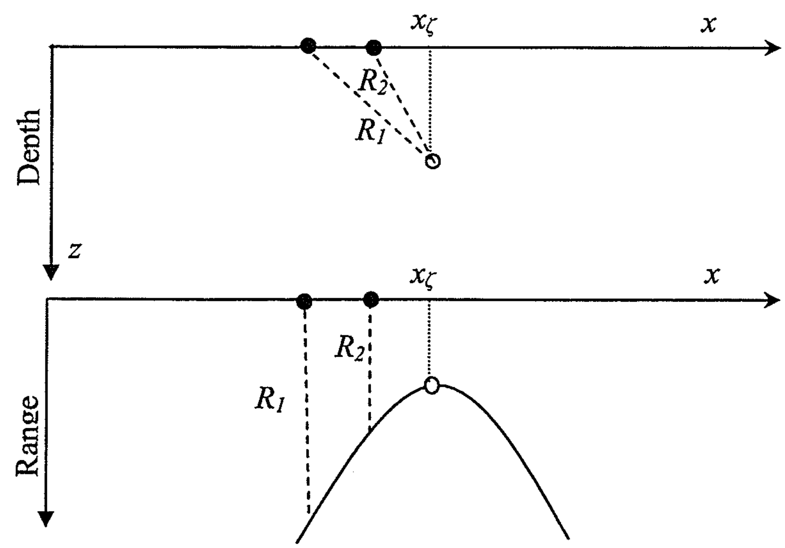

Figure 2.13 Hyperbolic relationship between range and cross-range. R_1 and R_2 represent measured range values at different locations on x.

Another repercussion of the preceding arguments is that it is impossible to derive the location of a target in R^3 space with a single synthetic aperture. For a single linear aperture, only the cross-range component x_ζ may be derived as the hyperbola maximum in the general case. A priori knowledge either of the targets other two components, y_ζ or z_ζ is sufficient to pinpoint the precise location of the target since the problem then becomes a two dimensional one. For example, if it is known that the target is located directly under the aperture at an undetermined depth such that $y_\zeta = Y_\zeta$ and we determine that $x_\zeta = X_\zeta$ from Figure 2.13, then (2.68) involves only one unknown in z_ζ which can be solved by setting $x = X_\zeta$ to get

$$z_\zeta = Z_\zeta = \sqrt{Y_\zeta^2 - R^2}\,. \tag{2.69}$$

Given the two dimensional nature of the B-scan, the stepped frequency IFFT equation (2.59) must be augmented to take the cross range into consideration. For a given B-scan composed of L individual A-scans each with N frequency steps (corresponding to N range bins if no zero padding is used) the equation for the resulting B-scan image becomes:

$$u(m,l) = \frac{1}{N}\sum_{n=1}^{N} U_n(l) e^{-2\pi(m-1)(n-1)/N}, \quad \begin{array}{l} m = 1,2,\ldots,N \\ l = 1,2\ldots,L \end{array} . \tag{2.70}$$

Unfortunately, practical GPR target signatures will not exhibit perfect hyperbolic signatures, even for point targets, because of range resolution, the natural $1/r^n$ decay of electromagnetic radiation in the near and far-fields and antenna directivity. The effects these conditions have on the image are to blur and fade what would otherwise be a perfect hyperbola for a point target. Other effects that may degrade or alter a GPR image are near-field electromagnetics, scattering from finite targets, target frequency dependence and polarization. An example of a B-scan with a single subsurface scatterer is shown in Figure 2.14 where the imperfections in the range reconstruction become evident.

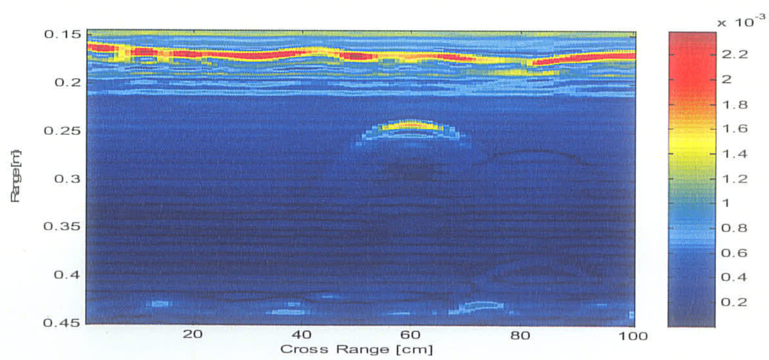

Figure 2.14 Example of a B-scan image.

2.7 Focussing in the Cross Range

Ultimately we would like to have the reconstructed image of a target resemble the actual target as closely as possible. Although a hyperbola can be a valuable representation of a point scatterer, it is not the most desirable representation for imaging purposes. Determining location by finding hyperbolic maximums in lieu of visualizing the target in the cross range as well as in the range domain is not the most physically realistic depiction of a target. The process of "converging" a hyperbolic range signature into a more realistic spatial image is called range migration and is in general a very complicated matter. One very promising algorithm currently of interest in the GPR community is *frequency-wavenumber migration* or F-K migration. F-K migration has been used to provide high quality images in many seismic applications and is gaining a reputation in GPR imaging. In GPR landmine detection, the hyperbolic curves usually seen in the GPR data can be collapsed to a point representing the position of the landmine. Essentially F-K migration is designed to back propagate the wave equation so that the position of a point source, i.e., the landmine, can be identified. The algorithm involves a simple mapping from the frequency domain to the vertical wavenumber by means of an interpolation procedure for the data samples known as the Stolt interpolation. The details of the F-K migration algorithm can be found in the literature [24, 25, 26] and will not be repeated. The effects of the F-K migration algorithm on simulated data in can be seen below in Figure 2.15.

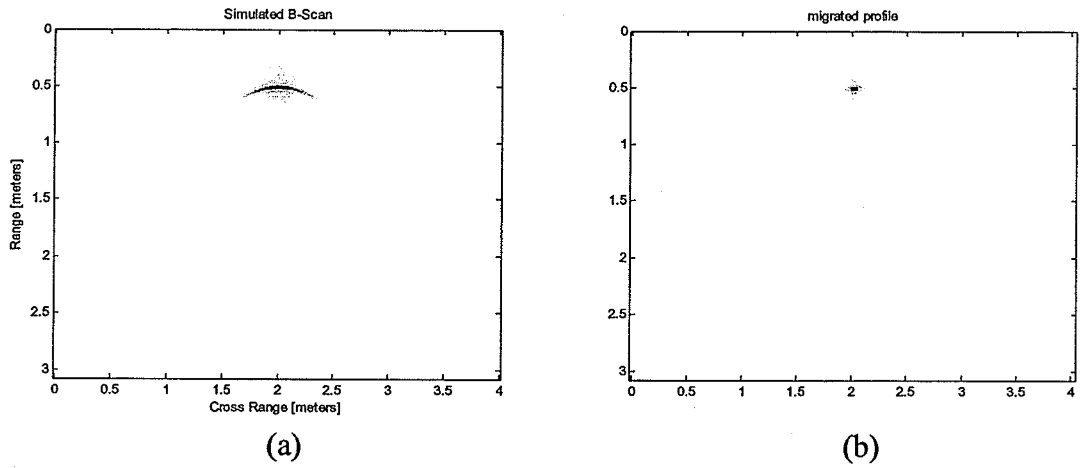

Figure 2.15 (a) Un-migrated B-scan, (b) Results of F-K migration on B-scan

CHAPTER 3
Symmetry and Group Theory

3.1 The Symmetry Concept

Symmetry is a concept that has fascinated civilizations for millennia, as witnessed in ancient art and architecture. For over a thousand years, Islamic art has emphasized only strong geometrical patterns underlining the Islamic notion of the divinity of numbers and affirming the humility required to accept the ultimate infallibility of the divine creation - the work of man will never equal the natural creations of God [27]. During the Renaissance, the use of symmetry became prevalent to emphasize divine order and God as the centre and the use of symmetrical gothic spires to imitate a movement towards heaven [28].

Évariste Galois (1811-1832) is credited with giving a formal language to the concept of symmetry in the early 1800s when he developed a new algebra designed to describe, manipulate and analyse symmetry. Galois' algebra, *Group theory* is a powerful formal method for analyzing abstract and physical systems in which symmetry is present and has surprising importance in physics, especially quantum mechanics where it was used extensively at the beginning of the 20th century to describe the geometrically symmetrical nature of atoms, molecules and lattices [29]. Physicists have even used group theoretical arguments to prove the existence of sub-atomic particles [30]. Recently, Group theory has emerged more frequently in electrical engineering problems and applications in signal processing, network theory and electromagnetic scattering [31][32][33].

In this chapter, the basic concepts of group theory that will be required in later electromagnetic discussions will be covered. These concepts include symmetry planes, definition of groups and group algebra, degeneracy and invariance. These Group theoretic principles will subsequently be applied in electromagnetic scattering theory in Chapter 4 and will be put to practical use in the subsequent chapters which outline the symmetry filter algorithm.

3.2 Groups and Symmetry

Because a formal mathematical language to describe symmetry is sought in Group theory, this chapter will begin with formal definitions of groups and symmetry. In mathematical vernacular, a Group $\mathcal{G}$ is defined as a set of elements $g \in \mathcal{G}$ that obey the following four properties with respect to a defined group multiplication operation $g_i\, g_j$:

i. ***Closure***

For every group element g_i, g_j, the result of the group multiplication operation $g_i g_j = g_k$ where g_i, g_j, $g_k \in \mathcal{G}$. In other words, the operation is an internal one.

ii. ***Associativity***

For all group elements g_i, g_j, $g_k \in \mathcal{G}$, $(g_i\, g_j)\, g_k = g_i(g_j\, g_k)$.

iii. ***Existence of identity element***

For all group elements $g \in \mathcal{G}$ there exists an element $\mathcal{E} \in \mathcal{G}$ such that $\mathcal{E}g = g\mathcal{E} = g$.

iv. ***Existence of an inverse element***

For every group element $g_i \in \mathcal{G}$ there exists a corresponding element $g_i^{-1} \in \mathcal{G}$ such that $g_i\, g_i^{-1} = g_i^{-1}\, g_i = \mathcal{E}$.

It should be noted that in general, commutativity does not hold. However, in the case that it does hold so that for every element g_i and $g_j \in \mathcal{G}$ we have $g_i g_j = g_j g_i$ the group $\mathcal{G}$ is said to be *Abelian.*

Mathematically speaking, symmetry can be defined as the "*invariance to all group multiplication operations of a specified group*"[34]. Operations represented by group elements can encompass a plethora of physical consequences including (but certainly not limited to) color, physical dilation (morphing) and in the quantum world, momentum and spin [29]. In this thesis, the symmetry inherent in the properties governing Maxwell's equations in the form of duality and reciprocity are of key interest and much use will be made of the inherent symmetries associated with these fundamental concepts. However the primary interest will lie in the *point symmetry groups* consisting of geometrical rotations, reflections and combinations thereof as it is with these groups that a radar detection scheme suitable for symmetrical subsurface target recognition will be pieced together. Since the symmetry properties in electromagnetism and in geometry will be exploited, a brief introduction to symmetry with respect to these concepts follows.

3.2.1 Basic Properties and Definitions in Group theory

The *order* of a group $\mathcal{G}$ is defined as the number of elements in $\mathcal{G}$ which may be finite, countably infinite, or non-countably infinite. A *finite group* is a group with a finite number of elements N,

$$\mathcal{G} = \{g_\ell\} \qquad \ell = 1,2\ldots N \tag{3.1}$$

A *Lie group* is a group with a non-countably infinite number of elements that depend on a set of real, continuously varying parameters $\{a_1, a_2 \ldots a_n\}$ where n may or may not be infinite. This implies that an infinitesimal change in one group element yields another element,

$$\mathcal{G} = \{g(a_1, a_2 \ldots a_n)\}. \tag{3.2}$$

Note that the group elements are not functions: varying the parameters denotes another group element. The vast majority of groups that arise in physical situations are finite groups or Lie groups [35].

A group $\mathcal{G}$ is said to be *cyclic* if it can be expressed as a power of a single element g such that

$$\begin{aligned} &\mathcal{G} = \{g_\ell\} \\ &g_\ell = (g)^\ell, \qquad \ell = 1, 2, \ldots, N \end{aligned} \tag{3.3}$$

where the identity element is

$$\mathcal{E} = g_N = (g)^N. \tag{3.4}$$

A group $\mathcal{G}$ is said to be a *direct product* of n of its *subgroups* $\mathcal{H}_1$, $\mathcal{H}_2$, …, $\mathcal{H}_n$ (each of which is a group that obeys the group axioms of section 3.2 in its own right) if the elements of the different subgroups commute and every element of $\mathcal{G}$ can be uniquely expressed as

$$g = h_1 \cdot h_2 \cdot \cdots \cdot h_n \tag{3.5}$$

where h_i is an element from the $\mathcal{H}_i$ subgroup. If the n subgroups have only the identity element $\mathcal{E}$ in common then the resulting group $\mathcal{G}$ is denoted

$$\mathcal{G} = \mathcal{H}_1 \otimes \mathcal{H}_2 \otimes \cdots \otimes \mathcal{H}_n. \tag{3.6}$$

If the constituent subgroups have no elements in common (save the identity element), the order of a direct product group is the product of the subgroup orders. If the constituent subgroups happen to share an element, then the order of the direct product group is the product of the subgroup orders less twice the number of shared elements.

3.2.2 Theory of Matrix Representations

A *matrix representation* of a group $\mathcal{G} = \{g_\ell\}$ consists of a mapping of the group onto $d \times d$ matrices $\overleftrightarrow{\mathbf{\Phi}}(g_\ell) = \overleftrightarrow{\mathbf{\Phi}}_\ell$ such that the group multiplication properties are satisfied under matrix (dot) multiplication. All four group axioms of section 3.2 hold for the matrix representation, notably the existence of an identity and inverse element such that

$$\overleftrightarrow{\mathbf{\Phi}}(\mathcal{E}) = \overleftrightarrow{\mathbf{I}} \tag{3.7}$$

where $\overleftrightarrow{\mathbf{I}}$ is a $d \times d$ identity matrix and

$$\overleftrightarrow{\mathbf{\Phi}}(g_\ell^{-1}) = \left[\overleftrightarrow{\mathbf{\Phi}}_\ell\right]^{-1}. \tag{3.8}$$

A matrix representation is said to be *faithful* if the mapping is one-to-one (i.e. an isomorphism). Matrix representations can correspond to finite or Lie groups, possessing discrete or continuous matrix elements. A given representation $\overleftrightarrow{\mathbf{\Phi}}_\ell$ of a group $\mathcal{G}$ is not unique since one faithful matrix representation can be mapped to a *similar* representation through a *similarity transformation*

$$\overleftrightarrow{\mathbf{\Phi}}_\ell' = \overleftrightarrow{\mathbf{B}} \cdot \overleftrightarrow{\mathbf{\Phi}}_\ell \cdot \left[\overleftrightarrow{\mathbf{B}}\right]^{-1} \tag{3.9}$$

where $\overleftrightarrow{\mathbf{B}}$ is an arbitrary $d \times d$ non-singular matrix. This is to say that in general any given matrix representation of a group $\mathcal{G}$ is not unique.

A matrix representation is a *unitary representation* if the matrices of the representation consist of unitary matrices, that is, the hermitian adjoint of the matrix defined by $\mathbf{A}^{\dagger} = \left[\mathbf{A}^{\mathrm{T}}\right]^{*}$ is equal to the matrix inverse:

$$\left[\overleftrightarrow{\mathbf{\Phi}}_{\ell}\right]^{\dagger} = \left[\overleftrightarrow{\mathbf{\Phi}}_{\ell}\right]^{-1}. \tag{3.10}$$

If a matrix representation satisfies (3.10) and is therefore unitary, then the determinant $\left|\overleftrightarrow{\mathbf{\Phi}}_{\ell}\right| = e^{j\theta}$ where θ is real. The set of all $d \times d$ unitary matrices forms a group $\overleftrightarrow{\mathbf{U}}^{(d)}$ with matrix multiplication as the group operation and satisfies all four axioms of section 3.2.

A further restriction may be enforced on the group if we consider only a subset of the group $\overleftrightarrow{\mathbf{U}}^{(d)}$ that consists of all orthogonal $d \times d$ matrices $\overleftrightarrow{\mathbf{O}}^{(d)}$. Elements of $\overleftrightarrow{\mathbf{O}}^{(d)}$ that satisfy the orthogonality property

$$\left[\overleftrightarrow{\mathbf{\Phi}}_{\ell}\right]^{\mathrm{T}} = \left[\overleftrightarrow{\mathbf{\Phi}}_{\ell}\right]^{-1} \tag{3.11}$$

If a matrix representation satisfies (3.11) then the representation is orthogonal and the determinant is characterized by

$$\left|\overleftrightarrow{\mathbf{\Phi}}_{\ell}\right| = \pm 1, \tag{3.12}$$

Physically, these transformations represent "rotations" and the matrix $\overleftrightarrow{\mathbf{\Phi}}_{\ell}$ is considered to represent a *proper rotation* when the determinant is +1 and an *improper rotation* when the determinant is -1. Only rotations that can be applied to a rigid body are proper rotations. An important ramification of orthogonality is that the application of an orthogonal matrix transformation will not affect the magnitude of the transformed element. This concept is physically appealing because it is often essential that orthogonal transformations do not physically alter the magnitudes of the elements defined in the coordinate system, but only orientation in the coordinate system.

A matrix representation is said to be *reducible* if it can be put into block form as

$$\overleftrightarrow{\mathbf{\Phi}} = \begin{bmatrix} \overleftrightarrow{\mathbf{A}} & \overleftrightarrow{\mathbf{C}} \\ \overleftrightarrow{\mathbf{0}} & \overleftrightarrow{\mathbf{B}} \end{bmatrix} \tag{3.13}$$

through a similarity transformation (3.9) where $\overleftrightarrow{\mathbf{A}}$ is an $n \times n$ matrix, $\overleftrightarrow{\mathbf{B}}$ is a $m \times m$ matrix, $\overleftrightarrow{\mathbf{C}}$ is an $n \times m$ matrix and $\overleftrightarrow{\mathbf{0}}$ is the $m \times n$ null matrix. The original representation has been reduced to representations $\overleftrightarrow{\mathbf{A}}$ and $\overleftrightarrow{\mathbf{B}}$ because

$$\overleftrightarrow{\mathbf{\Phi}}_i \overleftrightarrow{\mathbf{\Phi}}_j = \overleftrightarrow{\mathbf{\Phi}}_k \Rightarrow \begin{cases} \overleftrightarrow{\mathbf{A}}_i \overleftrightarrow{\mathbf{A}}_j = \overleftrightarrow{\mathbf{A}}_k \\ \overleftrightarrow{\mathbf{B}}_i \overleftrightarrow{\mathbf{B}}_j = \overleftrightarrow{\mathbf{B}}_k \end{cases}. \tag{3.14}$$

$\overleftrightarrow{\mathbf{A}}$ and $\overleftrightarrow{\mathbf{B}}$ are said to be reduced representations of $\overleftrightarrow{\mathbf{\Phi}}$. If the representation can not be reduced any further it is said to be *irreducible.*

3.3 Symmetry and Point Groups

The symmetry of a body is prescribed by the set of transformations which preserve the distances between all points on the body and bring the body into coincidence with itself. Any such transformation is a *symmetry group*. In order to preserve the non-morphological properties, the transformations are restricted to rotations about some axis and mirror reflections in the plane. For a body of finite extent, all symmetry transformations must have at least one geometrical point fixed on the body, otherwise, successive transformations will result in the body "walking" through a geometrical translation and the symmetry will not hold. This implies that all axes of rotation and planes of reflection must intersect at a single point which is called the *fixed point.* Group transformations that possess such an intersection point are called *point groups*.

When discussing rotations there are two possible conventions: rotation of the *axes* and rotation of the *object* relative to fixed axes. Axes in R^3 may be rotated with respect to the object through an angle ϕ about a given axis by matrix transformations called *coordinate rotations* given by

x-axis of rotation $$\vec{\mathbf{U}}_x(\phi)=\begin{bmatrix}1 & 0 & 0\\ 0 & \cos(\phi) & -\sin(\phi)\\ 0 & \sin(\phi) & \cos(\phi)\end{bmatrix} \tag{3.15}$$

y-axis of rotation $$\vec{\mathbf{U}}_y(\phi)=\begin{bmatrix}\cos(\phi) & 0 & \sin(\phi)\\ 0 & 1 & 0\\ -\sin(\phi) & 0 & \cos(\phi)\end{bmatrix} \tag{3.16}$$

z-axis of rotation $$\vec{\mathbf{U}}_z(\phi)=\begin{bmatrix}\cos(\phi) & -\sin(\phi) & 0\\ \sin(\phi) & \cos(\phi) & 0\\ 0 & 0 & 1\end{bmatrix}. \tag{3.17}$$

An object in R^3 can be rotated with respect to fixed axes by matrix transformations called *object rotations* through an angle ϕ about a given axis of rotation and can be expressed by the matrix transpose of the corresponding coordinate rotation as given by

x-axis of rotation $$\vec{\mathbf{U}}_{x_o}(\phi)=\left[\vec{\mathbf{U}}_x(\phi)\right]^{\mathrm{T}}=\begin{bmatrix}1 & 0 & 0\\ 0 & \cos(\phi) & \sin(\phi)\\ 0 & -\sin(\phi) & \cos(\phi)\end{bmatrix} \tag{3.18}$$

y-axis of rotation $$\vec{\mathbf{U}}_{y_O}(\phi) = \left[\vec{\mathbf{U}}_y(\phi)\right]^{\mathrm{T}} = \begin{bmatrix} \cos(\phi) & 0 & -\sin(\phi) \\ 0 & 1 & 0 \\ \sin(\phi) & 0 & \cos(\phi) \end{bmatrix} \quad (3.19)$$

z-axis of rotation $$\vec{\mathbf{U}}_{z_O}(\phi) = \left[\vec{\mathbf{U}}_z(\phi)\right]^{\mathrm{T}} = \begin{bmatrix} \cos(\phi) & \sin(\phi) & 0 \\ -\sin(\phi) & \cos(\phi) & 0 \\ 0 & 0 & 1 \end{bmatrix} \quad (3.20)$$

Object rotations operate on the set of all points in the coordinate system so that all points that make up the object are rotated while the coordinate system remains unchanged. Object rotations and coordinate rotations are depicted pictorially for the particular case of rotation about the x-axis in Figure 3.1 below.

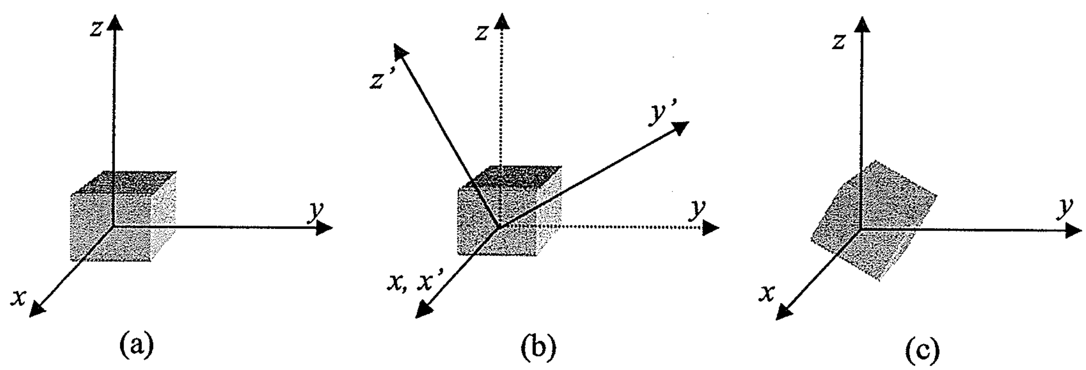

Figure 3.1 Rotation transformations can be considered as rotations of the coordinate system or as rotations of the object: (a) an object before rotation, (b) rotation of the coordinate system, (c) rotation of the object

In general, the rotation matrix is denoted $\vec{\mathbf{U}}$ and is orthogonal according to (3.11) since

$$\left[\vec{\mathbf{U}}(\phi)\right]^{-1} = \left[\vec{\mathbf{U}}(\phi)\right]^{\mathrm{T}}. \quad (3.21)$$

These matrices correspond to proper rotations since $\left|\overleftrightarrow{\mathbf{U}}\right| = 1$ for $0 \leq \phi \leq 2\pi$ so application of a rotation $\overleftrightarrow{\mathbf{U}}$ will not alter the magnitude, only the orientation.

The group of discrete point-rotations (coordinate and object rotations) with respect to an axis of rotation though a finite angle $\phi = 2\pi/M$ has an orthogonal representation denoted as $\overleftrightarrow{\mathbf{C}}_M = \overleftrightarrow{\mathbf{U}}\left(2\pi/_M\right)$. For example, the group of object point-rotations with respect to a z-axis of rotation is written as

$$\overleftrightarrow{\mathbf{C}}_M = \overleftrightarrow{\mathbf{U}}_{z_O}\left(\frac{2\pi}{M}\right) = \begin{bmatrix} \cos\left(\frac{2\pi}{M}\right) & \sin\left(\frac{2\pi}{M}\right) & 0 \\ -\sin\left(\frac{2\pi}{M}\right) & \cos\left(\frac{2\pi}{M}\right) & 0 \\ 0 & 0 & 1 \end{bmatrix}. \tag{3.22}$$

Equation (3.22) is the *generator* for a cyclic group C_M for the particular case of object rotation for a *z*-axis of rotation according to (3.3) since all elements in the group can be generated from powers of the single representation matrix

$$C_M = \left\{\mathcal{E}, C_M, C_M^2, \ldots, C_M^{M-1}\right\}. \tag{3.23}$$

This is to say that the matrix representation $\overleftrightarrow{\mathbf{C}}_M$ represents a rotation transformation through a finite angle of $\phi = 2\pi/M$ and that $\overleftrightarrow{\mathbf{C}}_M^n$ is a rotation though $\phi = n\left(2\pi/M\right)$. The object in Figure 3.2(a) does not have any rotational symmetry (save M =1 rotation, which amounts to an identity rotation). The object in Figure 3.2(b) has C_4 symmetry since any rotation about its *axis of symmetry* by $\phi = 2\pi/4$ will result in an identical object. The object depicted in Figure 3.2(c) also exhibits rotation symmetry since it is invariant under rotations of $\phi = \pi$.

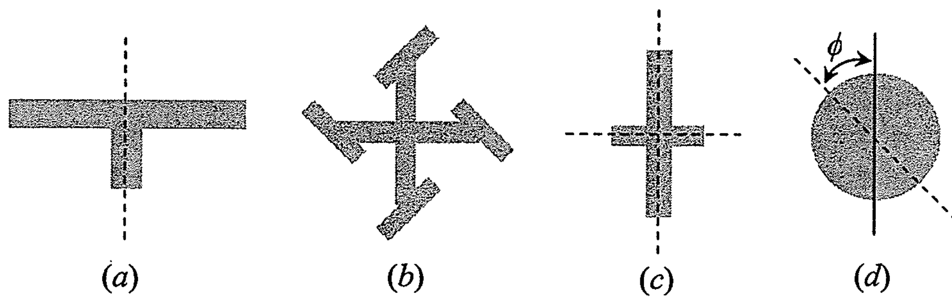

Figure 3.2 Objects with varying degrees of symmetry: (a) Reflection $\mathcal{R}$ symmetry, (b) C_4 rotational symmetry, (c) C_{2a} symmetry, (d) $C_{\infty a}$ symmetry

If an object possesses a *symmetry plane*, or plane of reflection, the object is said to be invariant to *reflections* through the plane. Symmetry by reflection through a symmetry plane is isomorphic to the reflection group denoted $\mathcal{R}$ which are improper rotations. The reflection group $\mathcal{R}$ is said to be cyclic insofar as all group elements are powers of a single element. In the case of $\mathcal{R}$, there are only two elements: the reflection operation $\mathcal{R}$ and the identity element $\mathcal{E}$, so that $\mathcal{R}$ forms a point group of order two denoted by

$$\mathcal{R} = \{R, \mathcal{E}\} = \{R, R^2\} \tag{3.24}$$

where it is interesting to note that $\mathcal{R}$ is its own inverse and that a double reflection is the identity operation. The group of improper rotations that are point reflections can be expressed by matrix representations in R^3. For example, if an object possesses symmetry through reflection about the *x-z* plane the corresponding unitary, orthogonal representation generator is

$$\overleftrightarrow{\mathbf{R}} = \begin{bmatrix} 1 & 0 & 0 \\ 0 & -1 & 0 \\ 0 & 0 & 1 \end{bmatrix} \tag{3.25}$$

Figure 3.2(a) displays an object that possesses $\mathcal{R}$ symmetry with a single plane of symmetry. Conversely, Figure 3.2(b) displays an object that does not possess reflection symmetry at all and is said to be *chiral.* Commonly found objects that possess chiral characteristics include coil-springs and screws. Any attempt to bring an object having gone through a single reflection into coincidence with the original chiral object will result in failure. Figure 3.2(c) displays an object with two planes of symmetry and the object depicted in Figure 3.2(d) has an infinite number of symmetry planes. If rotational symmetry is also exhibited by an object with a symmetry plane, such that the symmetry plane contains the axis of symmetry, the resulting symmetry group is denoted in the notation of Baum [33] as C_{2a}, where the subscript *2a* denotes that the reflection plane includes a C_2 rotation axis. This group is formed by the direct product of the rotation and reflection symmetry groups and is denoted by

$$\begin{aligned} C_M \otimes \mathcal{R} &= C_{Ma} \\ &= \left\{ \mathcal{E}, R, C_M, C_M^2, \ldots, C_M^{M-1}, RC_M, RC_M^2, \ldots, RC_M^{M-1} \right\} \end{aligned} . \tag{3.26}$$

This equation implies that if an object with C_M rotational symmetry possesses a symmetry plane, then the object must possess *M-1* other symmetry planes, since $\left\{ RC_M, RC_M^2, \ldots, RC_M^{M-1} \right\}$ are all symmetry planes that have undergone a rotation.

An object such as the one depicted in Figure 3.2(d) that is in geometric coincidence with itself under a continuous rotation transformation with respect to an axis of rotation is said to be a body of revolution (BOR) and is isomorphic to a continuous Lie group. In the notation of Baum [33] the object is said to possess $C_{\infty a}$ symmetry where the subscript indicates that the rotation symmetry has an infinite order and that its axis of symmetry contains a rotating symmetry plane. For $C_{\infty a}$ symmetry, there are an infinite number of symmetry planes about its axis of symmetry.

3.4 Character Tables

A convenient way to portray a finite group, its elements and the inner workings of its algebra, is by displaying the group in a *character table*. A character table for a finite group of order N is a square $N \times N$ table made up of all possible ways of multiplying two group elements together. The table consists of anterior group elements as column indices and exterior group elements as row indices in order to lay out the table of products.

As an example, consider the C_{4a} symmetry group which consists of elements

$$C_{4a} = \{\mathfrak{E}, R, C_4, C_4^2, C_4^3, RC_4, RC_4^2, RC_4^3\}. \tag{3.27}$$

The character table for this group is exhibited in Table 3.1.

Table 3.1 Character Table for the C_{4a} Symmetry Group

	$\mathfrak{E}$	R	C_4	C_4^2	C_4^3	RC_4	RC_4^2	RC_4^3
$\mathfrak{E}$	$\mathfrak{E}$	R	C_4	C_4^2	C_4^3	RC_4	RC_4^2	RC_4^3
R	R	$\mathfrak{E}$	RC_4	RC_4^2	RC_4^3	C_4	C_4^2	C_4^3
C_4	C_4	RC_4^3	C_4^2	C_4^3	$\mathfrak{E}$	R	RC_4	RC_4^2
C_4^2	C_4^2	RC_4^2	C_4^3	$\mathfrak{E}$	C_4	RC_4^3	R	RC_4
C_4^3	C_4^3	RC_4	$\mathfrak{E}$	C_4	C_4^2	RC_4^2	RC_4^3	R
RC_4	RC_4	C_4^3	RC_4^2	RC_4^3	R	$\mathfrak{E}$	C_4	C_4^2
RC_4^2	RC_4^2	C_4^2	RC_4^3	R	RC_4	C_4^3	$\mathfrak{E}$	C_4
RC_4^3	RC_4^3	C_4	R	RC_4	RC_4^2	C_4^2	C_4^3	$\mathfrak{E}$

Several interesting properties about the group can be seen from inspection of its character table. Every row and every column in the table contains every group element once and only once. The non-commutative nature of the group is exposed since for example, it can be seen that $RC_4 \neq C_4R$.

3.5 Degenerate Solutions and Invariance

If the matrix representations are taken to be linear transformations, we may express the linear transformation of a vector $\vec{\mathbf{r}}$ in R^3 as

$$\vec{\mathbf{r}}' = \overleftrightarrow{\mathbf{\Phi}}_{\ell} \cdot \vec{\mathbf{r}}. \tag{3.28}$$

A *degenerate* case of the group representation occurs when two or more different group elements correspond to an identical transformation of $\vec{\mathbf{r}}$ such that

$$\overleftrightarrow{\mathbf{\Phi}}_i \cdot \vec{\mathbf{r}} = \overleftrightarrow{\mathbf{\Phi}}_j \cdot \vec{\mathbf{r}}, \quad i \neq j. \tag{3.29}$$

Since a group must contain the inverse element of every group element and because of closure, (3.29) may be restated as

$$\vec{\mathbf{r}} = \left(\overleftrightarrow{\mathbf{\Phi}}_i^{-1} \overleftrightarrow{\mathbf{\Phi}}_j \right) \vec{\mathbf{r}} = \overleftrightarrow{\mathbf{\Phi}}_k \vec{\mathbf{r}}. \tag{3.30}$$

where $\overleftrightarrow{\mathbf{\Phi}}_k \neq \overleftrightarrow{\mathbf{I}}$. This equation reveals that under certain circumstances, a group operation on a position vector will not change the vector. For instance, a group rotation about the z-axis will leave any position on the z-axis invariant with respect to the operation. The task is then to find the particular vectors that are invariant with respect to a particular group operation. To accomplish this, consider the eigenvector of the group operation

$$\overleftrightarrow{\mathbf{\Phi}}_k = \lambda \overleftrightarrow{\mathbf{I}} \tag{3.31}$$

where λ is an eigenvalue of the representation matrix. The problem can then be rewritten as

$$\lambda\overleftrightarrow{\mathbf{I}}\bullet\vec{\mathbf{r}} = \vec{\mathbf{r}} \tag{3.32}$$

from which it is apparent that for eigenvalues of unit value ($\lambda = 1$), (3.32) will hold. The eigenvectors of $\overleftrightarrow{\mathbf{\Phi}}_k$ that correspond to $\lambda = 1$ will then satisfy (3.30). These vectors are referred to as *degenerate* vectors and the ones having unity magnitude are denoted by $\vec{\mathbf{r}} = \hat{\mathbf{r}}_{dk}$, i.e. they are unit vectors. Degenerate vectors of $\overleftrightarrow{\mathbf{\Phi}}_k$ satisfy (3.30)

$$\overleftrightarrow{\mathbf{\Phi}}_k\bullet\hat{\mathbf{r}}_{dk} = \hat{\mathbf{r}}_{dk}\,. \tag{3.33}$$

The unit vector solutions can be made to have arbitrary magnitude by multiplication with a scalar. For a given $d \times d$ matrix, there may exist up to d different eigenvalues λ. When less than d different eigenvalues exist and there are n identical eigenvalues (for example, two unit valued eigenvalues) the transformation is said to be n-fold degenerate and the eigenvectors corresponding to these identical eigenvalues will be orthogonal [36]. This implies that any linear combination of n degenerate vectors from an n-fold degenerate matrix transformation will be itself degenerate

$$\overleftrightarrow{\mathbf{\Phi}}_k\left[a_1\left(\hat{\mathbf{r}}_{dn}\right)_1 + a_2\left(\hat{\mathbf{r}}_{dn}\right)_2 + \ldots + a_n\left(\hat{\mathbf{r}}_{dn}\right)_n\right] = a_1\left(\hat{\mathbf{r}}_{dn}\right)_1 + a_2\left(\hat{\mathbf{r}}_{dn}\right)_2 + \ldots + a_n\left(\hat{\mathbf{r}}_{dn}\right)_n \tag{3.34}$$

where a_1, a_2,..., a_n are arbitrary scalars.

As an example, consider the case of C_{4a} symmetry with group elements given by (3.27) where the rotation axis coincides with the z-axis as depicted in Figure 3.3. The symmetry plane can be thought of as initially in the *x-z* plane such that the matrix generators for this group can be represented as

$$\overleftrightarrow{\mathbf{R}} = \begin{bmatrix} 1 & 0 & 0 \\ 0 & -1 & 0 \\ 0 & 0 & 1 \end{bmatrix}, \quad \overleftrightarrow{\mathbf{C}}_4 = \overleftrightarrow{\mathbf{U}}_{z_o}\left(\frac{2\pi}{4}\right) = \begin{bmatrix} 0 & 1 & 0 \\ -1 & 0 & 0 \\ 0 & 0 & 1 \end{bmatrix}. \tag{3.35}$$

where the rotation operation is an object rotation.

Several degenerate solutions exist for this symmetry such that a given symmetry operation will leave the degenerate vectors invariant. For example, the symmetry operation RC_4^2 has the matrix representation

$$\overleftrightarrow{\mathbf{RC}_4^2} = \begin{bmatrix} -1 & 0 & 0 \\ 0 & 1 & 0 \\ 0 & 0 & 1 \end{bmatrix}. \tag{3.36}$$

The matrix transformation $\overleftrightarrow{\mathbf{RC}_4^2}$ is 2-fold degenerate with two unity valued eigenvalues that correspond to two orthogonal eigenvectors:

$$\begin{aligned} (\hat{\mathbf{r}}_{dn})_1 &= \hat{\mathbf{e}}_y \\ (\hat{\mathbf{r}}_{dn})_2 &= \hat{\mathbf{e}}_z \end{aligned}. \tag{3.37}$$

The degeneracy for an improper rotation operation is always a two-fold degeneracy.

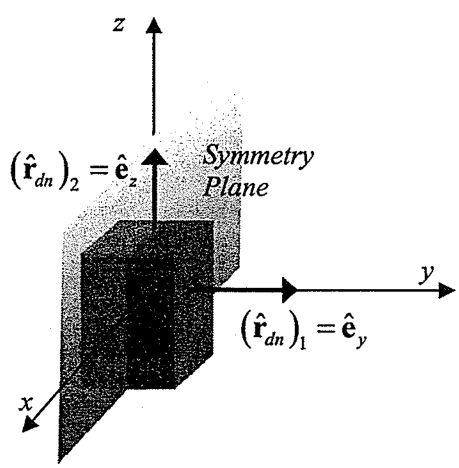

Figure 3.3 Object with C_{4a} Symmetry with respect to the *x-y* plane

It is easy to verify that these degenerate vectors do indeed observe the property in (3.34), that is

$$\overleftrightarrow{\mathbf{RC}_4^2}\bullet\left[a\hat{\mathbf{e}}_y + b\hat{\mathbf{e}}_z\right] = a\hat{\mathbf{e}}_x + b\hat{\mathbf{e}}_z \,. \tag{3.38}$$

This equation suggests that any position on the *y-z* plane will be degenerate under the $\overleftrightarrow{\mathbf{RC}_4^2}$ symmetry operation.

Other degenerate vectors exist for the C_{4a} symmetry group that correspond to other group elements. One of the most useful degenerate geometries is the one that corresponds to a pure reflection operation. For example, the degenerate unit vectors that correspond to a pure reflection $\overleftrightarrow{\mathbf{R}}$ through the *x-z* plane as in (3.25) are

$$\begin{aligned}(\hat{\mathbf{r}}_{dn})_1 &= \hat{\mathbf{e}}_x \\ (\hat{\mathbf{r}}_{dn})_2 &= \hat{\mathbf{e}}_z\end{aligned} \tag{3.39}$$

which through a similar relation as in (3.38) can be shown to correspond to an arbitrary position on the symmetry plane in question. *Degenerate vectors that correspond to pure reflections are arbitrary vectors on the symmetry plane.*

CHAPTER 4

Target Symmetry and Scattering

4.1 Electromagnetic Symmetry Planes and Rotations

Consider an electromagnetic symmetry plane defined by a normal unit vector $\hat{\mathbf{n}}$ and a point p such that all electromagnetic constitutive parameters, $\sigma(\vec{\mathbf{r}})$, $\varepsilon(\vec{\mathbf{r}})$ and $\mu(\vec{\mathbf{r}})$ are reflection symmetric with respect to this plane. Figure 4.1 shows the particular case when $\hat{\mathbf{n}} = \hat{\mathbf{e}}_y$ and $p = \langle 0,0,0 \rangle$ so that the symmetry plane is the x-z plane and includes the coordinate origin. It is convenient to select the coordinate origin as the fixed point when dealing with point groups and representations.

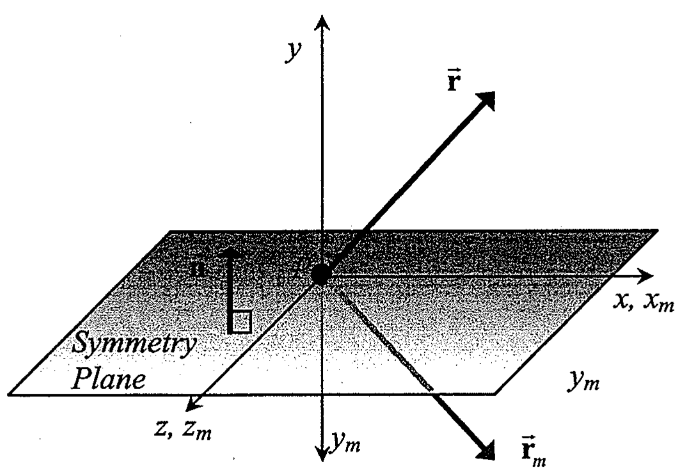

Figure 4.1 A symmetry plane with a position vector reflected through it

For such a system, the general position vector in Cartesian coordinates is given by

$$\vec{\mathbf{r}} = x\hat{\mathbf{e}}_x + y\hat{\mathbf{e}}_y + z\hat{\mathbf{e}}_z . \tag{4.1}$$

Given this position vector it is possible to define a mirror reflection position vector with respect to $\vec{\mathbf{r}}$ and the electromagnetic symmetry plane:

$$\vec{\mathbf{r}}_m = x\hat{\mathbf{e}}_x - y\hat{\mathbf{e}}_y + z\hat{\mathbf{e}}_z . \tag{4.2}$$

The reflection symmetry can be denoted by a matrix representation in the Group theoretical sense by equation (3.25) which is restated here as

$$\overleftrightarrow{\mathbf{R}} = \begin{bmatrix} 1 & 0 & 0 \\ 0 & -1 & 0 \\ 0 & 0 & 1 \end{bmatrix}. \tag{4.3}$$

This provides for the formal derivation of $\vec{\mathbf{r}}$ with respect to $\vec{\mathbf{r}}_m$ and vice versa as

$$\vec{\mathbf{r}}_m = \overleftrightarrow{\mathbf{R}} \bullet \vec{\mathbf{r}} \tag{4.4}$$

$$\vec{\mathbf{r}} = \overleftrightarrow{\mathbf{R}} \bullet \vec{\mathbf{r}}_m \tag{4.5}$$

A vector $\vec{\mathbf{r}}$ positioned arbitrarily in R^3 can always be considered as the difference between two vectors that originate at the basis origin so that $\vec{\mathbf{r}} = \vec{\mathbf{r}}_2 - \vec{\mathbf{r}}_1$ since

$$\begin{aligned} \vec{\mathbf{r}}_m &= \overleftrightarrow{\mathbf{R}} \bullet \vec{\mathbf{r}} = \overleftrightarrow{\mathbf{R}} \bullet (\vec{\mathbf{r}}_2 - \vec{\mathbf{r}}_1) \\ &= \overleftrightarrow{\mathbf{R}} \bullet \vec{\mathbf{r}}_2 - \overleftrightarrow{\mathbf{R}} \bullet \vec{\mathbf{r}}_1 \\ &= \vec{\mathbf{r}}_{m2} - \vec{\mathbf{r}}_{m1} \end{aligned} \quad . \tag{4.6}$$

This principle is shown graphically in Figure 4.2.

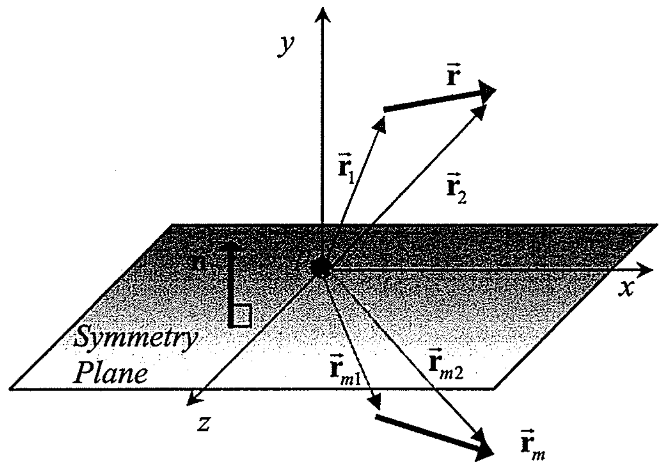

Figure 4.2 An arbitrary vector in R^3 reflected through a symmetry plane

The reflected position vector $\vec{\mathbf{r}}_m$ may be considered either as a new position vector located in a reflected location with respect to the symmetry plane or as an identical position vector located in a reflected coordinate system $\langle \hat{\mathbf{e}}_{x_m}, \hat{\mathbf{e}}_{y_m}, \hat{\mathbf{e}}_{z_m} \rangle$. From the perspective of a casual observer, observations taken at positions $\vec{\mathbf{r}}$ and $\vec{\mathbf{r}}_m$ will produce identical results (as will observations taken in either coordinate systems) since the medium under observation is reflection symmetric about the electromagnetic symmetry plane. Stated formally the scalar constitutive parameters satisfy

$$\begin{aligned} \sigma(\vec{\mathbf{r}}) &= \sigma\left(\overleftrightarrow{\mathbf{R}}\bullet\vec{\mathbf{r}}\right) = \sigma(\vec{\mathbf{r}}_m) \\ \varepsilon(\vec{\mathbf{r}}) &= \varepsilon\left(\overleftrightarrow{\mathbf{R}}\bullet\vec{\mathbf{r}}\right) = \varepsilon(\vec{\mathbf{r}}_m) \\ \mu(\vec{\mathbf{r}}) &= \mu\left(\overleftrightarrow{\mathbf{R}}\bullet\vec{\mathbf{r}}\right) = \mu(\vec{\mathbf{r}}_m) \end{aligned} \quad . \tag{4.7}$$

The selection of the *x-z* plane does not detract from the generality of the results but is made only for convenience. The symmetry plane and all of the following arguments can be rotated through the appropriate rotation transformations $\overleftrightarrow{\mathbf{U}}$ in equations (3.18)-

(3.20) to represent a symmetry plane with an arbitrary normal vector. A position vector ($\vec{\mathbf{r}}$ or $\vec{\mathbf{r}}_m$) rotated by a rotation transformation is given by

$$\vec{\mathbf{r}}' = \overleftrightarrow{\mathbf{U}} \bullet \vec{\mathbf{r}} \tag{4.8}$$

$$\vec{\mathbf{r}}'_m = \overleftrightarrow{\mathbf{U}} \bullet \vec{\mathbf{r}}_m \tag{4.9}$$

Again this matrix transformation applies to any arbitrary vector, not necessarily originating at the coordinate origin. Let $\vec{\mathbf{r}} = \vec{\mathbf{r}}_2 - \vec{\mathbf{r}}_1$, then

$$\begin{aligned} \vec{\mathbf{r}}' &= \overleftrightarrow{\mathbf{U}} \bullet \vec{\mathbf{r}} = \overleftrightarrow{\mathbf{U}} \bullet \left(\vec{\mathbf{r}}_2 - \vec{\mathbf{r}}_1\right) \\ &= \overleftrightarrow{\mathbf{U}} \bullet \vec{\mathbf{r}}_2 - \overleftrightarrow{\mathbf{U}} \bullet \vec{\mathbf{r}}_1 \\ &= \vec{\mathbf{r}}'_2 - \vec{\mathbf{r}}'_1 \end{aligned} \tag{4.10}$$

and $\vec{\mathbf{r}}'$ is the difference between the rotated components $\vec{\mathbf{r}}'_1$ and $\vec{\mathbf{r}}'_2$.

The rotated position vector $\vec{\mathbf{r}}'$ may be considered either as a new position vector located in a rotated location with respect to $\vec{\mathbf{r}}$ or as an identical position vector located in a rotated coordinate system $\left\langle \hat{\mathbf{e}}_{x'}, \hat{\mathbf{e}}_{y'}, \hat{\mathbf{e}}_{z'} \right\rangle$.

Applying this to (4.4) or (4.5) gives

$$\begin{aligned} \vec{\mathbf{r}}'_m &= \overleftrightarrow{\mathbf{U}} \bullet \vec{\mathbf{r}}_m = \overleftrightarrow{\mathbf{U}} \bullet \overleftrightarrow{\mathbf{R}} \bullet \vec{\mathbf{r}} \\ &= \left(\overleftrightarrow{\mathbf{U}} \bullet \overleftrightarrow{\mathbf{R}} \bullet \overleftrightarrow{\mathbf{U}}^{-1}\right) \bullet \overleftrightarrow{\mathbf{U}} \bullet \vec{\mathbf{r}} \\ &= \overleftrightarrow{\mathbf{R}}' \bullet \vec{\mathbf{r}}' \end{aligned} \tag{4.11}$$

where $\overleftrightarrow{\mathbf{R}}' = \overleftrightarrow{\mathbf{U}} \bullet \overleftrightarrow{\mathbf{R}} \bullet \overleftrightarrow{\mathbf{U}}^{-1}$ is a similarity transformation of the symmetry plane so that the rotated position vector $\vec{\mathbf{r}}'$ is reflected through the rotated symmetry plane defined by the unit normal vector $\hat{\mathbf{n}}' = \overleftrightarrow{\mathbf{U}} \bullet \hat{\mathbf{n}} = \overleftrightarrow{\mathbf{U}} \bullet \hat{\mathbf{e}}_y$ and fixed point $p = \langle 0,0,0 \rangle$ to form a rotated reflected vector $\vec{\mathbf{r}}'_m$. The proof that this transformation applies to vectors with arbitrary origin follows immediately from (4.6) and (4.11) and will not be repeated.

Consider the example shown in Figure 4.3. If the symmetry plane with $\hat{\mathbf{n}} = \hat{\mathbf{e}}_y$ is rotated by $\pi/4$ about the z-axis, the corresponding object rotation transformation matrix according to (3.20) is

$$\vec{\mathbf{U}}_{zo}\left(\pi/4\right) = \frac{\sqrt{2}}{2}\begin{bmatrix} 1 & 1 & 0 \\ -1 & 1 & 0 \\ 0 & 0 & \sqrt{2} \end{bmatrix}. \tag{4.12}$$

The unit normal becomes

$$\hat{\mathbf{n}}' = \vec{\mathbf{U}}_{zo}\left(\pi/4\right)\bullet\hat{\mathbf{n}} = \frac{\sqrt{2}}{2}\left(\hat{\mathbf{e}}_x + \hat{\mathbf{e}}_y\right) \tag{4.13}$$

The rotated reflection matrix becomes

$$\begin{aligned} \vec{\mathbf{R}}' &= \vec{\mathbf{U}}_{zo}\left(\pi/4\right)\bullet\vec{\mathbf{R}}\bullet\left[\vec{\mathbf{U}}_{zo}\left(\pi/4\right)\right]^{-1} \\ &= \begin{bmatrix} 0 & -1 & 0 \\ -1 & 0 & 0 \\ 0 & 0 & 1 \end{bmatrix} \end{aligned} \tag{4.14}$$

The position vectors $\vec{\mathbf{r}}$ and $\vec{\mathbf{r}}_m$ become

$$\vec{\mathbf{r}}' = \vec{\mathbf{U}}_{zo}\left(\pi/4\right)\bullet\vec{\mathbf{r}} = \frac{\sqrt{2}}{2}(x+y)\hat{\mathbf{e}}_x + \frac{\sqrt{2}}{2}(x+y)\hat{\mathbf{e}}_y + z\hat{\mathbf{e}}_z \tag{4.15}$$

$$\vec{\mathbf{r}}'_m = \vec{\mathbf{R}}'\bullet\vec{\mathbf{r}}' = \frac{\sqrt{2}}{2}(x-y)\hat{\mathbf{e}}_x - \frac{\sqrt{2}}{2}(x+y)\hat{\mathbf{e}}_y + z\hat{\mathbf{e}}_z \tag{4.16}$$

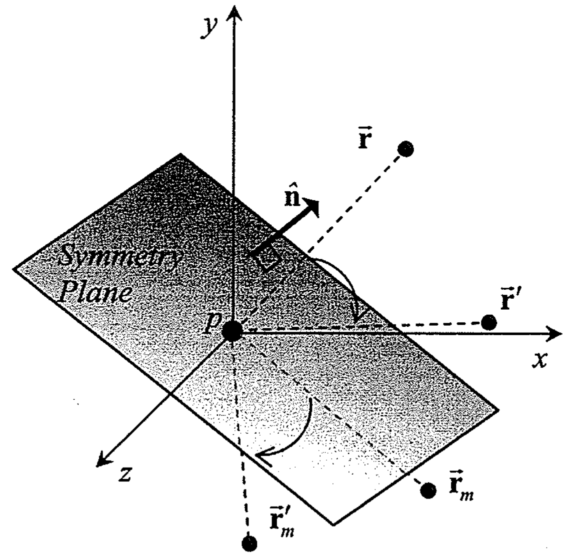

Figure 4.3 $\overleftrightarrow{\mathbf{U}}_{z_0}(\pi/4)$ rotation (object rotation) of a symmetry plane in R^3

If rotational symmetry exists then the scalar constitutive parameters are also invariant to the group rotation operation. If the rotation matrix $\overleftrightarrow{\mathbf{U}}$ in (4.8) is a symmetry group rotation C_M (continuous or discrete) $1 \le M \le \infty$ with matrix representation $\overleftrightarrow{\mathbf{C}}_M$, then the constitutive parameters will satisfy

$$\begin{aligned} \sigma(\vec{\mathbf{r}}) &= \sigma\left(\overleftrightarrow{\mathbf{C}}_M \bullet \vec{\mathbf{r}}\right) = \sigma(\vec{\mathbf{r}}_M) \\ \varepsilon(\vec{\mathbf{r}}) &= \varepsilon\left(\overleftrightarrow{\mathbf{C}}_M \bullet \vec{\mathbf{r}}\right) = \varepsilon(\vec{\mathbf{r}}_M) \ , \\ \mu(\vec{\mathbf{r}}) &= \mu\left(\overleftrightarrow{\mathbf{C}}_M \bullet \vec{\mathbf{r}}\right) = \mu(\vec{\mathbf{r}}_M) \end{aligned} \tag{4.17}$$

where $\vec{\mathbf{r}}_M = \overleftrightarrow{\mathbf{C}}_M \bullet \vec{\mathbf{r}}$ is a position vector rotated through a group symmetry rotation. For achiral media with C_{Ma} (or $C_{\infty a}$ symmetry) there is both reflection and rotational symmetry so that the constitutive parameters satisfy

$$\begin{aligned} \sigma(\vec{\mathbf{r}}) &= \sigma(\vec{\mathbf{r}}_M) = \sigma(\vec{\mathbf{r}}_m) = \sigma(\vec{\mathbf{r}}_{Mm}) \\ \varepsilon(\vec{\mathbf{r}}) &= \varepsilon(\vec{\mathbf{r}}_M) = \varepsilon(\vec{\mathbf{r}}_m) = \varepsilon(\vec{\mathbf{r}}_{Mm}) \\ \mu(\vec{\mathbf{r}}) &= \mu(\vec{\mathbf{r}}_M) = \mu(\vec{\mathbf{r}}_m) = \mu(\vec{\mathbf{r}}_{Mm}) \end{aligned} \tag{4.18}$$

where $\vec{\mathbf{r}}_{Mm} = \overleftrightarrow{\mathbf{C}}_M \bullet \overleftrightarrow{\mathbf{R}} \bullet \vec{\mathbf{r}}$ is a position vector rotated through a group rotation operation and reflected through a symmetry plane and the subscripts *Mm* denote that the vector has undergone a rotation through $2\pi/M$ and a "mirrored" reflection. The relationships of (4.18) state that the constitutive parameters of an object with C_{Ma} symmetry are invariant to all operations of the C_{Ma} group. Analogously, this relationship shows that for C_{Ma} symmetry, knowledge of the constitutive parameters from a single observation implies knowledge from $2M\text{-}1$ other observations due to the symmetry.

Consider Figure 4.4 which depicts a two dimensional object with C_{4a} symmetry such that the object (as well as its reflection symmetry plane) is invariant to 90° rotations. From a measurement of the object at position $\vec{\mathbf{r}}$, a mirror reflected observation across the object's symmetry plane can be deduced at location $\vec{\mathbf{r}}_m$. Furthermore, rotation of the object by $\phi = 90°$ will bring the object into coincidence with itself such that post-rotation observations made at $\vec{\mathbf{r}}$ or $\vec{\mathbf{r}}_m$ will be invariant. For an object with C_{4a} symmetry, a single measurement at $\vec{\mathbf{r}}$ yields valuable information at 7 other locations, all symmetric rotations and reflections. If the electromagnetic constitutive parameters of the object were being measured by some suitable device, it is reasonable to expect that a measurement taken at location $\vec{\mathbf{r}}$ will be reflected with respect to a measurement taken at location $\vec{\mathbf{r}}_m$ and that any attempt to rotate the object by an integer multiple of 90° will again reproduce identical measurements. However devices that directly measure the constitutive parameters of materials are not practical and these parameters are in general measured indirectly by electromagnetic fields.

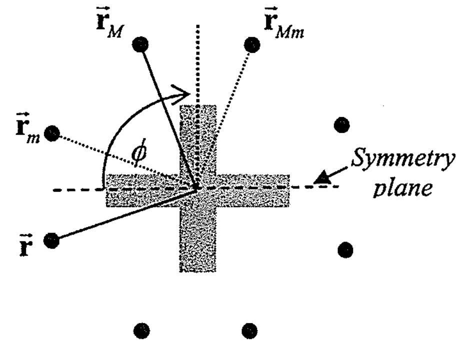

Figure 4.4 The effects of various group operations on a position vector $\vec{\mathbf{r}}$: $\vec{\mathbf{r}}_m$ is a reflection through the symmetry plane, $\vec{\mathbf{r}}_M$ is a rotation through $2\pi/M$ and $\vec{\mathbf{r}}_{Mm}$ is a reflection followed by a rotation through $2\pi/M$.

4.2 Decomposition of Electromagnetic Scattering Into Symmetric and Antisymmetric Components

If a symmetry exists in a medium, it can be shown that a given electromagnetic phenomenon will manifest itself symmetrically as well. If a symmetry plane exists, we may define the mirrored electromagnetic components as [37]

$$\vec{\mathbf{E}}_m(\vec{\mathbf{r}},f)=\overleftrightarrow{\mathbf{R}}\cdot\vec{\mathbf{E}}(\vec{\mathbf{r}}_m,f) \tag{4.19}$$

$$\vec{\mathbf{H}}_m(\vec{\mathbf{r}},f)=-\overleftrightarrow{\mathbf{R}}\cdot\vec{\mathbf{H}}(\vec{\mathbf{r}}_m,f) \tag{4.20}$$

$$\vec{\mathbf{J}}_m(\vec{\mathbf{r}},f)=\overleftrightarrow{\mathbf{R}}\cdot\vec{\mathbf{J}}(\vec{\mathbf{r}}_m,f) \tag{4.21}$$

$$\rho_m(\vec{\mathbf{r}},f)=\rho(\vec{\mathbf{r}}_m,f). \tag{4.22}$$

The sign change in the reflected magnetic field (4.20) compensates for the chiral qualities in the solenoidal characteristic of the magnetic field with respect to the electric field whereby the solenoidal properties of the magnetic fields are inverted in the reflection. This is akin to observing that a right-handed screw appears as a left-handed screw in a mirror. The signs can be reversed for the reflected components in equations (4.19)-(4.22) and the equations would still be consistent. However, it is convenient to maintain the stated sign convention since the scalar quantity ρ exhibits no sign change in its reflection [37].

Equations (4.19) through (4.22) must satisfy Maxwell's equations to be valid representations of electromagnetic phenomena reflected through a symmetry plane. Dropping the frequency variable again, the curl relationship in (2.25) is satisfied since[37]

$$\begin{aligned}
\nabla\times\vec{\mathbf{E}}_m(\vec{\mathbf{r}}) &= \begin{vmatrix} \hat{\mathbf{e}}_x & \hat{\mathbf{e}}_y & \hat{\mathbf{e}}_z \\ \partial/\partial x & \partial/\partial y & \partial/\partial z \\ \left(E_m(\vec{\mathbf{r}})\right)_x & \left(E_m(\vec{\mathbf{r}})\right)_y & \left(E_m(\vec{\mathbf{r}})\right)_z \end{vmatrix} \\
&= -\vec{\vec{\mathbf{R}}}\bullet \begin{vmatrix} \hat{\mathbf{e}}_x & \hat{\mathbf{e}}_y & \hat{\mathbf{e}}_z \\ \partial/\partial x_m & \partial/\partial y_m & \partial/\partial z_m \\ \left(E(\vec{\mathbf{r}}_m)\right)_x & \left(E(\vec{\mathbf{r}}_m)\right)_y & \left(E(\vec{\mathbf{r}}_m)\right)_z \end{vmatrix}. \\
&= j\omega\mu\vec{\vec{\mathbf{R}}}\bullet\vec{\mathbf{H}}(\vec{\mathbf{r}}_m) \\
&= -j\omega\mu\vec{\mathbf{H}}_m(\vec{\mathbf{r}})
\end{aligned} \tag{4.23}$$

Similarly (2.26) is satisfied since

$$\begin{aligned}
\nabla\times\vec{\mathbf{H}}_m(\vec{\mathbf{r}}) &= \begin{vmatrix} \hat{\mathbf{e}}_x & \hat{\mathbf{e}}_y & \hat{\mathbf{e}}_z \\ \partial/\partial x & \partial/\partial y & \partial/\partial z \\ \left(H_m(\vec{\mathbf{r}})\right)_x & \left(H_m(\vec{\mathbf{r}})\right)_y & \left(H_m(\vec{\mathbf{r}})\right)_z \end{vmatrix} \\
&= \vec{\vec{\mathbf{R}}}\bullet \begin{vmatrix} \hat{\mathbf{e}}_x & \hat{\mathbf{e}}_y & \hat{\mathbf{e}}_z \\ \partial/\partial x_m & \partial/\partial y_m & \partial/\partial z_m \\ \left(H(\vec{\mathbf{r}}_m)\right)_x & \left(H(\vec{\mathbf{r}}_m)\right)_y & \left(H(\vec{\mathbf{r}}_m)\right)_z \end{vmatrix}
\end{aligned}$$

$$
\begin{aligned}
&= \overleftrightarrow{\mathbf{R}} \cdot \vec{\mathbf{J}}(\vec{\mathbf{r}}_m) + (\sigma + j\omega)\overleftrightarrow{\mathbf{R}} \cdot \vec{\mathbf{E}}(\vec{\mathbf{r}}_m) \\
&= \vec{\mathbf{J}}_m(\vec{\mathbf{r}}) + (\sigma + j\omega)\vec{\mathbf{E}}_m(\vec{\mathbf{r}})
\end{aligned}
\tag{4.24}
$$

The continuity equation (2.27) is satisfied because

$$
\begin{aligned}
-j\omega\rho_m(\vec{\mathbf{r}}) &= \nabla \cdot \vec{\mathbf{J}}_m(\vec{\mathbf{r}}) \\
&= \frac{\partial}{\partial x}\vec{\mathbf{J}}_m(\vec{\mathbf{r}}) + \frac{\partial}{\partial y}\vec{\mathbf{J}}_m(\vec{\mathbf{r}}) + \frac{\partial}{\partial z}\vec{\mathbf{J}}_m(\vec{\mathbf{r}}) \\
&= \frac{\partial}{\partial x_m}\vec{\mathbf{J}}(\vec{\mathbf{r}}_m) + \frac{\partial}{\partial y_m}\vec{\mathbf{J}}(\vec{\mathbf{r}}_m) + \frac{\partial}{\partial z_m}\vec{\mathbf{J}}(\vec{\mathbf{r}}_m) \\
&= -j\omega\rho(\vec{\mathbf{r}}_m)
\end{aligned}
, \tag{4.25}
$$

which is as in (4.22).

Equations (4.23) through (4.25) show that if a symmetry plane exists and a measurement is taken at position $\vec{\mathbf{r}}$, the reflected electromagnetic fields produced by charges and currents can be deduced at $\vec{\mathbf{r}}_m$ without physically measuring the fields at $\vec{\mathbf{r}}_m$.

The symmetric and antisymmetric field quantities can now be defined in terms of contributions from measurements taken on either side of a symmetry plane. Consider Figure 4.5 where an object with a symmetry plane is measured at two locations $\vec{\mathbf{r}}$ and $\vec{\mathbf{r}}_m$ on either side of a symmetry plane *S*. The excitations are in the form of an electric field $\vec{\mathbf{E}}^{(i)}(\vec{\mathbf{r}})$ when measuring at $\vec{\mathbf{r}}$ and $\vec{\mathbf{E}}_m^{(i)}(\vec{\mathbf{r}}) = \overleftrightarrow{\mathbf{R}} \cdot \vec{\mathbf{E}}^{(i)}(\vec{\mathbf{r}}_m)$ when measuring at $\vec{\mathbf{r}}_m$.

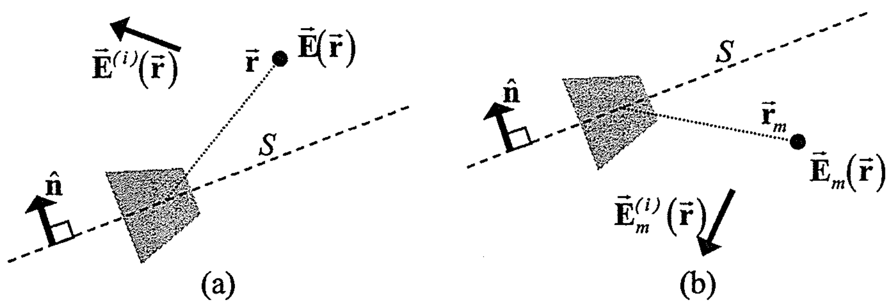

Figure 4.5 Measurement of an object with respect to its symmetry plane: (a) The system is initially excited by $\vec{\mathbf{E}}^{(i)}(\vec{\mathbf{r}})$ and measured at $\vec{\mathbf{r}}$, (b) The entire system is then reflected across S for the second measurement.

The symmetric components for the measured fields are denoted $\vec{\mathbf{E}}_{sy}$ and $\vec{\mathbf{H}}_{sy}$ and are derived from the measured fields $\vec{\mathbf{E}}$, $\vec{\mathbf{E}}_m$, $\vec{\mathbf{H}}$ and $\vec{\mathbf{H}}_m$ as follows [37]:

$$\vec{\mathbf{E}}_{sy}(\vec{\mathbf{r}})=\frac{1}{2}\left\{\vec{\mathbf{E}}(\vec{\mathbf{r}})+\vec{\mathbf{E}}_m(\vec{\mathbf{r}})\right\}=\frac{1}{2}\left\{\vec{\mathbf{E}}(\vec{\mathbf{r}})+\vec{\mathbf{R}}\cdot\vec{\mathbf{E}}(\vec{\mathbf{r}}_m)\right\}, \tag{4.26}$$

$$\vec{\mathbf{H}}_{sy}(\vec{\mathbf{r}})=\frac{1}{2}\left\{\vec{\mathbf{H}}(\vec{\mathbf{r}})+\vec{\mathbf{H}}_m(\vec{\mathbf{r}})\right\}=\frac{1}{2}\left\{\vec{\mathbf{H}}(\vec{\mathbf{r}})-\vec{\mathbf{R}}\cdot\vec{\mathbf{H}}(\vec{\mathbf{r}}_m)\right\}. \tag{4.27}$$

The antisymmetric parts of the scattered fields are denoted by $\vec{\mathbf{E}}_{as}$ and $\vec{\mathbf{H}}_{as}$ and are

$$\vec{\mathbf{E}}_{as}(\vec{\mathbf{r}})=\frac{1}{2}\left\{\vec{\mathbf{E}}(\vec{\mathbf{r}})-\vec{\mathbf{E}}_m(\vec{\mathbf{r}})\right\}=\frac{1}{2}\left\{\vec{\mathbf{E}}(\vec{\mathbf{r}})-\vec{\mathbf{R}}\cdot\vec{\mathbf{E}}(\vec{\mathbf{r}}_m)\right\}, \tag{4.28}$$

$$\vec{\mathbf{H}}_{as}(\vec{\mathbf{r}})=\frac{1}{2}\left\{\vec{\mathbf{H}}(\vec{\mathbf{r}})-\vec{\mathbf{H}}_m(\vec{\mathbf{r}})\right\}=\frac{1}{2}\left\{\vec{\mathbf{H}}(\vec{\mathbf{r}})+\vec{\mathbf{R}}\cdot\vec{\mathbf{H}}(\vec{\mathbf{r}}_m)\right\}. \tag{4.29}$$

In general the total scattered fields can be reconstructed by:

$$\vec{\mathbf{E}}(\vec{\mathbf{r}})=\vec{\mathbf{E}}_{sy}(\vec{\mathbf{r}})+\vec{\mathbf{E}}_{as}(\vec{\mathbf{r}}), \tag{4.30}$$

$$\vec{\mathbf{H}}(\vec{\mathbf{r}})=\vec{\mathbf{H}}_{sy}(\vec{\mathbf{r}})+\vec{\mathbf{H}}_{as}(\vec{\mathbf{r}}). \tag{4.31}$$

These equations show that if measurements are taken at a location $\vec{\mathbf{r}}$ and at a mirror reflected location $\vec{\mathbf{r}}_m$ with respect to a reflection symmetry operation $\mathcal{R}$, the measured electric and magnetic fields may be decomposed into symmetric and antisymmetric components. It should be noted that "*antisymmetric*" does not imply "*asymmetric*" since these two terms are mutually exclusive. The antisymmetric condition implies that the field components at $\vec{\mathbf{r}}$ and $\vec{\mathbf{r}}_m$ are the same but with opposite signs. Asymmetry implies that no fundamental relationship exists at all between the components. Furthermore the equations suggest that if S is in fact a true symmetry plane with respect to $\vec{\mathbf{r}}$ and $\vec{\mathbf{r}}_m$ then

$$\begin{aligned}\vec{\mathbf{E}}(\vec{\mathbf{r}}) &= \vec{\mathbf{E}}_m(\vec{\mathbf{r}}) = \overleftrightarrow{\mathbf{R}}\bullet\vec{\mathbf{E}}\left(\overleftrightarrow{\mathbf{R}}\bullet\vec{\mathbf{r}}\right) \\ \vec{\mathbf{H}}(\vec{\mathbf{r}}) &= \vec{\mathbf{H}}_m(\vec{\mathbf{r}}) = -\overleftrightarrow{\mathbf{R}}\bullet\vec{\mathbf{H}}\left(\overleftrightarrow{\mathbf{R}}\bullet\vec{\mathbf{r}}\right)\end{aligned} \tag{4.32}$$

so that

$$\begin{aligned}\vec{\mathbf{E}}_{sy}(\vec{\mathbf{r}}) &= \vec{\mathbf{E}}(\vec{\mathbf{r}}) \\ \vec{\mathbf{H}}_{sy}(\vec{\mathbf{r}}) &= \vec{\mathbf{H}}(\vec{\mathbf{r}})\end{aligned} \tag{4.33}$$

and

$$\vec{\mathbf{E}}_{as}(\vec{\mathbf{r}}) = \vec{\mathbf{H}}_{as}(\vec{\mathbf{r}}) = 0 \tag{4.34}$$

and only the symmetric components are non-zero. The converse of these conditions however are not necessarily true since (4.32) through (4.34) will also be satisfied if no scatterer is present at all.

If the symmetry plane S is not chosen correctly or if no such symmetry plane exists, then the symmetric and antisymmetric field components will both have nonzero contributions.

Furthermore, these conditions can only be considered as general guidelines since any realistic measurements will surely result in a finite, non-zero antisymmetric component even when a symmetry plane is present due to the non-ideal nature of the measurement. Moreover, there may be various cases where the constitutive parameters vary only slightly and have little effect on the resulting scattered fields over large parts of the volume under investigation. If these features are not symmetric as required by (4.7), one might still invoke the symmetry decomposition as an approximation. In general, all target scatterers will possess nonzero symmetric and antisymmetric components. Despite these deficiencies, the conditions outlined in (4.32) through (4.34) will be taken as a convenient measure of the presence of a symmetry plane.

4.3 Symmetric and Antisymmetric Responses In The Presence of C_M and C_{Ma} Symmetry

The concept of symmetric and antisymmetric fields may be expanded to include the existence of C_M rotational symmetry by invoking the results of (4.18).

$$\vec{\mathbf{E}}_M(\vec{\mathbf{r}}) = \overleftrightarrow{\mathbf{C}}_M \bullet \vec{\mathbf{E}}(\vec{\mathbf{r}}_M) \tag{4.35}$$

$$\vec{\mathbf{H}}_M(\vec{\mathbf{r}}) = \overleftrightarrow{\mathbf{C}}_M \bullet \vec{\mathbf{H}}(\vec{\mathbf{r}}_M) \tag{4.36}$$

$$\vec{\mathbf{J}}_M(\vec{\mathbf{r}}) = \overleftrightarrow{\mathbf{C}}_M \bullet \vec{\mathbf{J}}(\vec{\mathbf{r}}_M) \tag{4.37}$$

$$\rho_m(\vec{\mathbf{r}}) = \rho(\vec{\mathbf{r}}_M) \tag{4.38}$$

It is interesting to compare (4.36) to its reflection field equivalent in (4.20). The rotation of the magnetic field vector by a group symmetry rotation operation does not change the sign of the magnetic field as it does for the group reflection operation [13]. This is expected since a simple rotational translation will not reverse the solenoid properties of the magnetic fields: a right-handed screw rotated to a different location is still a right-handed screw. In general, a sign change occurs when the magnetic field is subjected to improper rotations such as reflection and no sign change occurs when the magnetic field is subjected to proper rotations, such as rotation.

These new field quantities must satisfy Maxwell's equations as valid representations of electromagnetic phenomena rotated through a group symmetry operation. As before, the curl operations are satisfied by

$$\begin{aligned}
\nabla \times \vec{\mathbf{E}}_M(\vec{\mathbf{r}}) &= \begin{vmatrix} \hat{\mathbf{e}}_x & \hat{\mathbf{e}}_y & \hat{\mathbf{e}}_z \\ \partial/\partial x & \partial/\partial y & \partial/\partial z \\ (E_M(\vec{\mathbf{r}}))_x & (E_M(\vec{\mathbf{r}}))_y & (E_M(\vec{\mathbf{r}}))_z \end{vmatrix} \\
&= \overleftrightarrow{\mathbf{C}}_M \bullet \begin{vmatrix} \hat{\mathbf{e}}_x & \hat{\mathbf{e}}_y & \hat{\mathbf{e}}_z \\ \partial/\partial x_m & \partial/\partial y_m & \partial/\partial z_m \\ (E(\vec{\mathbf{r}}_M))_x & (E(\vec{\mathbf{r}}_M))_y & (E(\vec{\mathbf{r}}_M))_z \end{vmatrix} \\
&= -j\omega\mu \overleftrightarrow{\mathbf{C}}_M \bullet \vec{\mathbf{H}}(\vec{\mathbf{r}}_M) \\
&= -j\omega\mu \vec{\mathbf{H}}_M(\vec{\mathbf{r}})
\end{aligned} \tag{4.39}$$

and similarly,

$$\nabla \times \vec{\mathbf{H}}_M(\vec{\mathbf{r}}) = \begin{vmatrix} \hat{\mathbf{e}}_x & \hat{\mathbf{e}}_y & \hat{\mathbf{e}}_z \\ \partial/\partial x & \partial/\partial y & \partial/\partial z \\ (H_M(\vec{\mathbf{r}}))_x & (H_M(\vec{\mathbf{r}}))_y & (H_M(\vec{\mathbf{r}}))_z \end{vmatrix}$$

$$
\begin{aligned}
&= \vec{\mathbf{C}}_M \bullet \begin{vmatrix} \hat{\mathbf{e}}_x & \hat{\mathbf{e}}_y & \hat{\mathbf{e}}_z \\ \partial/\partial x_m & \partial/\partial y_m & \partial/\partial z_m \\ \left(H(\vec{\mathbf{r}}_M)\right)_x & \left(H(\vec{\mathbf{r}}_M)\right)_y & \left(H(\vec{\mathbf{r}}_M)\right)_z \end{vmatrix} \\
&= \vec{\mathbf{C}}_M \bullet \vec{\mathbf{J}}(\vec{\mathbf{r}}_M) + (\sigma + j\omega)\vec{\mathbf{C}}_M \bullet \vec{\mathbf{E}}(\vec{\mathbf{r}}_M) \\
&= \vec{\mathbf{J}}_M(\vec{\mathbf{r}}) + (\sigma + j\omega)\vec{\mathbf{E}}_M(\vec{\mathbf{r}})
\end{aligned} \tag{4.40}
$$

The continuity equation of (2.27) is satisfied identically as it is satisfied in (4.25):

$$
\begin{aligned}
-j\omega\rho_M(\vec{\mathbf{r}}) &= \nabla \bullet \vec{\mathbf{J}}_M(\vec{\mathbf{r}}) \\
&= \frac{\partial}{\partial x}\vec{\mathbf{J}}_M(\vec{\mathbf{r}}) + \frac{\partial}{\partial y}\vec{\mathbf{J}}_M(\vec{\mathbf{r}}) + \frac{\partial}{\partial z}\vec{\mathbf{J}}_M(\vec{\mathbf{r}}) \\
&= \frac{\partial}{\partial x_M}\vec{\mathbf{J}}(\vec{\mathbf{r}}_M) + \frac{\partial}{\partial y_M}\vec{\mathbf{J}}(\vec{\mathbf{r}}_M) + \frac{\partial}{\partial z_M}\vec{\mathbf{J}}(\vec{\mathbf{r}}_M) \\
&= -j\omega\rho(\vec{\mathbf{r}}_M)
\end{aligned} \tag{4.41}
$$

In a manner similar to the derivations for reflection symmetry, these equations suggest that if C_M symmetry exists then a measurement at one location will reveal information concerning the target at M locations in total.

In an analogous approach to reflection symmetry operations, symmetrical and antisymmetrical components of the measured fields can be constructed by measurements that are subjected to the rotation operation C_M. Figure 4.6 illustrates a target with C_3 symmetry (and no $\mathcal{R}$ symmetry). The responses are taken at $\vec{\mathbf{r}}$, $\vec{\mathbf{r}}_3^{(1)} = \vec{\mathbf{C}}_3 \bullet \vec{\mathbf{r}}$ and $\vec{\mathbf{r}}_3^{(2)} = \left(\vec{\mathbf{C}}_3\right)^2 \bullet \vec{\mathbf{r}}$ from the excitation fields that are also rotated with the symmetry rotation operation.

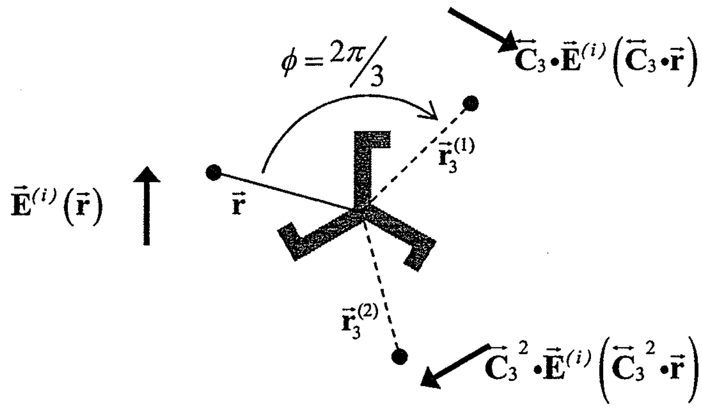

Figure 4.6 An object with C_3 symmetry observed through symmetry operations

The symmetric and antisymmetric fields will then take on an identical form as in (4.26) through (4.29). These are

$$\vec{\mathbf{E}}_{sy}(\vec{\mathbf{r}}) = \frac{1}{2}\left\{\vec{\mathbf{E}}(\vec{\mathbf{r}}) + \vec{\mathbf{E}}_M(\vec{\mathbf{r}})\right\} = \frac{1}{2}\left\{\vec{\mathbf{E}}(\vec{\mathbf{r}}) + \vec{\mathbf{C}}_M \bullet \vec{\mathbf{E}}(\vec{\mathbf{r}}_M)\right\}, \tag{4.42}$$

$$\vec{\mathbf{H}}_{sy}(\vec{\mathbf{r}}) = \frac{1}{2}\left\{\vec{\mathbf{H}}(\vec{\mathbf{r}}) + \vec{\mathbf{H}}_M(\vec{\mathbf{r}})\right\} = \frac{1}{2}\left\{\vec{\mathbf{H}}(\vec{\mathbf{r}}) + \vec{\mathbf{C}}_M \bullet \vec{\mathbf{H}}(\vec{\mathbf{r}}_M)\right\}, \tag{4.43}$$

$$\vec{\mathbf{E}}_{as}(\vec{\mathbf{r}}) = \frac{1}{2}\left\{\vec{\mathbf{E}}(\vec{\mathbf{r}}) - \vec{\mathbf{E}}_M(\vec{\mathbf{r}})\right\} = \frac{1}{2}\left\{\vec{\mathbf{E}}(\vec{\mathbf{r}}) - \vec{\mathbf{C}}_M \bullet \vec{\mathbf{E}}(\vec{\mathbf{r}}_M)\right\}, \tag{4.44}$$

$$\vec{\mathbf{H}}_{as}(\vec{\mathbf{r}}) = \frac{1}{2}\left\{\vec{\mathbf{H}}(\vec{\mathbf{r}}) - \vec{\mathbf{H}}_M(\vec{\mathbf{r}})\right\} = \frac{1}{2}\left\{\vec{\mathbf{H}}(\vec{\mathbf{r}}) - \vec{\mathbf{C}}_M \bullet \vec{\mathbf{H}}(\vec{\mathbf{r}}_M)\right\}. \tag{4.45}$$

As before, the fields can be reconstructed from their symmetric and antisymmetric components by:

$$\vec{\mathbf{E}}(\vec{\mathbf{r}}) = \vec{\mathbf{E}}_{sy}(\vec{\mathbf{r}}) + \vec{\mathbf{E}}_{as}(\vec{\mathbf{r}}), \tag{4.46}$$

$$\vec{\mathbf{H}}(\vec{\mathbf{r}}) = \vec{\mathbf{H}}_{sy}(\vec{\mathbf{r}}) + \vec{\mathbf{H}}_{as}(\vec{\mathbf{r}}). \tag{4.47}$$

These equations show that if measurements are taken at a location $\vec{\mathbf{r}}$ and at a C_M rotated position $\vec{\mathbf{r}}_M$, the measured electric and magnetic fields may be decomposed into symmetric and antisymmetric components. Furthermore the equations suggest that if the object does in fact possess C_M symmetry (or if the group C_M is a subgroup of the actual target symmetry) then measurements at $\vec{\mathbf{r}}$ and $\vec{\mathbf{r}}_M$ that are excited by $\vec{\mathbf{E}}^{(i)}(\vec{\mathbf{r}})$ and $\vec{\mathbf{C}}_M \bullet \vec{\mathbf{E}}_M^{(i)}(\vec{\mathbf{C}}_M \bullet \vec{\mathbf{r}})$ respectively will give

$$\begin{aligned}\vec{\mathbf{E}}(\vec{\mathbf{r}}) &= \vec{\mathbf{E}}_M(\vec{\mathbf{r}}) = \vec{\mathbf{C}}_M \bullet \vec{\mathbf{E}}(\vec{\mathbf{C}}_M \bullet \vec{\mathbf{r}}) \\ \vec{\mathbf{H}}(\vec{\mathbf{r}}) &= \vec{\mathbf{H}}_M(\vec{\mathbf{r}}) = \vec{\mathbf{C}}_M \bullet \vec{\mathbf{H}}(\vec{\mathbf{C}}_M \bullet \vec{\mathbf{r}})\end{aligned} \tag{4.48}$$

so that

$$\begin{aligned}\vec{\mathbf{E}}_{sy}(\vec{\mathbf{r}}) &= \vec{\mathbf{E}}(\vec{\mathbf{r}}) \\ \vec{\mathbf{H}}_{sy}(\vec{\mathbf{r}}) &= \vec{\mathbf{H}}(\vec{\mathbf{r}})\end{aligned} \tag{4.49}$$

and

$$\vec{\mathbf{E}}_{as}(\vec{\mathbf{r}}) = \vec{\mathbf{H}}_{as}(\vec{\mathbf{r}}) = 0 \tag{4.50}$$

which is the same result for reflection symmetry given in section 4.2. As before, target asymmetry does not imply target antisymmetry and an asymmetric target with respect to the rotation operation can not be expected to yield zero valued symmetric fields. Rather the general case of scattering from an arbitrary target will exhibit both symmetric and antisymmetric components in the symmetry decomposition. These results can be further generalized to include the augmented rotation-reflection group C_{Ma} by means of (4.11). Because of (4.11) the results outlined in the symmetry conditions for $\mathcal{R}$ group operations in (4.32)-(4.34) and in the C_M conditions of (4.48)-(4.50) will hold for any target with C_{Ma} symmetry such that

$$\vec{\mathbf{E}}(\vec{\mathbf{r}}) = \vec{\mathbf{E}}_m(\vec{\mathbf{r}}) = \overleftrightarrow{\mathbf{R}}' \bullet \vec{\mathbf{E}}\left(\overleftrightarrow{\mathbf{R}}' \bullet \vec{\mathbf{r}}\right)$$
$$\vec{\mathbf{H}}(\vec{\mathbf{r}}) = \vec{\mathbf{H}}_m(\vec{\mathbf{r}}) = -\overleftrightarrow{\mathbf{R}}' \bullet \vec{\mathbf{H}}\left(\overleftrightarrow{\mathbf{R}}' \bullet \vec{\mathbf{r}}\right) \tag{4.51}$$

where

$$\overleftrightarrow{\mathbf{R}}' = \left(\overleftrightarrow{\mathbf{C}}_M \bullet \overleftrightarrow{\mathbf{R}} \bullet \overleftrightarrow{\mathbf{C}}_M^{-1}\right) \tag{4.52}$$

is a similarity transformation of the original reflection group $\mathcal{R}$ representation by means of the relevant rotation group C_M. For general C_{Ma} symmetry, the symmetric and antisymmetric fields can be constructed by incorporating (4.52) into the symmetric and antisymmetric field equations for the case of general improper symmetry operations

$$\vec{\mathbf{E}}_{sy}(\vec{\mathbf{r}}) = \frac{1}{2}\left\{\vec{\mathbf{E}}(\vec{\mathbf{r}}) + \vec{\mathbf{E}}_{Mm}(\vec{\mathbf{r}})\right\} = \frac{1}{2}\left\{\vec{\mathbf{E}}(\vec{\mathbf{r}}) + \overleftrightarrow{\mathbf{C}}_{Ma} \bullet \vec{\mathbf{E}}\left(\overleftrightarrow{\mathbf{C}}_{Ma} \bullet \vec{\mathbf{r}}\right)\right\}, \tag{4.53}$$

$$\vec{\mathbf{H}}_{sy}(\vec{\mathbf{r}}) = \frac{1}{2}\left\{\vec{\mathbf{H}}(\vec{\mathbf{r}}) + \vec{\mathbf{H}}_{Mm}(\vec{\mathbf{r}})\right\} = \frac{1}{2}\left\{\vec{\mathbf{H}}(\vec{\mathbf{r}}) \pm \overleftrightarrow{\mathbf{C}}_{Ma} \bullet \vec{\mathbf{H}}\left(\overleftrightarrow{\mathbf{C}}_{Ma} \bullet \vec{\mathbf{r}}\right)\right\}, \tag{4.54}$$

$$\vec{\mathbf{E}}_{as}(\vec{\mathbf{r}}) = \frac{1}{2}\left\{\vec{\mathbf{E}}(\vec{\mathbf{r}}) - \vec{\mathbf{E}}(\vec{\mathbf{r}})\right\} = \frac{1}{2}\left\{\vec{\mathbf{E}}(\vec{\mathbf{r}}) - \overleftrightarrow{\mathbf{C}}_{Ma} \bullet \vec{\mathbf{E}}\left(\overleftrightarrow{\mathbf{C}}_{Ma} \bullet \vec{\mathbf{r}}\right)\right\}, \tag{4.55}$$

$$\vec{\mathbf{H}}_{as}(\vec{\mathbf{r}}) = \frac{1}{2}\left\{\vec{\mathbf{H}}(\vec{\mathbf{r}}) - \vec{\mathbf{H}}_{Mm}(\vec{\mathbf{r}})\right\} = \frac{1}{2}\left\{\vec{\mathbf{H}}(\vec{\mathbf{r}}) \pm \overleftrightarrow{\mathbf{C}}_{Ma} \bullet \vec{\mathbf{H}}\left(\overleftrightarrow{\mathbf{C}}_{Ma} \bullet \vec{\mathbf{r}}\right)\right\}, \tag{4.56}$$

where the sign changes in (4.54) and (4.56) depend on whether or not the operation is a proper or improper rotation. The usual conditions and expectations apply.

The consequences of group symmetries in observed targets are summarized in Table 4.1 below.

Table 4.1

Group	*Constitutive Parameters*	*Symmetry Conditions*
$\mathcal{R}$	$\sigma(\vec{\mathbf{r}})=\sigma(\vec{\mathbf{r}}_m)$ $\varepsilon(\vec{\mathbf{r}})=\varepsilon(\vec{\mathbf{r}}_m)$ $\mu(\vec{\mathbf{r}})=\mu(\vec{\mathbf{r}}_m)$	$\vec{\mathbf{E}}(\vec{\mathbf{r}})=\overleftrightarrow{\mathbf{R}}\bullet\vec{\mathbf{E}}(\vec{\mathbf{r}}_m)$ $\vec{\mathbf{H}}(\vec{\mathbf{r}})=-\overleftrightarrow{\mathbf{R}}\bullet\vec{\mathbf{H}}(\vec{\mathbf{r}}_m)$
C_M	$\sigma(\vec{\mathbf{r}})=\sigma(\vec{\mathbf{r}}_M)$ $\varepsilon(\vec{\mathbf{r}})=\varepsilon(\vec{\mathbf{r}}_M)$ $\mu(\vec{\mathbf{r}})=\mu(\vec{\mathbf{r}}_M)$	$\vec{\mathbf{E}}(\vec{\mathbf{r}})=\overleftrightarrow{\mathbf{C}}_M\bullet\vec{\mathbf{E}}_M(\vec{\mathbf{r}}_M)$ $\vec{\mathbf{H}}(\vec{\mathbf{r}})=\overleftrightarrow{\mathbf{C}}_M\bullet\vec{\mathbf{H}}_M(\vec{\mathbf{r}}_M)$
C_{Ma}	$\sigma(\vec{\mathbf{r}})=\sigma(\vec{\mathbf{r}}_M)=\sigma(\vec{\mathbf{r}}_m)=\sigma(\vec{\mathbf{r}}_{Mm})$ $\varepsilon(\vec{\mathbf{r}})=\varepsilon(\vec{\mathbf{r}}_M)=\varepsilon(\vec{\mathbf{r}}_m)=\varepsilon(\vec{\mathbf{r}}_{Mm})$ $\mu(\vec{\mathbf{r}})=\mu(\vec{\mathbf{r}}_M)=\mu(\vec{\mathbf{r}}_m)=\mu(\vec{\mathbf{r}}_{Mm})$	$\vec{\mathbf{E}}(\vec{\mathbf{r}})=\overleftrightarrow{\mathbf{R}}\bullet\vec{\mathbf{E}}(\vec{\mathbf{r}}_m)=\overleftrightarrow{\mathbf{C}}_M\bullet\vec{\mathbf{E}}(\vec{\mathbf{r}}_M)$ $=\overleftrightarrow{\mathbf{C}}_{Ma}\bullet\vec{\mathbf{E}}\left(\overleftrightarrow{\mathbf{C}}_{Ma}\bullet\vec{\mathbf{r}}\right)$ $\vec{\mathbf{H}}(\vec{\mathbf{r}})=-\overleftrightarrow{\mathbf{R}}\bullet\vec{\mathbf{H}}(\vec{\mathbf{r}}_m)=\overleftrightarrow{\mathbf{C}}_M\bullet\vec{\mathbf{H}}(\vec{\mathbf{r}}_M)$ $=\pm\overleftrightarrow{\mathbf{C}}_{Ma}\vec{\mathbf{H}}\left(\overleftrightarrow{\mathbf{C}}_{Ma}\bullet\vec{\mathbf{r}}\right)$

4.4 Bistatic Scattering of Subsurface Symmetric Targets and Generalized Reciprocity

Consider a bistatic GPR system defined in the upper-half space by the dyadic Green's function $\overline{\overline{\mathbf{G}}}_s(\vec{\mathbf{r}}_1,\vec{\mathbf{r}}_2)$. If a subsurface target with a group symmetry of order N and group representation $\overleftrightarrow{\Phi}_\ell$ is present, the symmetry will manifest itself in $\overline{\overline{\mathbf{G}}}_s$ such that the symmetry can be analysed by successive measurements, regardless of the bistatic antenna configuration. The ground is assumed to be planar with symmetry of $\mathcal{T}_2\otimes C_{\infty a}$, meaning that it is the direct product of $\mathcal{T}_2$ translational symmetry in two dimensions and continuous rotational symmetry [38]. $\mathcal{T}_2$ symmetry is equivalent to invariance through two dimensional translations in space. Disregarding any present subsurface scattering, any translation in the plane above ground will leave the result unchanged as long as all translations occur parallel to the ground plane (otherwise the $\mathcal{T}_2$ symmetry is destroyed and the results will vary). This result is intuitive since moving the GPR along an infinite planar structure should not result in any electromagnetic fluctuations. Since by hypothesis the subsurface target has finite dimensions, only point symmetry groups will apply to targets and $\mathcal{T}_2$ symmetry will not apply. By hypothesis, target symmetry will be a subset of $C_{\infty a}$ symmetry. This is to say, we will restrict our attention to targets that possess some form of rotation, reflection or both symmetries. However $C_{\infty a}$ is of course a subgroup of the ground symmetry $\mathcal{T}_2 \otimes C_{\infty a}$, meaning that any target of interest will then be a subset of the ground symmetry group when the target axis of symmetry is perpendicular to the ground plane. Any target symmetry group which is a subgroup of the earth/target symmetry group is retained as a symmetry group of the earth/target combination [38]. This means that the presence of the ground plane will not destroy the symmetry of the targets we seek and that the ground itself will manifest itself as a symmetric target.

The GPR system comprises two antennas that are initially positioned at $\vec{\mathbf{r}}_1$ and $\vec{\mathbf{r}}_2$ respectively as depicted in Figure 4.7. The two antennas are represented as current sources $\vec{\mathbf{J}}_1$ and $\vec{\mathbf{J}}_2$ and are initially oriented arbitrarily. Because of reciprocity, either antenna can be transmitter or receiver, however, we will take $\vec{\mathbf{J}}_1$ as the transmitter and $\vec{\mathbf{J}}_2$ as the receiver. The scattered electric fields at the receiver due to the current source at the transmitter are given by (2.47) which is

$$\vec{\mathbf{E}}_2^{(s)}(\vec{\mathbf{r}}_2) = -j\omega\mu \iiint_{V_1} \overline{\overline{\mathbf{G}}}_s(\vec{\mathbf{r}}_1, \vec{\mathbf{r}}_2) \cdot \vec{\mathbf{J}}_1(\vec{\mathbf{r}}_1)\, dv_1 . \tag{4.57}$$

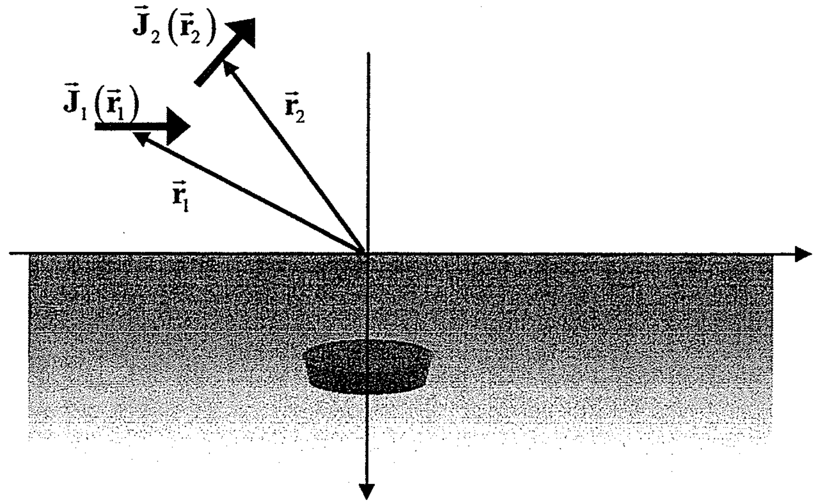

Figure 4.7 A symmetrical object measured by a bistatic system

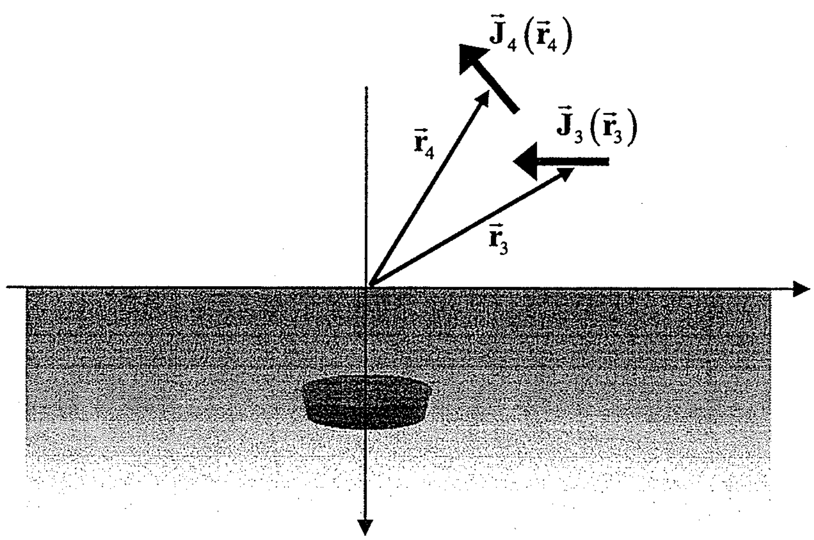

Figure 4.8 Symmetric object measured with a bistatic system through a symmetry operation

Application of a target symmetry operation to the bistatic configuration will alter the geometry of the problem as shown in Figure 4.8. The new bistatic orientation in the transformed system is given by

$$\vec{\mathbf{J}}_3(\vec{\mathbf{r}}_3) = \overleftrightarrow{\mathbf{\Phi}} \bullet \vec{\mathbf{J}}_1(\vec{\mathbf{r}}_1)$$
$$\vec{\mathbf{J}}_4(\vec{\mathbf{r}}_4) = \overleftrightarrow{\mathbf{\Phi}} \bullet \vec{\mathbf{J}}_2(\vec{\mathbf{r}}_2), \tag{4.58}$$

where

$$\begin{aligned} \vec{\mathbf{r}}_3 &= \overleftrightarrow{\mathbf{\Phi}} \bullet \vec{\mathbf{r}}_1 \longrightarrow \vec{\mathbf{r}}_1 = \overleftrightarrow{\mathbf{\Phi}}^{-1} \bullet \vec{\mathbf{r}}_3 \\ \vec{\mathbf{r}}_4 &= \overleftrightarrow{\mathbf{\Phi}} \bullet \vec{\mathbf{r}}_2 \longrightarrow \vec{\mathbf{r}}_2 = \overleftrightarrow{\mathbf{\Phi}}^{-1} \bullet \vec{\mathbf{r}}_4 \end{aligned}. \tag{4.59}$$

The transmitter is now located at $\vec{\mathbf{r}}_3$ and oriented as $\vec{\mathbf{J}}_3$ while the receiver is now located at $\vec{\mathbf{r}}_4$ and is oriented as $\vec{\mathbf{J}}_4$. Under this configuration, the scattered electric field at the receiver will be

$$\vec{\mathbf{E}}_4^{(s)}(\vec{\mathbf{r}}_4) = -j\omega\mu \iiint_{V_3} \overline{\overline{\mathbf{G}}}_s(\vec{\mathbf{r}}_3, \vec{\mathbf{r}}_4) \bullet \vec{\mathbf{J}}_3(\vec{\mathbf{r}}_3)\, dv_3 . \tag{4.60}$$

Because this new measurement corresponds to a symmetry operation, the two measurements will be equal so that

$$\vec{\mathbf{E}}_4^{(s)}(\vec{\mathbf{r}}_4) = \overleftrightarrow{\mathbf{\Phi}} \bullet \vec{\mathbf{E}}_2^{(s)}(\vec{\mathbf{r}}_2). \tag{4.61}$$

This implies

$$\begin{aligned} \overleftrightarrow{\mathbf{\Phi}} \bullet \vec{\mathbf{E}}_2^{(s)}(\vec{\mathbf{r}}_2) &= -j\omega\mu \iiint_{V_1} \overleftrightarrow{\mathbf{\Phi}} \bullet \overline{\overline{\mathbf{G}}}_s(\vec{\mathbf{r}}_1, \vec{\mathbf{r}}_2) \bullet \vec{\mathbf{J}}_1(\vec{\mathbf{r}}_1)\, dv_1 \\ &= -j\omega\mu \iiint_{V_1} \left(\overleftrightarrow{\mathbf{\Phi}} \bullet \overline{\overline{\mathbf{G}}}_s(\vec{\mathbf{r}}_1, \vec{\mathbf{r}}_2) \bullet \overleftrightarrow{\mathbf{\Phi}}^{-1} \right) \bullet \overleftrightarrow{\mathbf{\Phi}} \bullet \vec{\mathbf{J}}_1(\vec{\mathbf{r}}_1)\, dv_1 \\ &= -j\omega\mu \iiint_{V_3} \left(\overleftrightarrow{\mathbf{\Phi}} \bullet \overline{\overline{\mathbf{G}}}_s\left(\overleftrightarrow{\mathbf{\Phi}}^{-1} \bullet \vec{\mathbf{r}}_3, \overleftrightarrow{\mathbf{\Phi}}^{-1} \bullet \vec{\mathbf{r}}_4 \right) \bullet \overleftrightarrow{\mathbf{\Phi}}^{-1} \right) \bullet \vec{\mathbf{J}}_3(\vec{\mathbf{r}}_3)\, dv_3 \\ &= \vec{\mathbf{E}}_4^{(s)}(\vec{\mathbf{r}}_4) \end{aligned}, \tag{4.62}$$

Notice that the Jacobian of the transformation is neglected because the orthogonality of the transformation implies a Jacobian determinant of unity. Equation (4.62) therefore implies that

$$\begin{aligned}\overline{\overline{\mathbf{G}}}_s(\vec{\mathbf{r}}_3,\vec{\mathbf{r}}_4) &= \overleftrightarrow{\mathbf{\Phi}}\bullet\overline{\overline{\mathbf{G}}}_s\left(\overleftrightarrow{\mathbf{\Phi}}^{-1}\bullet\vec{\mathbf{r}}_3,\overleftrightarrow{\mathbf{\Phi}}^{-1}\bullet\vec{\mathbf{r}}_4\right)\bullet\overleftrightarrow{\mathbf{\Phi}}^{-1} \\ &= \overleftrightarrow{\mathbf{\Phi}}\bullet\overline{\overline{\mathbf{G}}}_s(\vec{\mathbf{r}}_1,\vec{\mathbf{r}}_2)\bullet\overleftrightarrow{\mathbf{\Phi}}^{-1}\end{aligned} \qquad (4.63)$$

This result implies that given a measurement as in (4.57) for a target with a symmetry of order N with matrix representation $\overleftrightarrow{\mathbf{\Phi}}_\ell$ ($\ell = 1,2,\ldots,N$), N-1 other solutions can be determined from (4.63). If we know the electric field response $\vec{\mathbf{E}}_1$ at $\vec{\mathbf{r}}_1$ then we can deduce the responses $\vec{\mathbf{E}}_\ell^{(s)}(\vec{\mathbf{r}}_\ell) = \overleftrightarrow{\mathbf{\Phi}}_\ell\bullet\vec{\mathbf{E}}_1^{(s)}(\vec{\mathbf{r}}_1)$, $(\ell = 2,3\ldots,N)$. Equation (4.63) represents the formal justification for the translation of symmetry from symmetric electromagnetic boundary conditions to symmetric electromagnetic fields.

In (2.52), reciprocity was used to show that any dyadic Green's function is symmetric so that knowledge of only six of the nine dyadic components are necessary to complete the dyadic. Equation (4.63) may be used in a similar fashion when N fold symmetry is present in the dyadic.

For instance, consider once again a target with C_{4a} symmetry with respect to the z axis as shown in Figure 3.3. The degenerate vectors for this particular symmetry operation were given in (3.39) and were found to be arbitrary positions on the symmetry plane in question. In the context of (4.63) the symmetry operation provides the transformations $\vec{\mathbf{r}}_3 = \overleftrightarrow{\mathbf{R}}\bullet\vec{\mathbf{r}}_1$ and $\vec{\mathbf{r}}_4 = \overleftrightarrow{\mathbf{R}}\bullet\vec{\mathbf{r}}_2$. The dyadic Green's function $\overline{\overline{\mathbf{G}}}(\vec{\mathbf{r}}_3,\vec{\mathbf{r}}_4)$ in matrix form can be written as

$$\overline{\overline{\mathbf{G}}}(\vec{\mathbf{r}}_3,\vec{\mathbf{r}}_4)=\begin{bmatrix} g_{xx}(\vec{\mathbf{r}}_3,\vec{\mathbf{r}}_4) & g_{xy}(\vec{\mathbf{r}}_3,\vec{\mathbf{r}}_4) & g_{xz}(\vec{\mathbf{r}}_3,\vec{\mathbf{r}}_4) \\ g_{yx}(\vec{\mathbf{r}}_3,\vec{\mathbf{r}}_4) & g_{yy}(\vec{\mathbf{r}}_3,\vec{\mathbf{r}}_4) & g_{yz}(\vec{\mathbf{r}}_3,\vec{\mathbf{r}}_4) \\ g_{zx}(\vec{\mathbf{r}}_3,\vec{\mathbf{r}}_4) & g_{zy}(\vec{\mathbf{r}}_3,\vec{\mathbf{r}}_4) & g_{zz}(\vec{\mathbf{r}}_3,\vec{\mathbf{r}}_4) \end{bmatrix}. \tag{4.64}$$

Implementing (4.63) gives

$$\begin{aligned} \overline{\overline{\mathbf{G}}}(\vec{\mathbf{r}}_3,\vec{\mathbf{r}}_4) &= \overleftrightarrow{\mathbf{R}}\bullet\overline{\overline{\mathbf{G}}}\left(\overleftrightarrow{\mathbf{R}}^{-1}\bullet\vec{\mathbf{r}}_3,\overleftrightarrow{\mathbf{R}}^{-1}\bullet\vec{\mathbf{r}}_4\right)\bullet\overleftrightarrow{\mathbf{R}}^{-1} \\ &= \overleftrightarrow{\mathbf{R}}\bullet\overline{\overline{\mathbf{G}}}(\vec{\mathbf{r}}_1,\vec{\mathbf{r}}_2)\bullet\overleftrightarrow{\mathbf{R}}^{-1} \\ &= \begin{bmatrix} g_{xx}(\vec{\mathbf{r}}_1,\vec{\mathbf{r}}_2) & -g_{xy}(\vec{\mathbf{r}}_1,\vec{\mathbf{r}}_2) & g_{xz}(\vec{\mathbf{r}}_1,\vec{\mathbf{r}}_2) \\ -g_{yx}(\vec{\mathbf{r}}_1,\vec{\mathbf{r}}_2) & g_{yy}(\vec{\mathbf{r}}_1,\vec{\mathbf{r}}_2) & -g_{yz}(\vec{\mathbf{r}}_1,\vec{\mathbf{r}}_2) \\ g_{zx}(\vec{\mathbf{r}}_1,\vec{\mathbf{r}}_2) & -g_{zy}(\vec{\mathbf{r}}_1,\vec{\mathbf{r}}_2) & g_{zz}(\vec{\mathbf{r}}_1,\vec{\mathbf{r}}_2) \end{bmatrix} \end{aligned}. \tag{4.65}$$

This equation indicates some interesting properties. For example, by inspection it can be seen that $g_{xy}(\vec{\mathbf{r}}_3,\vec{\mathbf{r}}_4)=-g_{xy}(\vec{\mathbf{r}}_1,\vec{\mathbf{r}}_2)$, $g_{zy}(\vec{\mathbf{r}}_3,\vec{\mathbf{r}}_4)=-g_{zy}(\vec{\mathbf{r}}_1,\vec{\mathbf{r}}_2)$ etc. These relationships are similar to the conventional reciprocity relationship (2.52) where it was found that the off diagonal elements of the dyadic are equal (e.g. $g_{xy}(\vec{\mathbf{r}}_1,\vec{\mathbf{r}}_2)=g_{yx}(\vec{\mathbf{r}}_2,\vec{\mathbf{r}}_1)$). Therefore (4.63) can be thought of as a more general form of electromagnetic reciprocity that is exhibited only by symmetric targets; from knowledge of target symmetry, some very intricate assumptions may be made about the form of the Green's function and therefore of the scattering behaviour.

A more profound result can be ascertained if the concept of degeneracy is now introduced into the discussion. Equation (3.33) shows that for degenerate configurations, a position vector can be left unchanged by a symmetry operation. For the $\overleftrightarrow{\mathbf{R}}$ operation, with the symmetry plane coinciding with the *x-z* plane, it has been established that the degenerate unit vectors are $(\hat{\mathbf{r}}_{dn})_1=\hat{\mathbf{e}}_x$ and $(\hat{\mathbf{r}}_{dn})_2=\hat{\mathbf{e}}_z$, corresponding to arbitrary positions on the symmetry plane itself. Setting $\vec{\mathbf{r}}_1 = a(\hat{\mathbf{r}}_{dn})_1 + b(\hat{\mathbf{r}}_{dn})_2$ and $\vec{\mathbf{r}}_2 = c(\hat{\mathbf{r}}_{dn})_1 + d(\hat{\mathbf{r}}_{dn})_2$, and invoking the fact that $\overleftrightarrow{\mathbf{R}} = \overleftrightarrow{\mathbf{R}}^{-1}$, (4.63) becomes

$$\begin{aligned}\overline{\overline{\mathbf{G}}}_s(\vec{\mathbf{r}}_1,\vec{\mathbf{r}}_2) &= \overleftrightarrow{\mathbf{R}}\bullet\overline{\overline{\mathbf{G}}}_s\left(\overleftrightarrow{\mathbf{R}}\bullet\vec{\mathbf{r}}_1,\overleftrightarrow{\mathbf{R}}\bullet\vec{\mathbf{r}}_2\right)\bullet\overleftrightarrow{\mathbf{R}}^{-1} \\ &= \overleftrightarrow{\mathbf{R}}\bullet\overline{\overline{\mathbf{G}}}_s(\vec{\mathbf{r}}_1,\vec{\mathbf{r}}_2)\bullet\overleftrightarrow{\mathbf{R}}^{-1}\end{aligned} \quad . \tag{4.66}$$

From this result, the following equalities obtain:

$$g_{xy}(\vec{\mathbf{r}}_1,\vec{\mathbf{r}}_2) = -g_{xy}(\vec{\mathbf{r}}_1,\vec{\mathbf{r}}_2) = 0\,, \tag{4.67}$$

$$g_{yx}(\vec{\mathbf{r}}_1,\vec{\mathbf{r}}_2) = -g_{yx}(\vec{\mathbf{r}}_1,\vec{\mathbf{r}}_2) = 0\,, \tag{4.68}$$

$$g_{yz}(\vec{\mathbf{r}}_1,\vec{\mathbf{r}}_2) = -g_{yz}(\vec{\mathbf{r}}_1,\vec{\mathbf{r}}_2) = 0\,, \tag{4.69}$$

$$g_{zy}(\vec{\mathbf{r}}_1,\vec{\mathbf{r}}_2) = -g_{zy}(\vec{\mathbf{r}}_1,\vec{\mathbf{r}}_2) = 0\,. \tag{4.70}$$

The result is a simplified dyadic Green's function that applies to the specific degenerate vector

$$\overline{\overline{\mathbf{G}}}(\vec{\mathbf{r}}_1,\vec{\mathbf{r}}_2) = \begin{bmatrix} g_{xx}(\vec{\mathbf{r}}_1,\vec{\mathbf{r}}_2) & 0 & g_{xz}(\vec{\mathbf{r}}_1,\vec{\mathbf{r}}_2) \\ 0 & g_{yy}(\vec{\mathbf{r}}_1,\vec{\mathbf{r}}_2) & 0 \\ g_{zx}(\vec{\mathbf{r}}_1,\vec{\mathbf{r}}_2) & 0 & g_{zz}(\vec{\mathbf{r}}_1,\vec{\mathbf{r}}_2) \end{bmatrix}. \tag{4.71}$$

It should be noted that the selection of $\vec{\mathbf{r}}_1$ and $\vec{\mathbf{r}}_2$ is arbitrary and that the formulation holds if they are interchanged or selected to be the same degenerate vector. These results, along with conventional reciprocity, imply that, when an object with C_{4a} symmetry is observed with a bistatic system, where the source and receiver are located on the same symmetry plane, the dyadic Green's function will possess only two off diagonal elements

$g_{zx}(\vec{\mathbf{r}}_1,\vec{\mathbf{r}}_2) = g_{xz}(\vec{\mathbf{r}}_1,\vec{\mathbf{r}}_2)$. This result is not obvious and is difficult to visualize in the absence of a group theoretical argument.

4.5 Equivalence of Symmetry in the Frequency and Time Domains

The electromagnetic symmetry formulations in the preceding arguments, and indeed in this entire chapter so far, have all been undertaken in the frequency domain because the radar system of interest is stepped frequency radar. The formulation in the frequency domain does not imply that the symmetries are exclusively frequency domain phenomena. In fact, symmetry in the frequency domain is equivalent to symmetry in the time domain and therefore equivalent to symmetry in the range domain via the range scaling equation of (2.61).

Again consider the scenarios presented in Figure 4.7 and Figure 4.8. It has been shown in the previous section that the corresponding field quantities are related by (4.61). This equivalence can be established in the time domain through implementation of the inverse Fourier transform which gives:

$$\vec{\mathbf{E}}_2(\vec{\mathbf{r}}_2,t) = \int_{-\infty}^{\infty} \vec{\mathbf{E}}_2(\vec{\mathbf{r}}_2,f)e^{j2\pi ft}df \tag{4.72}$$

$$\vec{\mathbf{E}}_4(\vec{\mathbf{r}}_4,t) = \int_{-\infty}^{\infty} \vec{\mathbf{E}}_4(\vec{\mathbf{r}}_4,f)e^{j2\pi ft}df \tag{4.73}$$

Invoking the relationship denoted in (4.61), one obtains

$$\begin{aligned}\vec{\mathbf{E}}_4(\vec{\mathbf{r}}_4,t) &= \int_{-\infty}^{\infty} \vec{\mathbf{E}}_4(\vec{\mathbf{r}}_4,f)e^{j2\pi ft}df \\ &= \int_{-\infty}^{\infty} \overleftrightarrow{\mathbf{\Phi}}\bullet\vec{\mathbf{E}}_2(\vec{\mathbf{r}}_2,f)e^{j2\pi ft}df \\ &= \overleftrightarrow{\mathbf{\Phi}}\bullet\int_{-\infty}^{\infty} \vec{\mathbf{E}}_2(\vec{\mathbf{r}}_2,f)e^{j2\pi ft}df\end{aligned} \tag{4.74}$$

Note that the symmetry group operation $\overleftrightarrow{\mathbf{\Phi}}$ is not a function of frequency or time and due to the linearity property of the Fourier transform pair, it may be taken out of the integral. Revisiting (4.72) allows for the following conclusion:

$$\vec{\mathbf{E}}_4(\vec{\mathbf{r}}_4,t) = \overleftrightarrow{\mathbf{\Phi}}\bullet\vec{\mathbf{E}}_2(\vec{\mathbf{r}}_2,t), \tag{4.75}$$

which is the same conclusion arrived at in the frequency domain in (4.61). This result shows that symmetry in the frequency domain fields implies symmetry in the time domain fields because the symmetry is preserved through the inverse Fourier transform. The inverse result, that symmetry in the time domain implies symmetry in the frequency domain, can be shown by similar arguments since the forward Fourier transform possesses the same linearity properties as the inverse transform. This implication can be formally stated as:

$$\vec{\mathbf{E}}_a(\vec{\mathbf{r}}_a,f) = \overleftrightarrow{\mathbf{\Phi}}\bullet\vec{\mathbf{E}}_b(\vec{\mathbf{r}}_b,f) \quad \rightleftarrows \quad \vec{\mathbf{E}}_a(\vec{\mathbf{r}}_a,t) = \overleftrightarrow{\mathbf{\Phi}}\bullet\vec{\mathbf{E}}_b(\vec{\mathbf{r}}_b,t) \tag{4.76}$$

4.6 Far-field Repercussions and the Vampire Signature

Although far-field electromagnetics are not of particular interest in the study of ground coupled GPR electromagnetics, a particular far-field repercussion of (4.66) that deserves special mention is the so called *vampire signature* effect introduced by Baum [38] whereby the backscattered (monostatic) fields measured from a point on the target symmetry plane exhibit no cross-polarized response in the far-field. This principle is a consequence of the zero-valued solutions such as the ones seen in (4.67)-(4.70) in combination with the far-field approximation. Here it will be shown that the vampire effect can be extended to the general bistatic (far-field) case.

This result becomes more accessible if the dyadic Green's function is rewritten in a coordinate system more conducive to general backscattering. Using the conventional *h*, *v* radar coordinates for horizontal and vertical polarizations a new basis vector forms a right handed system with $\langle \hat{\mathbf{e}}_h, \hat{\mathbf{e}}_v, -\hat{\mathbf{e}}_i \rangle$ where $\hat{\mathbf{e}}_i$ is the direction of incidence in the far-field as shown in Figure 4.9.

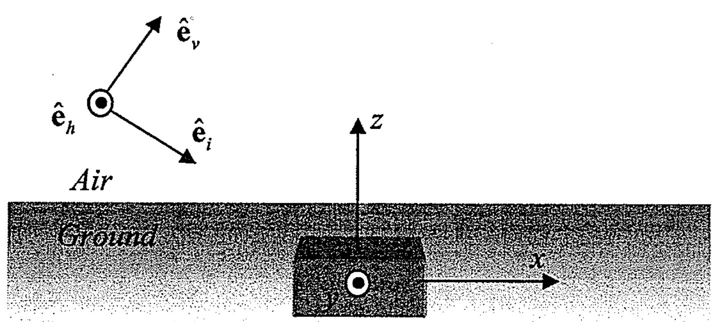

Figure 4.9 Subsurface target subjected to plane wave parallel to symmetry plane.

The matrix representation of C_{4a} of the old $\langle \hat{\mathbf{e}}_x, \hat{\mathbf{e}}_y, \hat{\mathbf{e}}_z \rangle$ coordinate system can be transformed to the new $\langle \hat{\mathbf{e}}_h, \hat{\mathbf{e}}_v, -\hat{\mathbf{e}}_i \rangle$ basis by means of a similarity transformation as in (3.9). This new set of matrices will possess the same eigenvalues as the old since

$$\begin{aligned}\left|\overline{\overline{\mathbf{B}}}\bullet\overline{\overline{\mathbf{\Phi}}}\bullet\overline{\overline{\mathbf{B}}}^{-1}-\lambda\overline{\overline{\mathbf{I}}}\right| &= \left|\overline{\overline{\mathbf{B}}}\bullet\left(\overline{\overline{\mathbf{\Phi}}}-\lambda\overline{\overline{\mathbf{I}}}\right)\bullet\overline{\overline{\mathbf{B}}}^{-1}\right| \\ &= \left|\overline{\overline{\mathbf{B}}}\right|\left|\overline{\overline{\mathbf{\Phi}}}-\lambda\overline{\overline{\mathbf{I}}}\right|\left|\overline{\overline{\mathbf{B}}}^{-1}\right| \; . \\ &= \left|\overline{\overline{\mathbf{\Phi}}}-\lambda\overline{\overline{\mathbf{I}}}\right|\end{aligned} \tag{4.77}$$

The eigenvectors that are degenerate vectors will remain in the symmetry plane as they will simply be rotated in the plane. For any target in the far-field, symmetrical or not, the dyadic Green's function in the far-field approximation will be such that all $\hat{\mathbf{e}}_i$ (i.e. longitudinal) components can be considered negligible (far-field approximation) so that

$$\overline{\overline{\mathbf{G}}}(\vec{\mathbf{r}}_i,\vec{\mathbf{r}}_i)=\begin{bmatrix} g_{hh}(\vec{\mathbf{r}}_i,\vec{\mathbf{r}}_i) & g_{hv}(\vec{\mathbf{r}}_i,\vec{\mathbf{r}}_i) & 0 \\ g_{vh}(\vec{\mathbf{r}}_i,\vec{\mathbf{r}}_i) & g_{vv}(\vec{\mathbf{r}}_i,\vec{\mathbf{r}}_i) & 0 \\ 0 & 0 & 0 \end{bmatrix}. \tag{4.78}$$

where $\vec{\mathbf{r}}_i=\overleftrightarrow{\mathbf{B}}\bullet\left[a_1(\hat{\mathbf{r}}_{dn})_1+a_2(\hat{\mathbf{r}}_{dn})_2+\ldots+a_n(\hat{\mathbf{r}}_{dn})_n\right]$ is the position vector located arbitrarily on the symmetry plane in the $\langle\hat{\mathbf{e}}_h,\hat{\mathbf{e}}_v,-\hat{\mathbf{e}}_i\rangle$ coordinate system for backscattering.

Consider the C_{4a} symmetric object depicted in Figure 4.10 where the symmetry plane in the $\langle\hat{\mathbf{e}}_x,\hat{\mathbf{e}}_y,\hat{\mathbf{e}}_z\rangle$ basis again consists of the *x*-*z* plane with unit normal $\hat{\mathbf{n}}=\hat{\mathbf{e}}_y$ such that

$$\overleftrightarrow{\mathbf{R}}=\begin{bmatrix} 1 & 0 & 0 \\ 0 & -1 & 0 \\ 0 & 0 & 1 \end{bmatrix}. \tag{4.79}$$

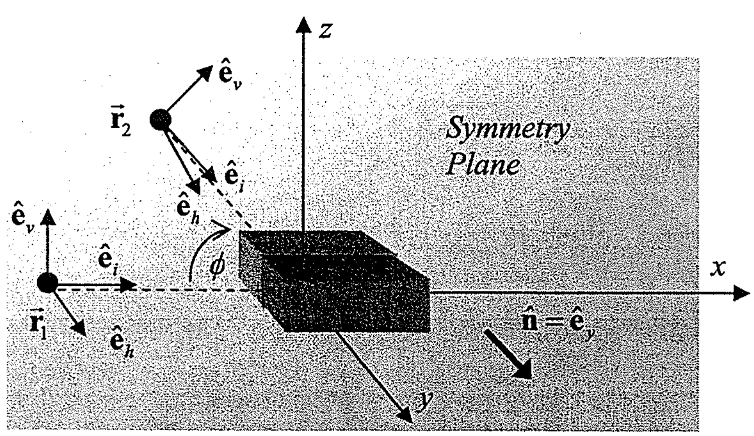

Figure 4.10 Measurement of a symmetric object on the symmetry plane: both $\hat{\mathbf{e}}_i$ and $\hat{\mathbf{e}}_v$ are parallel to the symmetry plane.

If the far-field backscatter is initially measured at a point on the x-axis at $\vec{\mathbf{r}}_1 = a\hat{\mathbf{e}}_x$ which corresponds to $\vec{\mathbf{r}}_1 = a\hat{\mathbf{e}}_i$, (4.78) will be valid as-is in the radar coordinate system since both $\langle \hat{\mathbf{e}}_x, \hat{\mathbf{e}}_y, \hat{\mathbf{e}}_z \rangle$ and $\langle \hat{\mathbf{e}}_h, \hat{\mathbf{e}}_v, -\hat{\mathbf{e}}_i \rangle$ coordinate systems coincide at this location. Making use of (4.66) and (4.78) it is clear that

$$\overline{\overline{\mathbf{G}}}_s(\vec{\mathbf{r}}_1, \vec{\mathbf{r}}_1) = \overleftrightarrow{\mathbf{R}} \cdot \overline{\overline{\mathbf{G}}}_s(\vec{\mathbf{r}}_1, \vec{\mathbf{r}}_1) \cdot \overleftrightarrow{\mathbf{R}}^{-1} = \begin{bmatrix} g_{hh}(\vec{\mathbf{r}}_1, \vec{\mathbf{r}}_1) & -g_{hv}(\vec{\mathbf{r}}_1, \vec{\mathbf{r}}_1) & 0 \\ -g_{vh}(\vec{\mathbf{r}}_1, \vec{\mathbf{r}}_1) & g_{vv}(\vec{\mathbf{r}}_1, \vec{\mathbf{r}}_1) & 0 \\ 0 & 0 & 0 \end{bmatrix}, \tag{4.80}$$

which implies that $g_{vh}(\vec{\mathbf{r}}_1, \vec{\mathbf{r}}_1) = g_{hv}(\vec{\mathbf{r}}_1, \vec{\mathbf{r}}_1) = 0$ and the off diagonal elements are all zero eliminating the cross-polarization for a current source with a given polarization so that

$$\overline{\overline{\mathbf{G}}}_s(\vec{\mathbf{r}}_1, \vec{\mathbf{r}}_1) = \begin{bmatrix} g_{hh}(\vec{\mathbf{r}}_1, \vec{\mathbf{r}}_1) & 0 & 0 \\ 0 & g_{vv}(\vec{\mathbf{r}}_1, \vec{\mathbf{r}}_1) & 0 \\ 0 & 0 & 0 \end{bmatrix}. \tag{4.81}$$

No cross-polarization will be produced in the backscatter at $\vec{\mathbf{r}}_1$. Consider now a rotation (object rotation) in the symmetry plane through the y-axis such that $\vec{\mathbf{r}}_1$ is rotated by an angle ϕ in the x-z plane. The new position $\vec{\mathbf{r}}_2$ is

$$\vec{\mathbf{r}}_2 = \overleftrightarrow{\mathbf{U}}_{yo}\left(\pi/4\right) \cdot \vec{\mathbf{r}}_1 . \tag{4.82}$$

The reflection operation in the radar coordinate system is attained by forming a similarity transformation as in (4.11) such that

$$\overleftrightarrow{\mathbf{R}}' = \overleftrightarrow{\mathbf{U}}_{yo}(\phi) \cdot \overleftrightarrow{\mathbf{R}} \cdot \left[\overleftrightarrow{\mathbf{U}}_{yo}(\phi)\right]^{-1} = \begin{bmatrix} 1 & 0 & 0 \\ 0 & -1 & 0 \\ 0 & 0 & 1 \end{bmatrix}. \tag{4.83}$$

This new rotated reflection is valid in the h, v coordinates which leads to the generalized expression of (4.80)

$$\overline{\overline{\mathbf{G}}}_s(\vec{\mathbf{r}}_2,\vec{\mathbf{r}}_2)=\overleftrightarrow{\mathbf{R}}'\bullet\overline{\overline{\mathbf{G}}}_s(\vec{\mathbf{r}}_2,\vec{\mathbf{r}}_2)\bullet\overleftrightarrow{\mathbf{R}}'^{-1}=\begin{bmatrix} g_{hh}(\vec{\mathbf{r}}_2,\vec{\mathbf{r}}_2) & -g_{hv}(\vec{\mathbf{r}}_2,\vec{\mathbf{r}}_2) & 0 \\ -g_{vh}(\vec{\mathbf{r}}_2,\vec{\mathbf{r}}_2) & g_{vv}(\vec{\mathbf{r}}_2,\vec{\mathbf{r}}_2) & 0 \\ 0 & 0 & 0 \end{bmatrix}, \tag{4.84}$$

implying again that the off diagonal elements are zero and that no cross polarization will manifest.

Notice that $\vec{\mathbf{r}}_1$ and $\vec{\mathbf{r}}_2$ are both degenerate with respect to both reflection operations defined in (4.79) and (4.83) since $\overleftrightarrow{\mathbf{R}}=\overleftrightarrow{\mathbf{R}}'$, and the general bistatic case can be stated as:

$$\overline{\overline{\mathbf{G}}}_s(\vec{\mathbf{r}}_1,\vec{\mathbf{r}}_2)=\overleftrightarrow{\mathbf{R}}'\bullet\overline{\overline{\mathbf{G}}}_s(\vec{\mathbf{r}}_1,\vec{\mathbf{r}}_2)\bullet\overleftrightarrow{\mathbf{R}}'^{-1}=\begin{bmatrix} g_{hh}(\vec{\mathbf{r}}_1,\vec{\mathbf{r}}_2) & -g_{hv}(\vec{\mathbf{r}}_1,\vec{\mathbf{r}}_2) & 0 \\ -g_{vh}(\vec{\mathbf{r}}_1,\vec{\mathbf{r}}_2) & g_{vv}(\vec{\mathbf{r}}_1,\vec{\mathbf{r}}_2) & 0 \\ 0 & 0 & 0 \end{bmatrix} \tag{4.85}$$

which implies

$$\overline{\overline{\mathbf{G}}}_s(\vec{\mathbf{r}}_1,\vec{\mathbf{r}}_2)=\begin{bmatrix} g_{hh}(\vec{\mathbf{r}}_1,\vec{\mathbf{r}}_2) & 0 & 0 \\ 0 & g_{vv}(\vec{\mathbf{r}}_1,\vec{\mathbf{r}}_2) & 0 \\ 0 & 0 & 0 \end{bmatrix} \tag{4.86}$$

The repercussion of this result is that a bistatic far-field measurement taken at points on the same symmetry plane will always exhibit no cross-polarization, regardless of antenna polarization. Specifically, if a target has $C_{\infty a}$ symmetry, then any backscattering (monostatic) measurement in the far-field will necessarily take place on a symmetry plane and the response will always have zero cross-poll. Moreover, any bistatic measurement of an object with $C_{\infty a}$ symmetry when the transmitter and receiver are located on the same symmetry plane will also result in zero cross-poll.

In analogy to a vampire that cannot see his own reflection in a mirror, a mirror symmetric object cannot see any cross-polarization in the in the far-field backscatter when measured from a point on a symmetry plane.

4.7 Measuring and Quantifying Symmetry

Whereas conventional electromagnetic reciprocity tells us nothing about the target in question, other than that the medium is isotropic, only symmetrical targets will abide by (4.63) and this suggests a method of symmetry detection using bistatic radar, by means of testing the validity of (4.63) with respect to a particular target. In order to accomplish such a task, the symmetry of a detected target must be quantified in some measurable way. The conditions given in Table 4.1 along with equations (4.26)-(4.29) and (4.53)-(4.56) make such an undertaking possible.

It has been shown that if a subsurface target with a group symmetry of order N and group representation $\overleftrightarrow{\mathbf{\Phi}}_\ell$ is present, the symmetry will manifest itself in the scattered fields in terms of its symmetric and antisymmetric components. One might therefore be tempted to record the scattered electromagnetic fields with respect to a symmetry operation and judge the symmetry or lack thereof by the symmetric and antisymmetric components alone. In such a system, a series of measurements might be taken before and after the proposed symmetry operation and then the symmetric and antisymmetric components could be derived. If the symmetric components appear dominant, one could draw the conclusion that the target has the proposed symmetry, otherwise one might conclude that the target does not possess the proposed symmetry. Assuming the target under examination was the only scatterer and no clutter was present, such a system would perhaps be reasonable. However in a practical GPR experiment, this is not the case and such a system suffers from one critical drawback: it does not differentiate between weakly and strongly scattering targets and therefore does not quantify symmetry per-sé; rather, it would only infer the proportion of the scattering that is symmetric and anti-symmetric with respect to the strength of the scattered fields. A weak scatterer that is symmetric should in fact exhibit dominance in the symmetric fields as should a strong scatterer that is symmetric. However the symmetric fields from the weaker scatterer will clearly be weaker than those of the strong scatterer. Such a system therefore does not quantify symmetry alone, it quantifies symmetry in the context of the strength of the scattered fields. Although some useful information regarding the symmetry of the scattering may be derived from such a scheme, a substantial improvement would be the quantification of target symmetry based solely on the merits of symmetry alone. This would allow the user to view the results in the context of purely symmetrical arguments that are independent of the strength of the scattered fields.

In order to quantify symmetry exclusively on a symmetrical basis, a more robust symmetry algorithm is proposed. This algorithm is based upon taking the ratio of the magnitude of the detected symmetric fields to the detected antisymmetric fields:

$$\Omega(\vec{\mathbf{r}}) = \frac{\left|\vec{\mathbf{E}}_{sy}(\vec{\mathbf{r}})\right|^2}{\left(\left|\vec{\mathbf{E}}_{as}(\vec{\mathbf{r}})\right| + \chi\right)^2}. \tag{4.87}$$

where χ is a non-negative, real constant whose sole purpose is to dampen the effects of potential singularities that may occur when a high degree of symmetry exists, i.e., when

$\left|\vec{\mathbf{E}}_{as}\right| \ll \left|\vec{\mathbf{E}}_{sy}\right|$. The quantity Ω is a unitless scalar quantity that acts as a symmetry coefficient that quantifies the symmetry of the target. This equation has a two-fold purpose: the numerator acts to emphasize regions of high symmetry whereas the denominator acts to quash regions where a high degree of antisymmetry exists. Although asymmetric targets do not necessarily possess high antisymmetry, it is expected that they will exhibit more antisymmetry than can be expected from highly symmetric targets, since symmetric targets should theoretically possess little or no antisymmetry at all. However zeros in $\vec{\mathbf{E}}_{as}$ materialize for reasons other than highly antisymmetric measurements and this can lead to instability in the equation. Issues such as measurement error and, more specifically, sidelobe nulls in the inverse FFT can cause (4.87) to blow up, resulting in skewed and unstable results. A judicious selection of the dampening factor χ can alleviate such concerns.

4.7.1 Stability of the Symmetry Coefficient Ω

Consider an initial measurement on a target such that the detected scattered field is $\vec{\mathbf{E}}(\vec{\mathbf{r}})$. A second measurement $\overleftrightarrow{\mathbf{\Phi}} \bullet \vec{\mathbf{E}}(\vec{\mathbf{r}})$ is made after a symmetry operation with group representation $\overleftrightarrow{\mathbf{\Phi}}$ in order to investigate whether or not the target has the proposed symmetry. This response may indicate strong symmetry, no symmetry or somewhere in between. Recalling the equations for the symmetric and antisymmetric components (4.53) and (4.55), equation (4.87) may be expanded to

$$\Omega(\vec{\mathbf{r}}) = \frac{\left|\vec{\mathbf{E}}(\vec{\mathbf{r}}) + \overleftrightarrow{\mathbf{\Phi}} \bullet \vec{\mathbf{E}}(\vec{\mathbf{r}})\right|^2}{\left(\left|\vec{\mathbf{E}}(\vec{\mathbf{r}}) - \overleftrightarrow{\mathbf{\Phi}} \bullet \vec{\mathbf{E}}(\vec{\mathbf{r}})\right| + \chi\right)^2}. \tag{4.88}$$

With no loss of generality, we can assume that all responses are real numbers in order to simplify the argument such that

$$\begin{aligned}\vec{\mathbf{E}}(\vec{\mathbf{r}}) &= x_1 \\ \vec{\vec{\mathbf{\Phi}}}\bullet\vec{\mathbf{E}}(\vec{\mathbf{r}}) &= x_2\end{aligned}. \tag{4.89}$$

Then (4.88) can be considered as a scalar function of the second measurement and the dampening factor χ only and can be simplified to give

$$\Omega(\chi, x_2) = \frac{|x_1 + x_2|^2}{\left(|x_1 - x_2| + \chi\right)^2}. \tag{4.90}$$

Figure 4.11 shows an example when the first measurement yields $\vec{\mathbf{E}}(\vec{\mathbf{r}}) = x_1$ and shows the result for a second measurement that varies from $-|x_1| \leq x_2 \leq |x_1|$, so that the symmetric and antisymmetric components both vary from 0 to $2|x_1|$ for several values of the dampening coefficient χ. Obviously, there is a singularity issue for the case when the second measurement approaches the first, i.e. when $x_1 \to x_2$. This problem is remedied by the inclusion of a dampening factor that is at least twice the magnitude of the initial measurement x_1. This implies that the symmetry coefficient cannot exceed a value of unity for a given measurement, while still maintaining a monotonically increasing functional relationship. This result can also be extended to complex numbers and the result is that stability of the symmetry coefficient Ω is assured, and the value of Ω is constrained to lie within $0 \leq \Omega \leq 1$ when

$$\chi \geq 2\left|\vec{\mathbf{E}}(\vec{\mathbf{r}})\right|. \tag{4.91}$$

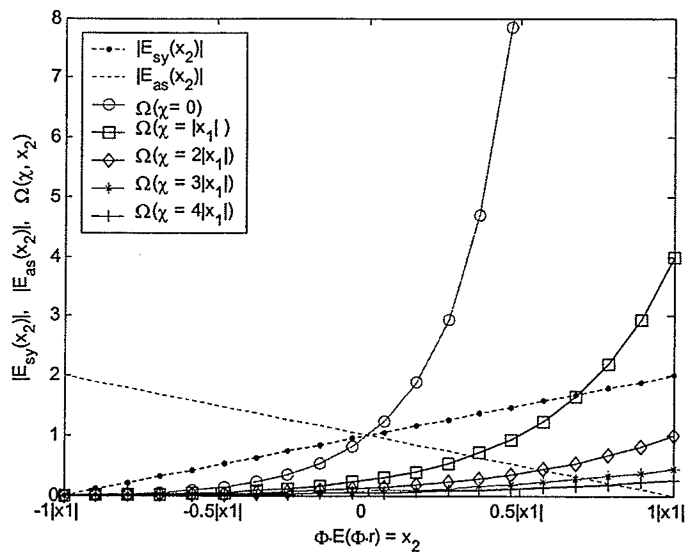

Figure 4.11 The behaviour of the symmetry coefficient when the first measurement is $\vec{\mathbf{E}}(\vec{\mathbf{r}}) = x_1$ and the second measurement ranges from $-|x_1| \leq \left(\overleftrightarrow{\boldsymbol{\Phi}}\bullet\vec{\mathbf{E}}(\vec{\mathbf{r}}) = x_2\right) \leq |x_1|$ for values of the dampening factor of χ=0, $\chi=|x_1|$, $\chi=2|x_1|$, $\chi=3|x_1|$ and $\chi=4|x_1|$.

One more convenient consequence of the proposed symmetry coefficient in (4.88) is that the symmetry of non-reflective space (zero target) will accordingly be designated as having zero symmetry in Ω since

$$\Omega(\vec{\mathbf{r}}) = \frac{\left|\vec{\mathbf{E}}(\vec{\mathbf{r}}) + \overleftrightarrow{\boldsymbol{\Phi}}\bullet\vec{\mathbf{E}}(\vec{\mathbf{r}})\right|^2}{\left(\left|\vec{\mathbf{E}}(\vec{\mathbf{r}}) - \overleftrightarrow{\boldsymbol{\Phi}}\bullet\vec{\mathbf{E}}(\vec{\mathbf{r}})\right| + \chi\right)^2} = \frac{|0+0|^2}{\left(|0-0| + \chi\right)^2} = 0, \tag{4.92}$$

which is an opportune result because we are searching for the symmetry associated with physical targets and are not interested in quantifying the symmetry of the surrounding medium.

CHAPTER 5
Symmetry Filter Algorithm

5.1 Practical Symmetry Measurements for Subsurface Targets

In order to implement an algorithm that exploits the spatial symmetry of subsurface targets, it is evident that the target measurements must undergo a transformation corresponding to an operation of a given symmetry group, so that the symmetric and antisymmetric components of the fields may be constructed. It is not convenient to consider rotations and reflections of the targets themselves, since they are buried and not readily accessible. More appropriate is a system whereby the measurement scheme undergoes the symmetry transformation while the target remains unaltered. Group theoretically and electromagnetically, both schemes are identical.

If the location of a target was known a priori with respect to the plane coincident with the ground surface, one could simply make an initial measurement, perform a symmetry operation $\overleftrightarrow{\mathbf{\Phi}}$ on the antenna system (rather than the target) and construct $\vec{\mathbf{E}}_{sy}(\vec{\mathbf{r}})$ and $\vec{\mathbf{E}}_{as}(\vec{\mathbf{r}})$ with respect to the symmetry operation as shown in Figure 5.1 for the specific example of a subsurface target with C_{4a} symmetry. The symmetry coefficient in (4.88) could then be calculated and the result would show whether or not the object possesses the prescribed symmetry. The initial location and orientation of the bistatic antenna current source pair $\vec{\mathbf{J}}_1(\vec{\mathbf{r}}_1)$ and $\vec{\mathbf{J}}_2(\vec{\mathbf{r}}_2)$ is inconsequential since all that is required to measure the symmetry is that the subsequent bistatic measurement corresponds to an operation of the target symmetry group. In the ideal case, any of the three subsequent measurements shown in Figure 5.1, $\overleftarrow{\mathbf{C}}_4^2 \bullet \vec{\mathbf{J}}_i(\vec{\mathbf{r}}_i)$, $\overleftarrow{\mathbf{C}}_4^3 \bullet \vec{\mathbf{J}}_i(\vec{\mathbf{r}}_i)$ or $\overleftarrow{\mathbf{R}} \bullet \vec{\mathbf{J}}_i(\vec{\mathbf{r}}_i)$, ($i = 1,2$) will ideally correspond to a symmetry coefficient of $\Omega(\vec{\mathbf{r}}) = 1$ (as will a measurement corresponding to $\overleftarrow{\mathbf{C}}_4 \bullet \vec{\mathbf{J}}_i(\vec{\mathbf{r}}_i)$, not depicted here). Subsequent measurements for this case are by no means limited to the operations shown since any operation listed in Table 3.1 will lead to identical results.

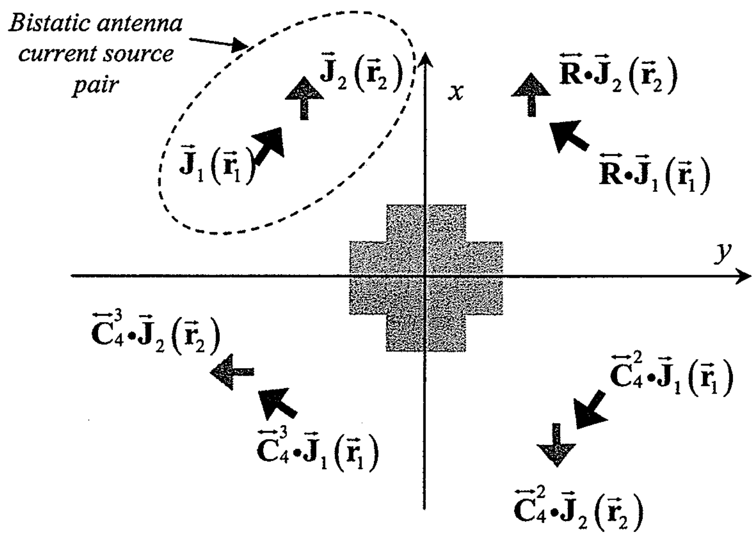

Figure 5.1 Top view of object with C_{4a} symmetry with an initial measurement by current source pair $\vec{\mathbf{J}}_1(\vec{\mathbf{r}}_1)$ and $\vec{\mathbf{J}}_2(\vec{\mathbf{r}}_2)$ and further measurements corresponding to various elements of the $\overleftarrow{\mathbf{C}}_{4a}$ group.

Consider now the object depicted in Figure 5.2 where the same experiment (various operations of the $\overleftarrow{\mathbf{C}}_{4a}$ symmetry group) are applied to an object with C_{3a} symmetry.

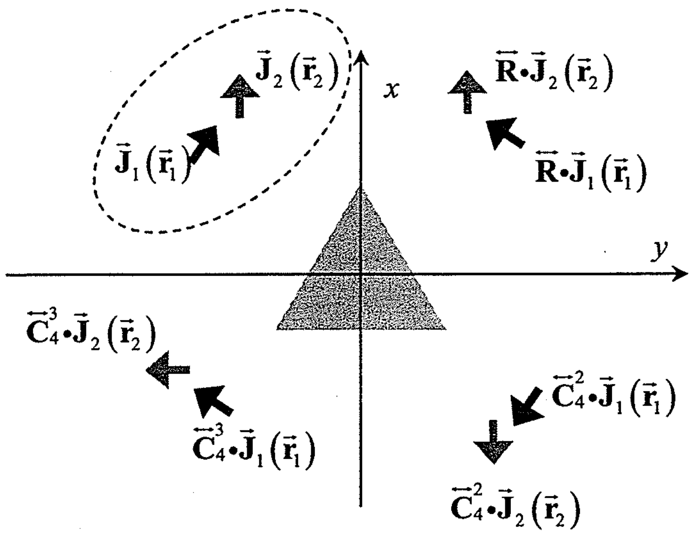

Figure 5.2 Top view of object with C_{3a} symmetry with an initial measurement by current source pair $\vec{\mathbf{J}}_1(\vec{\mathbf{r}}_1)$ and $\vec{\mathbf{J}}_2(\vec{\mathbf{r}}_2)$ and subsequent measurements of the C_{4a} symmetry group.

In this case the symmetry operations do not all yield identical results since the elements of the object's C_{3a} symmetry group are not all elements of the measurement scheme's C_{4a} symmetry operations. It is interesting to note however that there is one subsequent measurement that will indicate symmetry since the C_{4a} group and the C_{3a} group possess a common subgroup in the reflection operation $\overleftrightarrow{\mathbf{R}}$. In other words, the measurements made by $\vec{\mathbf{J}}_i(\vec{\mathbf{r}}_i)$ and $\overleftrightarrow{\mathbf{R}}\bullet\vec{\mathbf{J}}_i(\vec{\mathbf{r}}_i)$, i=1,2, will ideally correspond to a symmetry coefficient of $\Omega = 1$ since the reflection operation $\overleftrightarrow{\mathbf{R}}$ is also a member of the C_{3a} group.

It must be noted that in the development of this concept, knowledge of the physical properties of the object and its environment are never required. The principle in theory is entirely independent of the electromagnetic properties of the object, its physical (or electrical) dimensions and its range. All that is required is that the object posses the same symmetry as the measurement symmetry operation and that it is vertical relative to the plane in which the measurements are taken. In practice of course, one would not expect things to be quite so simple. Substantial dielectric or conductive contrast between the object and its surrounding medium, as well as the target being located within a reasonable proximity to the measuring antenna all make for relatively more convenient, practical and accurate measurements. The major drawback in the procedure defined so far is the lack of a priori knowledge of the location with respect to the surface plane. Such knowledge cannot be assumed in general GPR applications and a method to circumvent this requirement will be introduced in the following section.

5.2 Implementation of Symmetry from B-Scan Data

As mentioned previously, in practical GPR experiments, no a priori information regarding the position of the subsurface target can be assumed since the targets are buried beneath an opaque ground surface. Obviously, if some knowledge of the target's location were available, the job of measuring the symmetry could be accomplished by the means outlined in the previous section. However, since this is generally not the case and physically implementing the previous method would be tedious and inefficient, a more robust method is needed. The algorithm should make use of traditional B-scan data, as outlined in section 2.6, so that it may be conveniently applied to traditional GPR data and that no special new measuring scheme is required other than conventional synthetic aperture data collection.

It turns out that such a method is possible under the conditions that multiple B-scan measurements are taken parallel to one another and that the subsurface targets and antenna current sources are identical and possess even group symmetries themselves such that the target and bistatic antenna pair can be described by a group matrix representation of the form

$$C_{2Ka}, \quad \text{K}=1,2\ldots\infty. \tag{5.1}$$

Consider a 2 dimensional 3×3 Cartesian grid shown in Figure 5.3, where three B-scans of data are collected along the paths denoted by scan A, scan B and scan C, located along corresponding lines y_1, y_2 and y_3, with three bistatic measurements along each path taken at points (x_i, y_j) at the grid nodes, such that the ground surface and buried targets reside below the 2D grid. Figure 5.3 can then be considered a top-view perspective of three individual B-scans searching for targets below in the plane of the page. In this depiction, two bistatic measurements are shown.

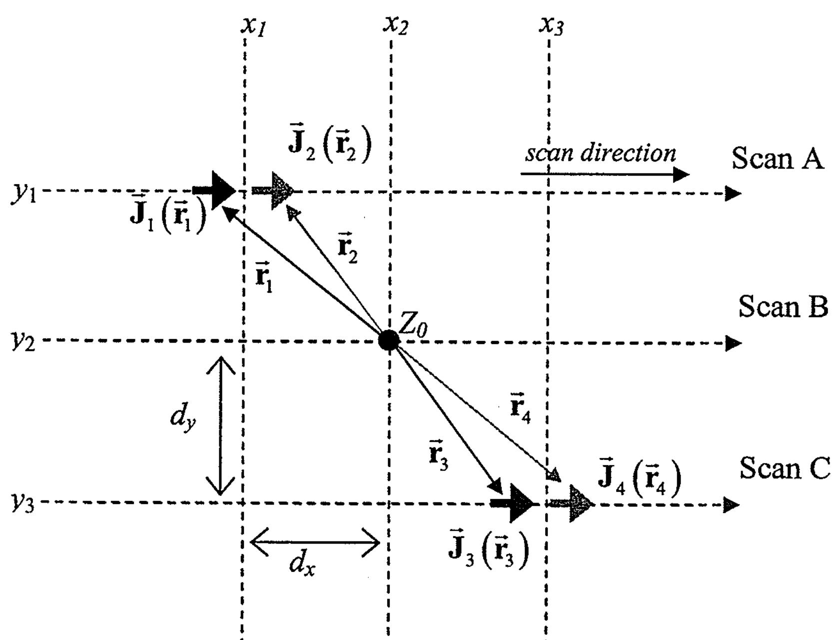

Figure 5.3 Top view of measurement system. There are three B-scans in parallel with the central B-scan (scan B) taken through Z_0.

Initially, a measurement is taken by the bistatic pair located at the first node (x_1, y_1) when the current source antennas $\vec{\mathbf{J}}_1$ and $\vec{\mathbf{J}}_2$ are at locations $\vec{\mathbf{r}}_1$ and $\vec{\mathbf{r}}_2$ respectively with respect to the origin Z_0. The current source pair then moves to the second node at (x_2, y_1) and so on until the antenna completes scan A. The source pair then moves down to complete scans B and C respectively. The requirements for the selection of the source pair locations or orientations with respect to one another are that their individual symmetry axes must coincide with the travel path of the synthetic aperture and that the antennas, which are required to have C_{2Ka} symmetry, must be positioned so that they are at least C_{2a} symmetric as a pair with respect to their bisector. The bisector is the line located half way between the bistatic antennas. This implies that their polarization axis must be parallel or perpendicular to the scan path. The requirement is depicted in Figure 5.4(a) which shows a close-up of the bistatic antenna structure for the case when the polarizations are parallel to the scan path. One should not be fooled by the apparent lack of symmetry due to the directionality of the arrow symbols that represent the antenna current sources and that are used for convenience since, as previously stated, the individual antennas must be at least C_{2a} symmetric. The C_{2a} symmetry assumed of a single antenna is depicted in Figure 5.4(b).

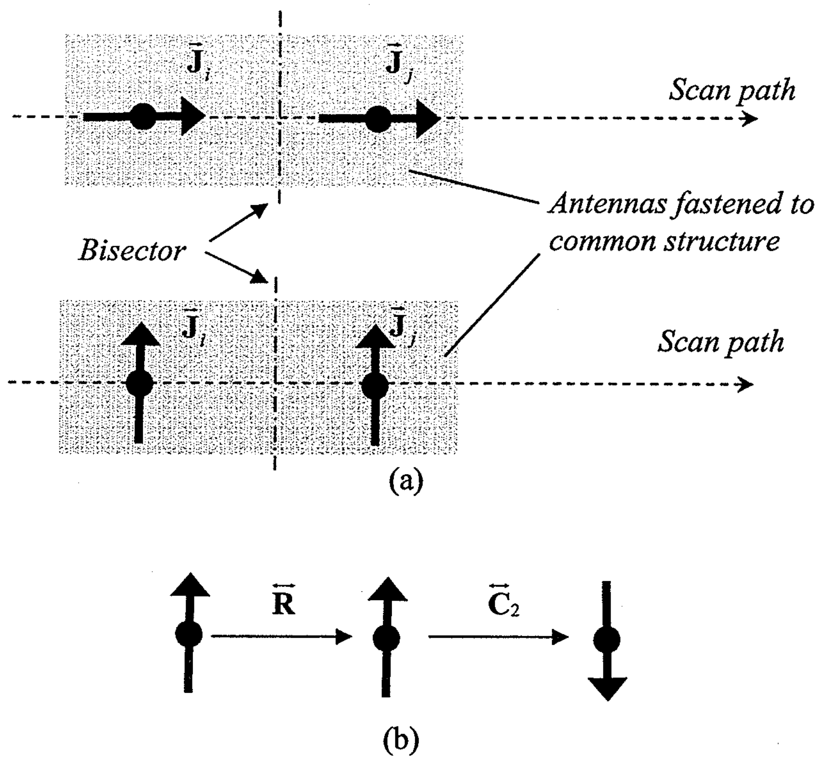

Figure 5.4 The bistatic antenna pair $\vec{\mathbf{J}}_i, \vec{\mathbf{J}}_j$ moves as a single unit. (a) The polarization axes are aligned either parallel or perpendicular to the scan path. (b) Both axes of symmetry reside on the current scan path and the entire unit possesses $\vec{\mathbf{C}}_{2a}$ symmetry about its bisector.

These restrictions do not preclude circular or even elliptical polarization since elliptic polarization still implies C_{2a} symmetry while circular polarization commands $C_{\infty a}$, both of which are included in the original C_{2Ka} requirement. For the case of elliptical polarization, the restrictions translate into the requirement that either both major or both minor polarization axes be parallel or perpendicular to the scan path. Polarization orientation is not a concern for perfectly circularly polarized antennas as long as the axis of rotation resides on the scan path.

Note that since no distinction is made between transmitter and receiver, either antenna may fulfill either task. The only other requirement is that their *relative* orientations and separations do not change from measurement to measurement. In other words, we must assume that the antennas are fastened to a common structure that moves along the scan path as a single unit and that this unit is unchanged during the entire experiment.

Upon inspection it would appear that no conventional symmetry operation has been undertaken since no rotations or reflections of the measurement scheme have been performed, so symmetry measurements appear to be out of the question. This is however not the case. Shown in Figure 5.5 is the consequence of the application of the $\overleftrightarrow{\mathbf{C}}_2$ rotation symmetry operation to the current source pair $\vec{\mathbf{J}}_1(\vec{\mathbf{r}}_1)$ and $\vec{\mathbf{J}}_2(\vec{\mathbf{r}}_2)$ with respect to the origin Z_0.

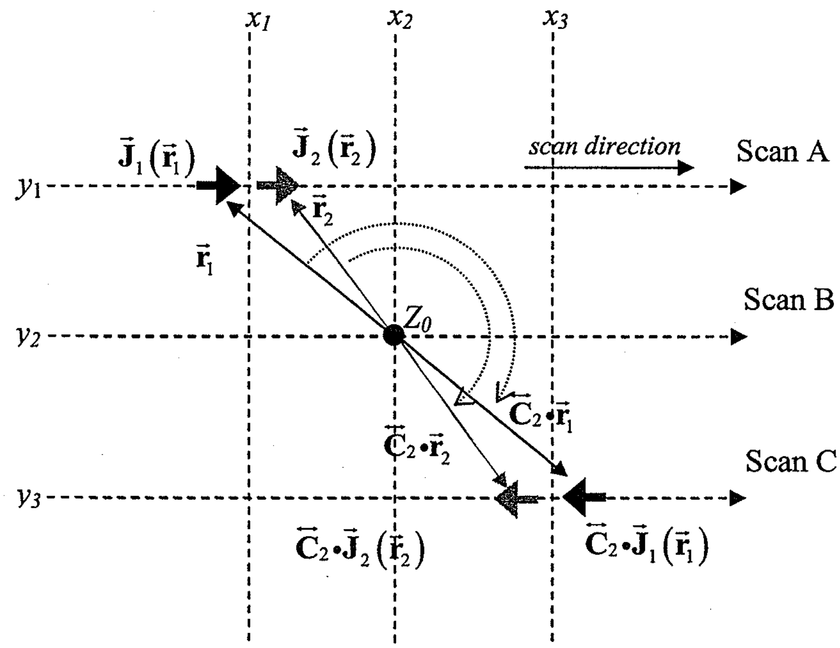

Figure 5.5 The $\overleftrightarrow{\mathbf{C}}_2$ rotation operation performed on the bistatic pair $\vec{\mathbf{J}}_1(\vec{\mathbf{r}}_1)$ and $\vec{\mathbf{J}}_2(\vec{\mathbf{r}}_2)$.

Revisiting Figure 5.3 suggests that no progress has been made since the rotated bistatic pair $\overleftarrow{\mathbf{C}}_2 \bullet \vec{\mathbf{J}}_1(\vec{\mathbf{r}}_1)$ and $\overleftarrow{\mathbf{C}}_2 \bullet \vec{\mathbf{J}}_2(\vec{\mathbf{r}}_2)$ appear to differ fundamentally from the original scan geometry for $\vec{\mathbf{J}}_3(\vec{\mathbf{r}}_3)$ and $\vec{\mathbf{J}}_4(\vec{\mathbf{r}}_4)$. At this point the conventional electromagnetic reciprocity relation defined in (2.49) is invoked to rectify this seemingly troublesome result. The reciprocity theorem guarantees that if the transmitter and receiver are interchanged, regardless of their geometry and orientation, the same response will be recorded. The concept is shown in Figure 5.6 where an arbitrary scatterer (not necessarily symmetric) is submitted to a bistatic measurement where the transmitter and receiver are pre-determined and the antennas identical. Due to reciprocity, the measured response will be identical for the case when the antenna roles are reversed as shown in Figure 5.6(a).

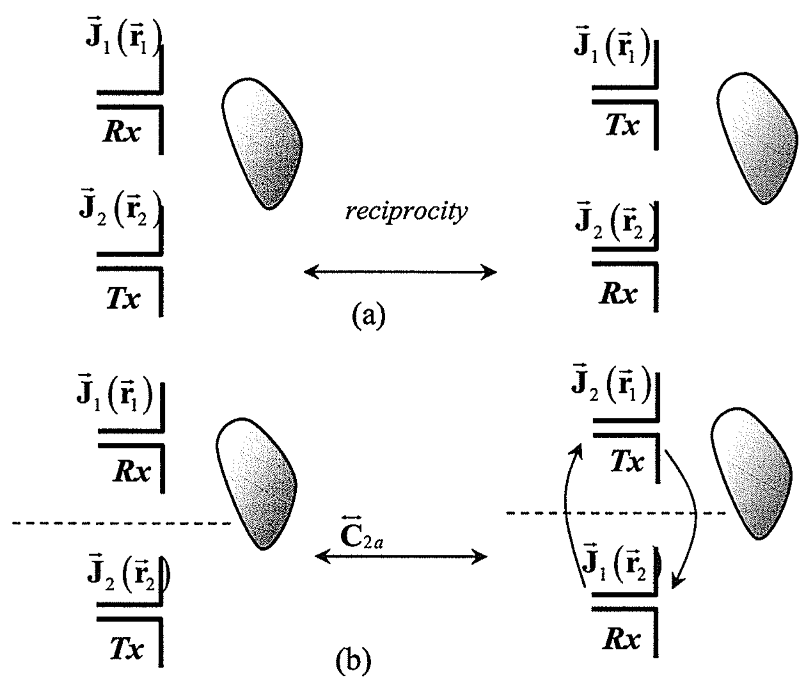

Figure 5.6 Conventional reciprocity is equivalent to a C_{2a} group operation with respect to a symmetric bistatic antenna pair. (a) Bistatic measurement geometry and reciprocity, (b) the $\overleftarrow{\mathbf{C}}_{2a}$ symmetry operation. The results for both cases are identical.

If, however, the individual antennas possess C_{2Ka} symmetry such that the antenna symmetry axis and the target symmetry axis are parallel and the antennas are identical however, conventional reciprocity may be taken one step further so that not only the *roles* of transmitter and receiver may be interchanged, but also the *positions* of transmitter and receiver. In the lexicon of group theory, we may state that *the measurement is invariant to a C_{2a} group operation on the bistatic pair* [39]. Stated formally, for a target with C_{2Ka} symmetry, the $\overleftrightarrow{\mathbf{C}}_2$ rotation operation on a bistatic antenna system, that is also symmetric with respect to its own bisector, will result in the following relations:

$$\vec{\mathbf{J}}_3(\vec{\mathbf{r}}_3) = \overleftrightarrow{\mathbf{C}}_2 \bullet \vec{\mathbf{J}}_2(\vec{\mathbf{r}}_2), \tag{5.2}$$

$$\vec{\mathbf{J}}_4(\vec{\mathbf{r}}_4) = \overleftrightarrow{\mathbf{C}}_2 \bullet \vec{\mathbf{J}}_1(\vec{\mathbf{r}}_1). \tag{5.3}$$

Without ever performing a rotation or reflection operation, a symmetric measurement of the C_{2a} group has been executed!

The implication of (5.2) and (5.3) is that if a target with C_{2Ka} symmetry happens to reside at the origin Z_0, then since the C_{2a} group is necessarily a subgroup of the target group, the symmetry of the target can be captured by means of the methods outlined in Chapter 4 and the symmetry coefficient Ω of the target can be calculated for the case of C_{2a} symmetry. Figure 5.7 outlines an example of a subsurface target with C_{4a} symmetry located at the grid origin.

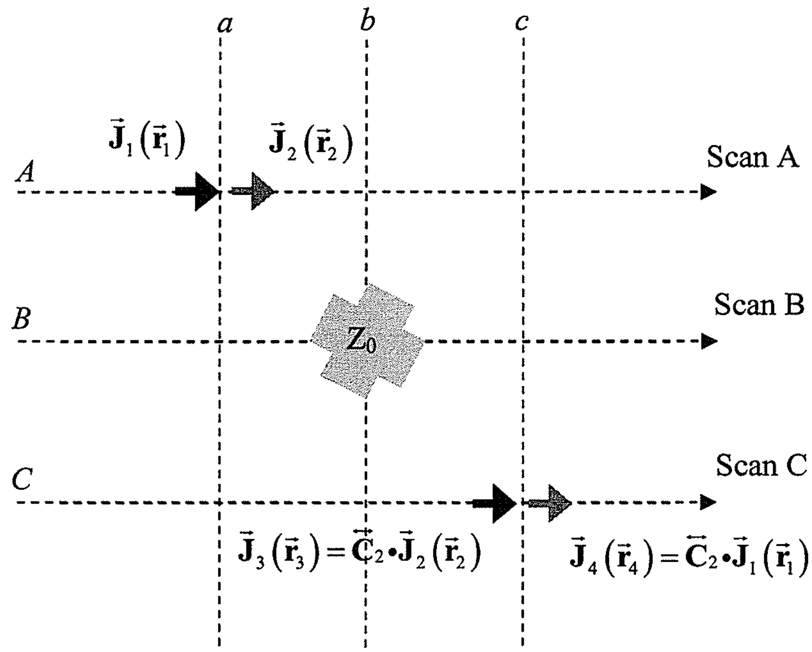

Figure 5.7 A target resides at Z_0 and measurements taken along parallel B-scans are equivalent to a C_{2a} symmetry operation

It is interesting and gratifying to note that the target centered at the origin need not be aligned in the plane in any particular manner. The demands of the theory place no restrictions on having the target initially rotated to any particular position. All that is required is that the target possess C_{2Ka} symmetry and that it be centered at the grid origin.

The last requirement appears to be somewhat of a limiting factor since if no a priori knowledge of the target's location is known, then it appears unlikely that it will find itself at the origin of the measurement grid as in Figure 5.7. This is not the case if the method is applied thoughtfully. Figure 5.8(a) shows the case where the target's location is not known in advance, other than that it resides somewhere on the centre scan line. The double edged arrows symbolize the symmetric bistatic pair. The method is first applied at the beginning of the 3 row B-scan and then is applied one position over and so on. In a sense, the measurement origin Z_0 can be said to move along the scan path. This can be considered as a *symmetry filter* window that slides along the B-scan data, calculating the symmetric and antisymmetric fields for the case of C_{2a} symmetry at each window position.

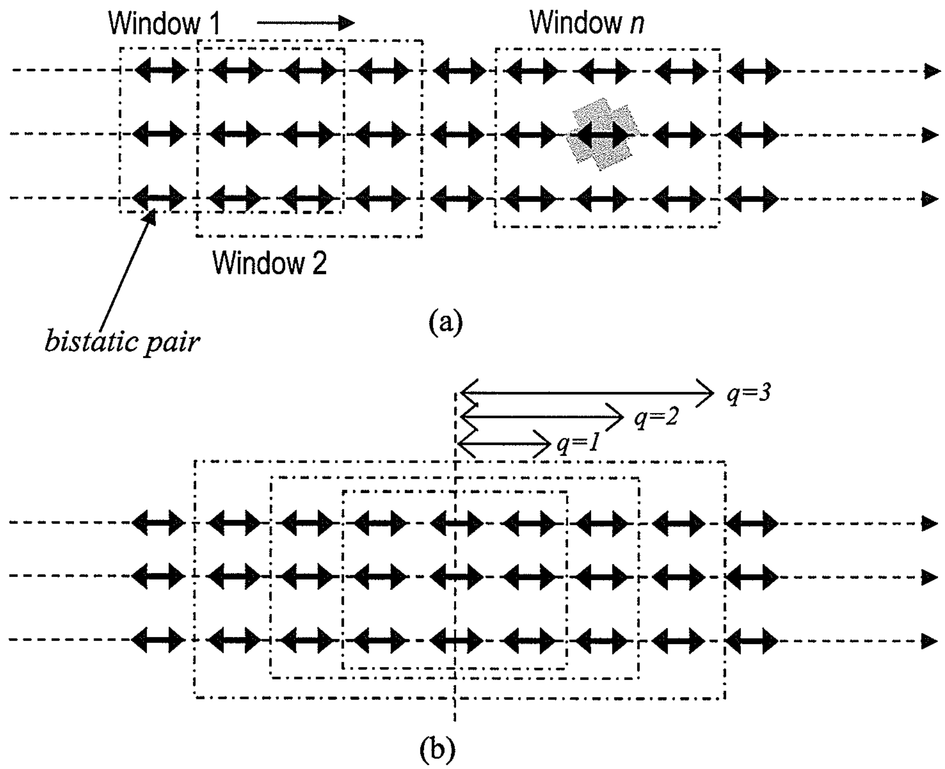

Figure 5.8 The symmetry filter acts as a moving window whereby the origin for Figure 5.5 moves along the scan path. (a) Symmetry measurement taken by window 1, then by window 2 and so on. (b) The size of the symmetry filter window is defined by q.

In Figure 5.8(b) we see that it is possible to apply filter windows greater than 3×3. The window may be as large as $3\times(2q-1)$ where q defines the length of the window up to the number of measurements per B-scan. However, as the filter window is made larger, the number of windowed observations possible on a finite length B-scan will become smaller, and windowed observations near the extremities of the scans will become less available.

If the B-scan measurements consist of n individual A-scans of data along each row and the symmetry filter window size is m then in general, the size of the post-symmetry filtered data will be

$$length(\text{Symmetry Filtered Data}) = n - m + 1\,. \tag{5.4}$$

Furthermore it is apparent from Figure 5.8(a) that the A-scans at the extremities (the first and last measurements) can not be analyzed for symmetry, because the C_{2a} group operation can not be implemented at these locations, due to lack of data beyond the extremities. As the filter window size grows, so too will the amount of data at the extremities that will become unavailable for symmetry analysis.

Because the symmetry filter uses the gathered data to calculate symmetric and antisymmetric fields, it is apparent that, despite requiring three B-scans of data on a two dimensional grid, the symmetry filter algorithm's post-processed results will lead only to a single set of symmetry filtered 2D B-scans of data. Specifically, the two exterior B-scans (scan A and scan C) are used to calculate one set of symmetric and antisymmetric fields. In this thesis, the central scan (scan B) is used only as a gauge by which to compare the results of a raw GPR B-scan with the results from symmetry filtering.

The limitation of dealing only with targets that possess C_{2Ka} symmetry might seem to be a hindrance to the general problem of landmine detection, however it turns out that a substantial proportion of landmines do in fact support the C_{2Ka} symmetry group. Figure 5.9 shows several examples of common landmines in production and/or in use today that exhibit symmetry encompassed by the $\overleftarrow{\mathbf{C}}_{2Ka}$ requirement for the proposed symmetry filter algorithm. The symmetry groups associated with these mines varies from $\overleftarrow{\mathbf{C}}_{2a}$ to $\overleftarrow{\mathbf{C}}_{\infty a}$ so that the proposed theory can apply to them all.

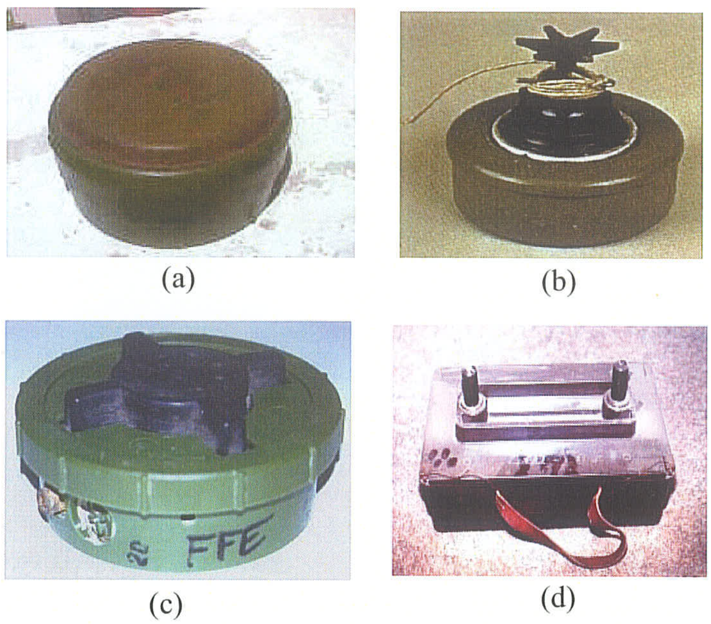

Figure 5.9 Some common landmines presently in production and/or in deployment and their corresponding group symmetries [40]: (a) The T72A (China) with $\overleftarrow{\mathbf{C}}_{\infty a}$, (b) PMA-2 (Yugoslavia) with $\overleftarrow{\mathbf{C}}_{\infty a}$, (c) PMN-2 (fmr. U.S.S.R.) with $\overleftarrow{\mathbf{C}}_{4a}$, (d) PT-MI2 (fmr. Czechoslovakia) $\overleftarrow{\mathbf{C}}_{2a}$

5.3 Implementation of Symmetry Filter Algorithm for GPR

The task at hand is to use the principles outlined in the previous section, and to implement it with regards to (2.70), which will be restated here for convenience:

$$u(m,l)=\frac{1}{N}\sum_{n=1}^{N}U_n e^{-2\pi(m-1)(n-1)/N}, \quad \begin{array}{l} m=1,2,\ldots,N \\ l=1,2\ldots,L \end{array}. \tag{5.5}$$

As alluded to previously, the algorithm will require more than one B-scan in order to gain insight into the symmetry properties of a target. The measurement setup required to collect the data that is necessary for the symmetry filter algorithm is shown in Figure

5.10. As noted earlier, it is assumed that no knowledge of the subsurface targets exists a priori other than that they are centered on the central B-scan (scan B). The data is collected according to (5.5) in the usual manner: the measurement system collects the B-scan data $u_A(m,l)$, $u_B(m,l)$ and $u_C(m,l)$ along scans A, B and C respectively as shown in the depiction below.

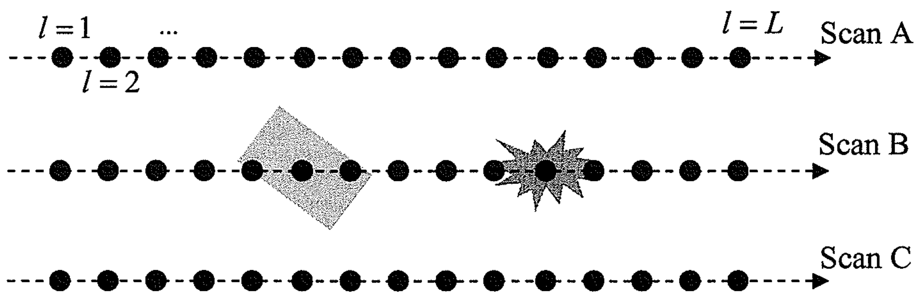

Figure 5.10 Measurement setup for the symmetry filter algorithm. B-scans $u_A(m,l)$, $u_B(m,l)$ and $u_C(m,l)$ are recorded for scan paths A, B and C respectively.

Let us assume that the measurements $u_A(m,l)$, $u_B(m,l)$ and $u_C(m,l)$ have been successfully recorded under the appropriate conditions. The data collections $u_A(m,l)$ and $u_C(m,l)$ are made into a $N \times L$ image. For the sake of clarity we will visualize only a single row of data corresponding to a single range bin. This single row of data corresponds to a single row of pixels as shown in Figure 5.11 where the pixelated images for scans A and C are shown (the data in scan B is not required for reasons other than comparison). We will assume that a target which possesses the required symmetry in (5.1) so that $\overleftrightarrow{\mathbf{C}}_{2a}$ will be a subgroup of the target symmetry, and that this target is centered at the τ_{th} measurement in the cross range as shown. The values for $u_A(1,l)$ and $u_C(1,l)$ ($l = 1, 2, \ldots, L$) are assigned colors in their pixels related to their recorded values.

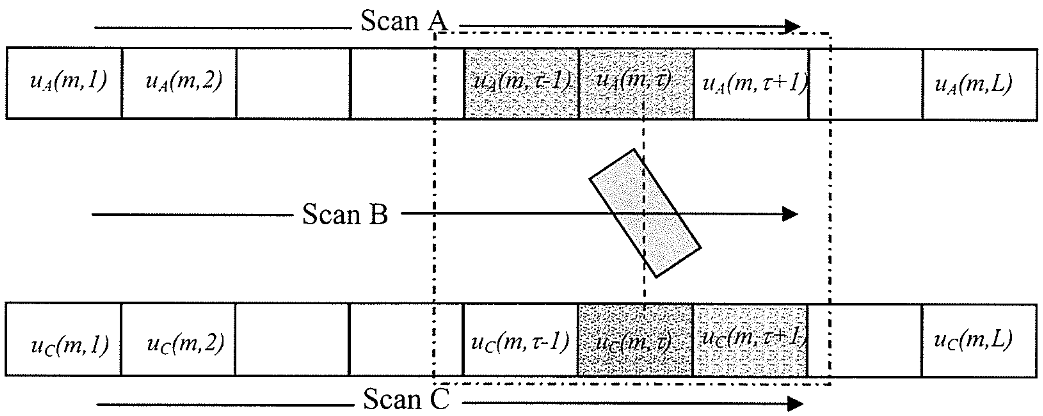

Figure 5.11 Single range bin from a B-scan. The pixels coloration reflects the C_{2a} symmetry of the observed target

It can be seen from the diagram that the symmetry filter method outlined in the previous sections can be implemented for a window size of q=1 (see Figure 5.8) by calculating the symmetric and antisymmetric pixels, in a manner reminiscent of the field calculations of section 4.3 through the following relations:

$$u_{sy}^{(1+)}(m,\tau) = u_A(m,\tau+1) + u_C(m,\tau-1), \tag{5.6}$$

$$u_{as}^{(1+)}(m,l) = u_A(m,l+q) - u_C(m,l-q), \tag{5.7}$$

$$u_{sy}^{(1-)}(m,\tau) = u_A(m,\tau-1) + u_C(m,\tau+1), \tag{5.8}$$

$$u_{as}^{(1-)}(m,\tau) = u_A(m,\tau-1) - u_C(m,\tau+1), \tag{5.9}$$

where the superscript (1+) implies that the symmetric and antisymmetric parts have been calculated for a window of size 1 with the data directly to the right of τ on the first scan (scan A). The superscript (1-) denotes that the symmetric and antisymmetric data to the left of τ on the first scan has been used.

The symmetry coefficient Ω of (4.87) can now be calculated by performing

$$\Omega(m,\tau)=\frac{\left|u_{sy}^{(1+)}(m,\tau)\right|^2}{\left(\left|u_{as}^{(1+)}(m,\tau)\right|+\chi\right)^2}+\frac{\left|u_{sy}^{(1-)}(m,\tau)\right|^2}{\left(\left|u_{as}^{(1-)}(m,\tau)\right|+\chi\right)^2} \tag{5.10}$$

where we will take $\chi=2\max\left\{\left|u_A(m,\tau)\right|,\left|u_C(m,\tau)\right|\right\}$ as in equation (4.91).

The preceding results can now be generalized to arbitrary points in the cross range l and arbitrary window size q over the entire B-scans:

$$u_{sy}^{(q+)}(m,l)=u_A(m,l+q)+u_C(m,l-q),\quad q\le l\le L-q, \tag{5.11}$$

$$u_{sy}^{(q-)}(m,l)=u_A(m,l-q)+u_C(m,l+q),\quad q\le l\le L-q, \tag{5.12}$$

$$u_{as}^{(q+)}(m,l)=u_A(m,l+q)-u_C(m,l-q),\quad q\le l\le L-q, \tag{5.13}$$

$$u_{as}^{(q-)}(m,l)=u_A(m,l-q)-u_Cm(m,l+q),\quad q\le l\le L-q. \tag{5.14}$$

The symmetry coefficient is then

$$\Omega^{(q)}(m,l)=\sum_{m=1}^{q}\left(\frac{\left|u_{sy}^{(q+)}(m,l)\right|^2}{\left(\left|u_{as}^{(q+)}(m,l)\right|+\chi\right)^2}+\frac{\left|u_{sy}^{(q-)}(m,l)\right|^2}{\left(\left|u_{as}^{(q-)}(m,l)\right|+\chi\right)^2}\right),\quad q\le l\le L-q, \tag{5.15}$$
$$\chi=2\max\left\{\left|u_A\right|,\left|u_C\right|\right\}$$

where the result for a window size q is taken to be the sum of symmetry coefficients from 1 to q.

Equation (5.15) results in an $N\times(L-2q)$ image that depicts the symmetry coefficient as a function of location. One final hurdle remains: the highly symmetric ground reflection. It was stated in section 4.4 that a prerequisite for the analysis of subsurface target symmetry was the existence of translational $\mathcal{T}_2 \otimes C_{\infty a}$ symmetry for the ground plane and that the symmetry of the ground possesses C_{2a} as a subgroup and will therefore be recognized as a symmetric response. The electromagnetic response from the ground can then be expected to manifest itself largely in Ω. This is unfortunate since the ground interface is always prevalent and usually provides a dominant response. In this thesis, this problem is not directly addressed and is left for future research. The issue is dealt with by disregarding the ground reflections entirely, and selecting only data in Ω that resides below the air-ground interface.

Many of the characteristics inherent in a conventional B-scan will be maintained in Ω, as long as the target in question possesses the required symmetry. Notably, the range migration effects discussed in section 2.6.4 that are prevalent in the cross-range may also manifest itself in the symmetry filtered data. This implies that conventional SAR post-processing algorithms such as conventional migration SAR focusing algorithms may also be applied to Ω. The process for implementation of the symmetry filter are displayed algorithmically in Figure 5.12.

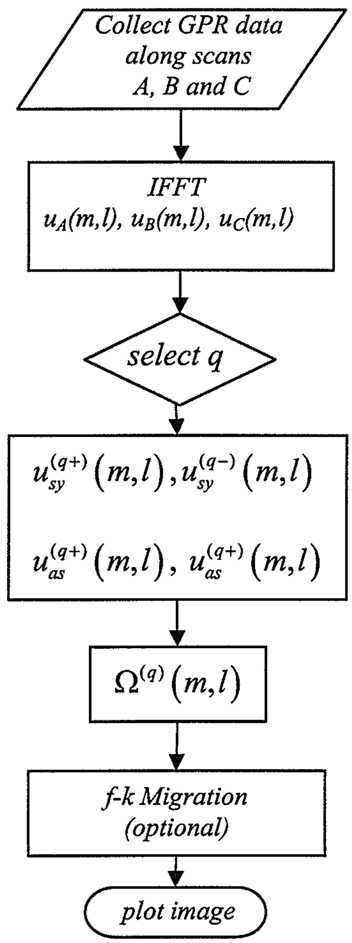

Figure 5.12 Symmetry filter method in algorithmic form

Equation (5.15) has been implemented in the Matlab© computational software environment and the code can be found in Appendix 1.

CHAPTER 6
Experiments and Results

6.1 Experimental Setup and Practical Considerations

6.1.1 Antenna

The symmetry algorithm presented in Chapter 6 has been formulated for the general case of bistatic scattering with identical antennas. Furthermore, practical imaging requires a high bandwidth system (corresponding to a small range resolution ΔR) in order to create high resolution images and therefore two identical high bandwidth antennas are required to implement the algorithm for the general bistatic case. Unfortunately, two identical antennas fitting this requirement could not be made available in the laboratory to perform the bistatic experiments. All measurements have therefore been performed as monostatic measurements with a single wideband antenna. Constraining measurements to the monostatic case does not alter the proposed formulation and algorithm since the monostatic case is just a special case of the more general bistatic regime where the transmitting antenna and receiving antenna are co-located. In the following experiments, the antenna employed is the H-1479 wideband double-ridged horn from BAE Systems with an operational bandwidth of 11.4GHz from 1GHz to 12.4GHz. The main characteristics of the horn are shown in Table 6.1 and a picture of the horn is shown in Figure 6.1.

Table 6.1

Frequency [GHz]	Gain (Nominal) [dBiL]	VSWR (Max)	VSWR (Typ)	3dB Beamwidth (Nominal) [Deg] E	H
1.0-12.4	6.0 to 12.0	3.0	2.0	50	45

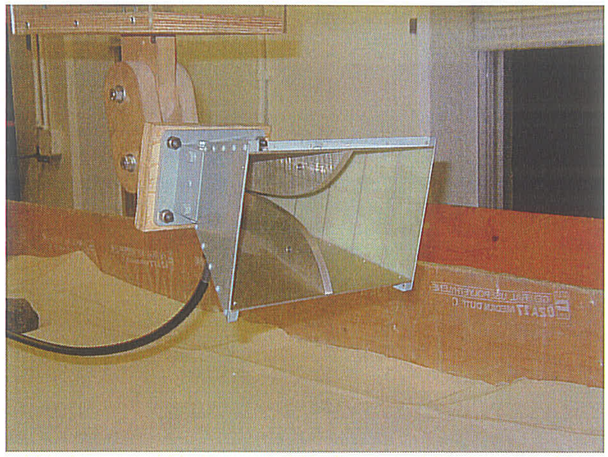

Figure 6.1 BAE H-1479 Double-ridged horn used in measurements

6.1.2 Measurement System

The design for the measurement system is shown in Figure 6.2. At the heart of the system is a PC workstation which controls and records the measurements through a graphical user interface (GUI) created in the Labview© programming environment.

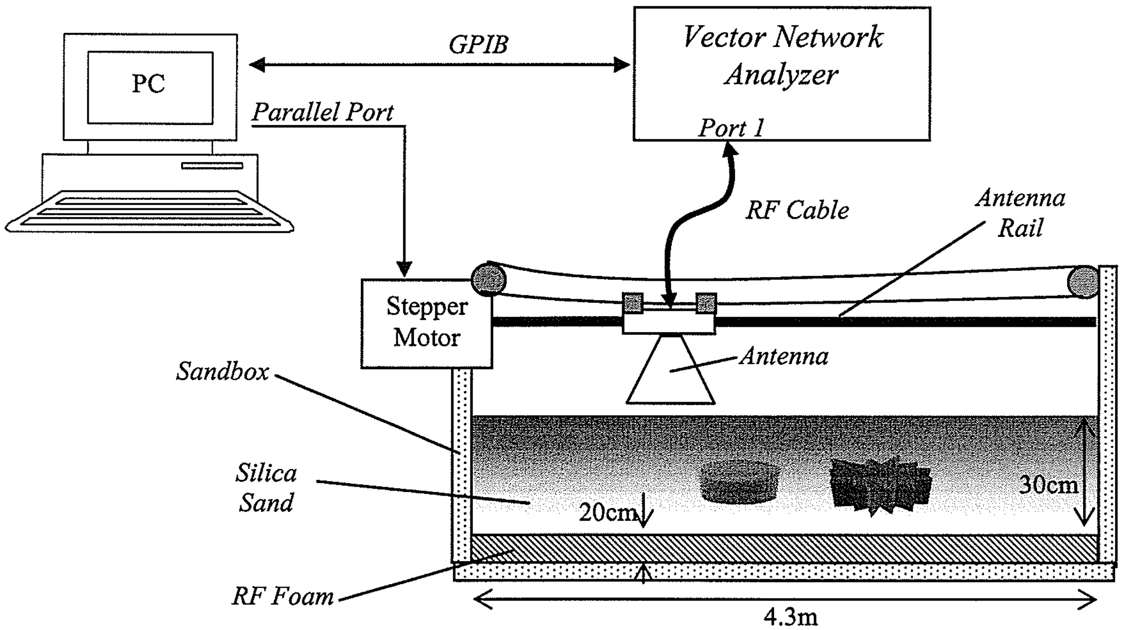

Figure 6.2 Experimental measurement setup

The measurements were taken in a custom built indoor testing environment that consists of a wooden sandbox with a mobile antenna rail unit mounted along the top of the sandbox. The sandbox measures $1.1\text{m} \times 4.3\text{m}$ in surface area and when spread evenly is filled with approximately 30cm of silica sand. Below the sand is a 20cm layer of absorptive RF foam in order to absorb energy and reduce the reflections from the bottom of the sandbox. The wideband horn antenna is itself mounted on a trolley cart with wheels designed to roll effortlessly along the rail. The antenna/trolley unit is fastened to a drive-belt attached to a stepper motor that provides mechanical power to move the antenna unit accurately to desired locations along the rail. A picture of the actual complete sandbox/VNA setup is shown in Figure 6.3.

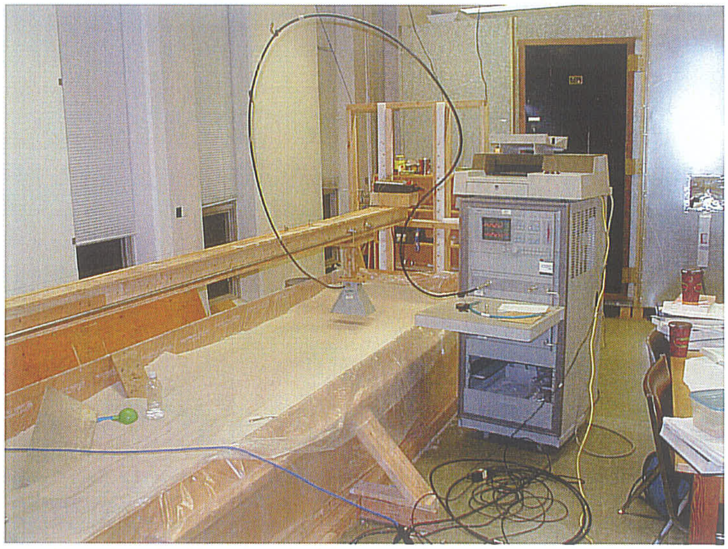

Figure 6.3 Picture of the actual GPR experimental measurement system including the Anritsu 360B VNA (right), sandbox and mobile antenna rail system. The stepper motor system (black box) can be seen on top of the rail.

All measurements are initiated and recorded by the PC through a GPIB connection to an Anritsu Model 360B vector network analyzer. The output power from the VNA is a constant 5dBm across the frequency spectrum of operation (this is the maximum output available from the VNA). The VNA is connected to the measurement horn antenna at port 1 of the VNA through a 6m long RF cable. All measurements taken are therefore S_{11} measurements as described in section 2.6.1. Operating in conjunction with the VNA measurements is a parallel port connection to the stepper-motor that controls the position of the antenna in order to facilitate accurate and automated B-scan data measurement.

A screen shot of the Labview© GUI is shown in Figure 6.4. The GUI is designed so that all system parameters regarding frequency and antenna displacement can be directly controlled from the PC. Both the parallel port stepper motor connection and GPIB connection to the VNA are managed by this program. All data is then exported from this program for post-processing in Matlab©.

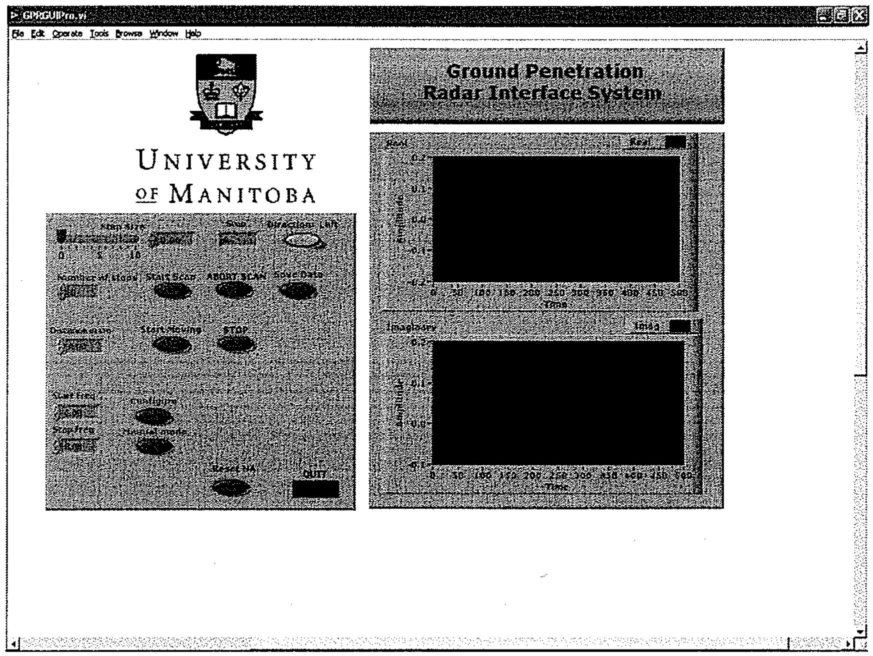

Figure 6.4 Labview© GUI controller for GPR system screen shot

6.1.3 Measurement Specifications

All experimental measurements consisted of a series of three parallel B-scans of equal length (in the cross range). The length of these measurements varied from experiment to experiment in order to reflect the size of the domain under investigation. An experiment involving three targets involved longer B-scan measurements in the cross range than did an experiment involving a single target. That said, all B-scans consisted of equally spaced incremental spatial steps of 1cm in the cross range so that the length of a particular B-scan is always $L\times1$cm, where L is the number of spatial samples in the cross-range. Furthermore, all stepped frequency A-scan measurements consisted of exactly N=501 frequencies spanning the entire operational bandwidth of the horn antenna. This is to say that all individual A-scan measurements consisted of 501 frequency steps of 24.75MHz spanning from 1GHz to 12.4GHz. The arangement is depicted in Figure 6.5.

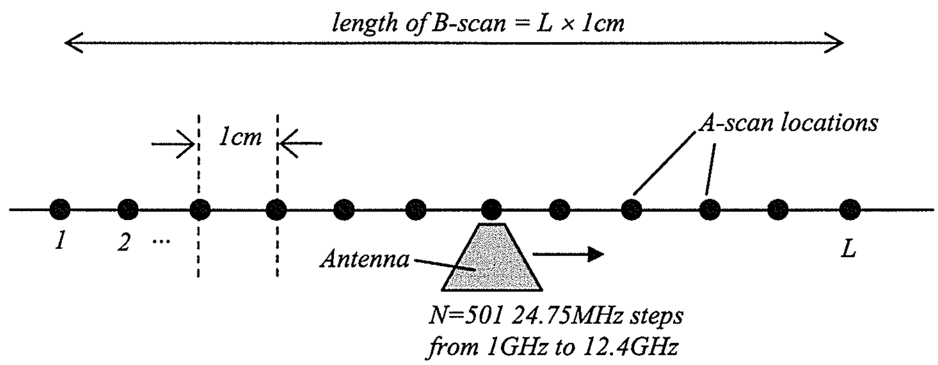

Figure 6.5 Dimensions for a typical GPR measurement

The silica sand used as the ground medium has a relative dielectric constant that was measured to be $\varepsilon_r = 2.4$. By virtue of (2.62), the expected range resolution of the radar system is

$$\Delta R = \frac{\left(\frac{c}{\sqrt{2.4}}\right)}{2(11.4GHz)} = 0.85cm. \tag{5.16}$$

For N=501 frequency steps and $\Delta R = 0.85cm$, one can expect the radar to "see" a distance of $N\Delta R = 4.29m$ without ambiguity. Since the targets of interest lie within the sand layer of the sandbox and are therefore restricted to the first 28cm below the air/sand interface, the results presented will be shown only to depths of interest and much of the data corresponding to deeper depths are neglected. Also, to improve the aesthetics of the resulting images, zero padding is introduced into the raw data at a ratio of 7:1 such that 7×501=3507 zeros are appended to the end of the raw data before the IFFT algorithm is implemented in all cases. Although this does not change the resolution of the radar, the resulting images appear more smooth and appealing to the eye.

The VNA/cable system was calibrated to the end of the RF cable and so all depth measurements are taken from this point. This is to say that the cable/antenna connection is henceforth considered as 0cm when measuring depth as shown in Figure 6.6. Distances measured from this point will be referred to as *absolute* distances (or depths).

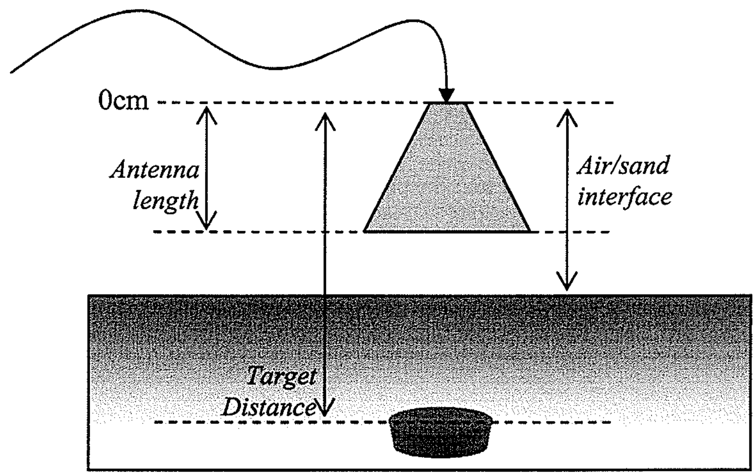

Figure 6.6 The GPR system measures depth from the cable/antenna connection

6.1.4 GPR Targets

Throughout the controlled experiments, several different GPR targets, symmetric and asymmetric, are immersed below the sand in order to test the validity of the symmetry filter algorithm. These targets fall into three categories: weak scatterers made of Styrofoam, strong scatterers made of metal, and lastly, for the sake of authenticity, a rock as a typical naturally occurring target is used.

The collection of weak scatterers consists of two pieces of Styrofoam cut into a cylinder and a rectangle respectively. The shapes and dimensions were chosen to resemble typical geometries of landmines. The cylindrical target, henceforth referred to as *Target A*, is depicted in Figure 6.7, and was chosen to represent the vast array of non-metallic landmines with $C_{\infty a}$ symmetry. The rectangular target, henceforth referred to as

Target B, is depicted in Figure 6.8 and was chosen to approximate non-metallic landmines with C_{2a} symmetry. Styrofoam has a dielectric constant of $\varepsilon_r = 1.03$, which provides some dielectric contrast in the subsurface but can be expected to scatter energy less than metal targets of similar dimensions. These *mine-like* targets will be used to simulate actual landmines.

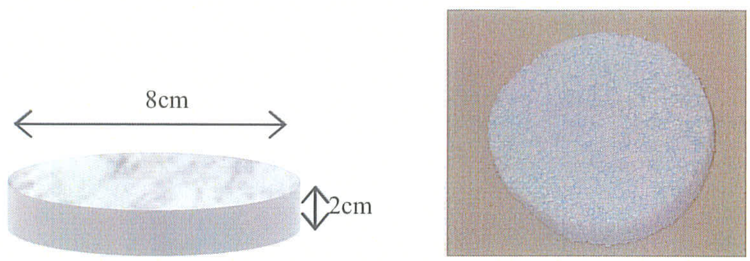

(a) (b)

Figure 6.7 Target A: Styrofoam cylindrical target (a) dimensions, (b) picture

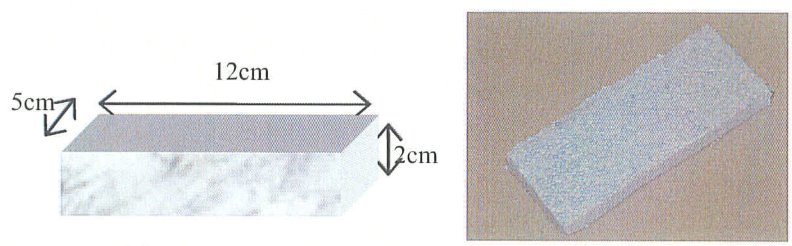

(a) (b)

Figure 6.8 Target B: Styrofoam rectangular target, (a) dimensions, (b) picture

The strong scatterers consist of two shapes cut out of a sheet of aluminium. These are a rectangle and a randomly cut four sided shape. The rectangular metallic scatterer, henceforth referred to as *Target C*, is depicted in Figure 6.9 and is used to test the efficacy of the algorithm for strong scatterers with the C_{2a} symmetric condition. The asymmetric four sided object, hereafter referred to as *Target D*, is meant to represent strongly reflective asymmetric clutter; it is depicted in Figure 6.10.

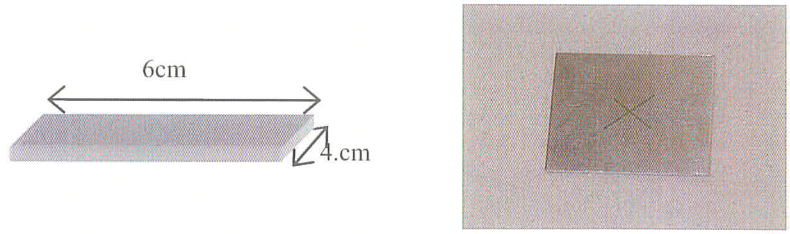

(a) (b)

Figure 6.9 Target C: Metallic rectangular plate target, (a) dimensions, (b) picture

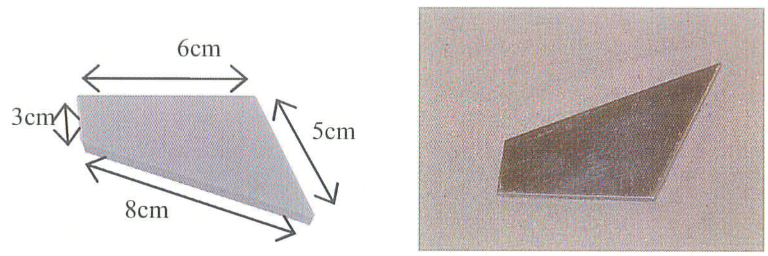

(a) (b)

Figure 6.10 Target D: Metallic asymmetric plate target, (a) dimensions, (b) picture

Finally, the rock target is shown in Figure 6.11 and will henceforth be referred to as *Target E*. The dielectric and conductive properties of this target are unknown, it was simply picked up off the street.

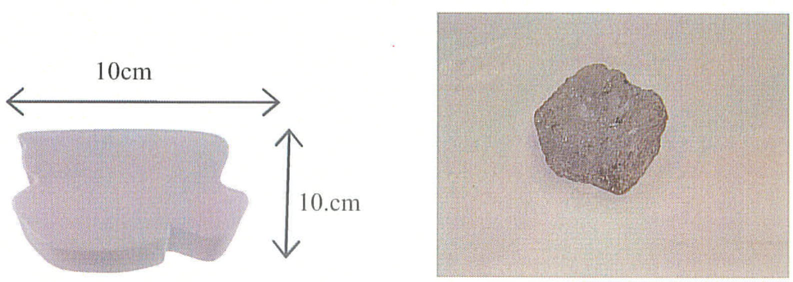

(a) (b)

Figure 6.11 Target E: Rock, (a) dimensions, (b) picture

6.2 Performance of Ω on Symmetric and Asymmetric Conductor Targets (Separate)

In this section targets C and D are submitted to the symmetry filter algorithm on an individual basis. Results of two experiments denoted experiment #1 and experiment #2 are presented to show the effects of symmetry and asymmetry on the symmetry coefficient Ω defined in (4.87).

6.2.1 Experiment # 1

The application of the symmetry filter algorithm begins by analyzing target C on its own, that is to say with no other targets in proximity. The measurements involve the usual three parallel B-scans, scan A, scan B and scan C when the target is positioned as shown in Figure 6.12, where the setup for the particular experiment is depicted. For this experiment, the B-scans consisted of L=50 measurements to give a synthetic aperture of $L\times$1cm=50cm. The separation distance between parallel B-scans was selected to be 5cm and the target was buried at an absolute depth of 49cm, or approximately 15cm below the air/sand interface. The conditions are listed again for clarity in Table 6.2.

Table 6.2 Conditions for experiment #1

Target	Scan Length ($L\times$1cm) [cm]	Absolute Depth (range) [cm]	Location (cross range) [cm]	B-scan separation [cm]	Output Power [dBm]
C	50	48	34	5	5

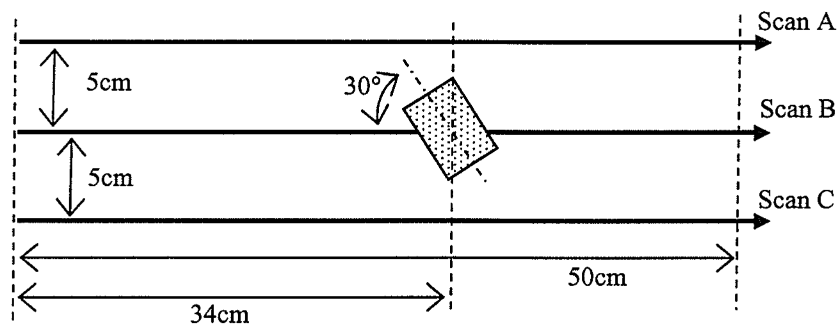

Figure 6.12 Measurement scheme for experiment #1 (Target C)

Note that, despite Target A being rotated 30°, it is still C_{2a} symmetric and the proposed algorithm is designed to take such a situation into consideration.

The centre B-scan (scan B) is shown for this experiment in Figure 6.13 before and after the F-K migration algorithm is implemented. These images represent the extent of classical SAR processing . The color scheme used in the images is such that red implies a response of high amplitude and blue implies a response with a small amplitude. The air/sand interface is evident at 30cm and the target appears where it should in the image, at an absolute depth of 48cm and at 38cm in the cross range. The center scan will be used as a standard henceforth whereby pre-symmetry filtered and post-symmetry filtered data can be compared qualitatively.

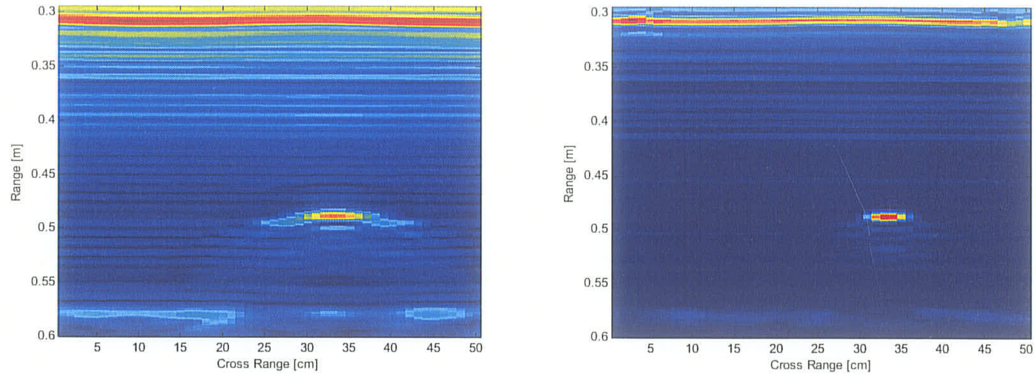

(a) (b)

Figure 6.13 Centre scan for experiment #1, (a) raw B-scan, (b) F-K migration. This is the classical SAR outcome.

The results from the two B-scans on either side of the centre scan are shown in Figure 6.14. Upon inspection, no meaningful information regarding the symmetry is evident in these images. These scans are used to calculate the Ω for this object.

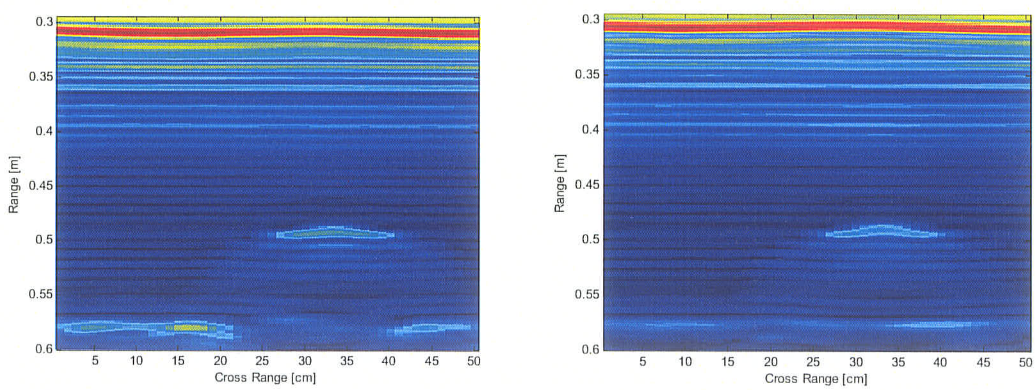

(a) (b)

Figure 6.14 Results for B-scans on either side of the centre scan: (a) Scan A, (b) Scan C

The symmetry filter is applied to the data for experiment #1. Initially a filter window of q=1 is be used. The results are shown in Figure 6.15. In section 4.4 it was stated that the interface between the air and ground will manifest itself as a dominant, highly symmetric response in Ω. This result is evident by the weak image in Figure 6.15(a) where it can be seen that this response is so great that the target symmetry (indicated by the image) is virtually drowned out. Figure 6.15(b) shows the result of Ω when the air/sand interface is not included in the image… the image is "zoomed in" so that the interface does not present itself. Here the target symmetry is more prevalent as seen in the high amplitude response. In Figure 6.15(c), the results of Ω are shown after F-K migration. In all cases the response from the bottom of the sandbox appears to be symmetric at some locations. During the construction of the sandbox, no effort was made to keep the RF foam very flat. This accounts for the variability in the floor symmetry.

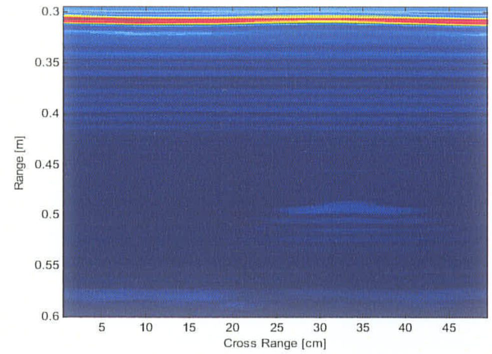

(a)

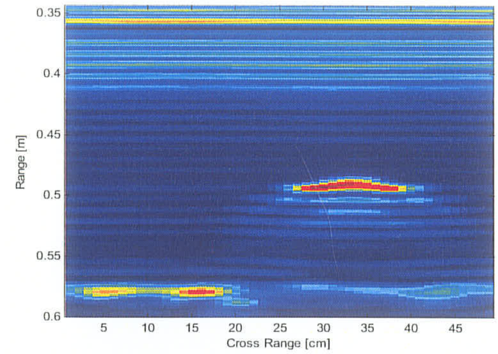

(b)

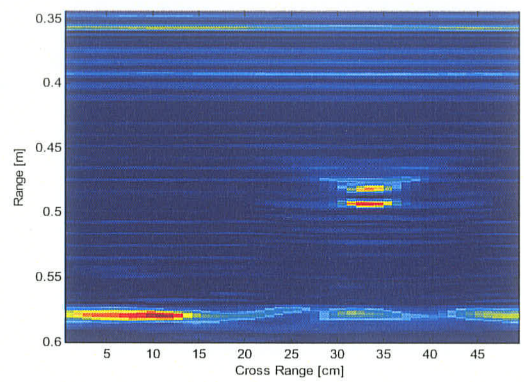

(c)

Figure 6.15 Results of Ω for q=1 for experiment #1: (a) including the ground reflection, (b) neglecting the ground reflection, (c) after F-K migration

The results for various symmetry filter window sizes q are shown in Figure 6.16. For the particular circumstance of a single symmetrical scatterer, one may draw the conclusion from Figure 6.16 that small window sizes result in sharper symmetry images. It is interesting to note another impact of larger values of q. As alluded to earlier in the previous chapter, larger values of q clip off valuable data on either end of the B-scan. We see in Figure 6.16(c) that with q=7, the symmetry response of the target is almost outside the confines of the image.

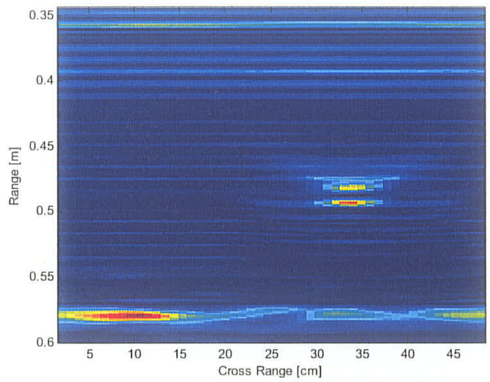

(a)

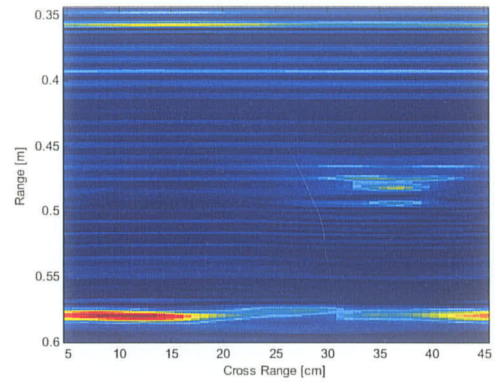

(b)

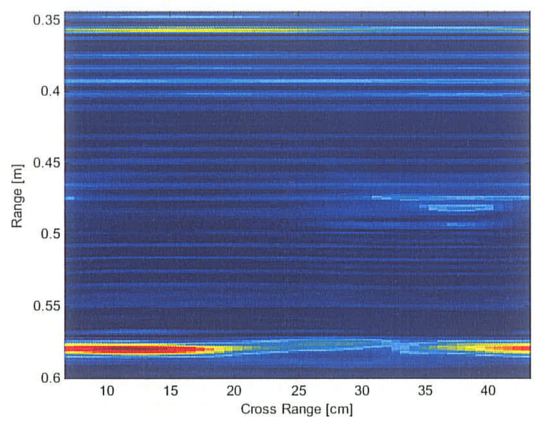

(c)

Figure 6.16 Results of Ω for experiment #1 (post F-K migration) for various filter window sizes: (a) q=2, (b) q=5, (c) q=7

6.2.2 Experiment #2

In this experiment, target D, the metallic target with no relevant symmetry, is submitted to the symmetry filter under similar circumstances as in experiment #1. The target is metallic and therefore can be expected to be highly reflective. The details of the experiment are found in Table 6.3 and the setup is depicted in Figure 6.17.

Table 6.3

Target	Scan Length (L×1cm) [cm]	Absolute Depth (range) [cm]	Location (cross range) [cm]	B-scan separation [cm]	Output Power [dBm]
D	50	47	25	5	5

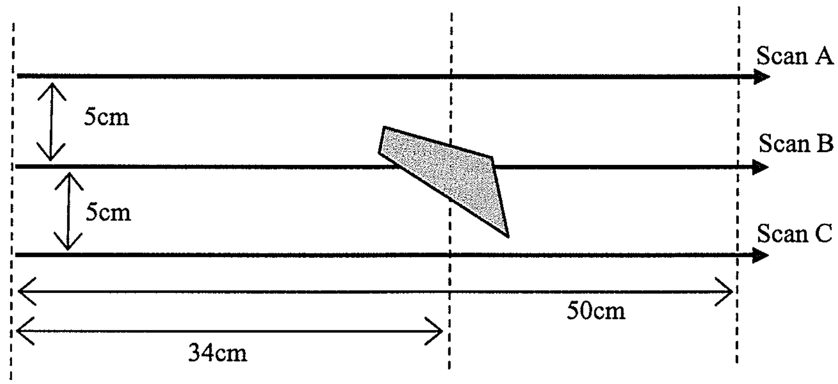

Figure 6.17 Experimental setup scheme for experiment #1 (Target D)

As before, the recorded central B-scan (scan B) is displayed both before and after F-K migration. The corresponding results are shown in Figure 6.18. Comparison between the results shown here and in Figure 6.13 from experiment #1 suggest that the targets appear to behave similarly under the GPR measurement. This is to say that signs of symmetry (or lack thereof) are not obvious by visual inspection.

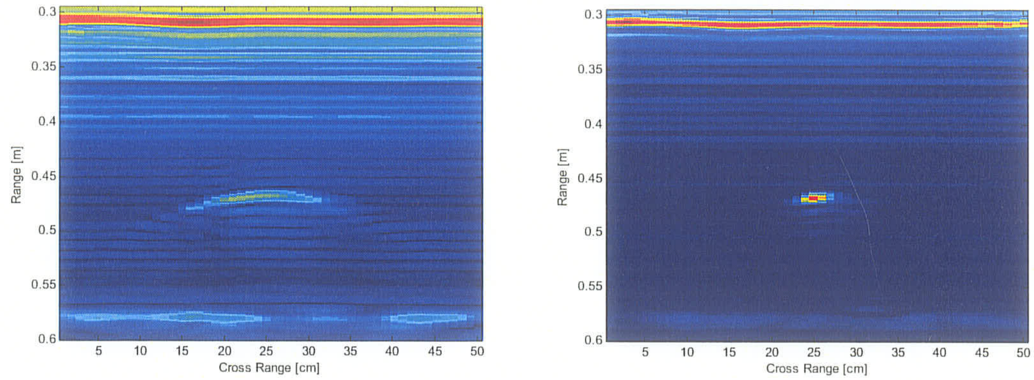

(a) (b)

Figure 6.18 Centre scan for experiment #2, (a) raw B-scan, (b) F-K migration. This is the classical SAR outcome.

The off-centre B-scans, scan A and scan C, are shown respectively in Figure 6.19. Here the effects of the asymmetrical nature of the object become somewhat apparent, and it is clear that the target response appears to differ somewhat between scan A and scan C.

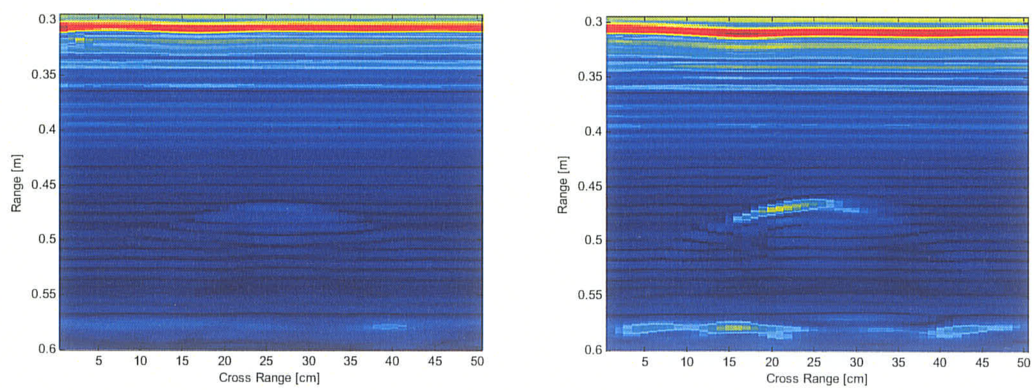

(a) (b)

Figure 6.19 Results for B-scans on either side of the centre scan: (a) Scan A, (b) Scan C

Next, the symmetry filter with a window size of q=1 is applied to the data and the results are shown in Figure 6.20 for the non-migrated and post F-K migration cases. Because of the dominance of the symmetry from the air/sand interface, this region is omitted from the images. It is interesting to compare the results shown in Figure 6.20, for the case of an asymmetrical scatterer, with those shown in Figure 6.15, when the scatterer possesses a relevant symmetry. It is clear that the results of the symmetry filter on target D result in a relatively suppressed response in Ω, with respect to the results obtained with target C in experiment #1.

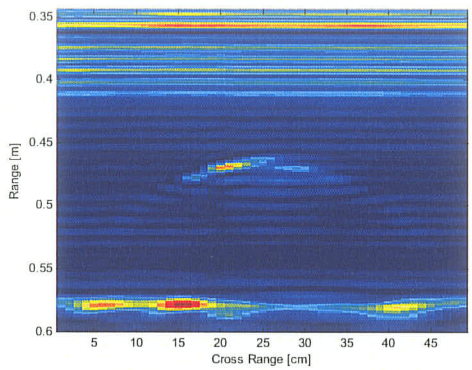

(a)

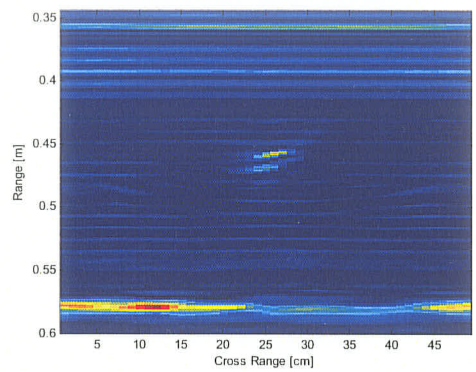

(b)

Figure 6.20 Results of Ω for q=1 for experiment #2 (neglecting the ground reflection): (a) Un-migrated result, (b) post F-K migration result

Finally, the results of the symmetry filter for several other window sizes are shown in Figure 6.21. From these images, it can be seen that, for the asymmetrical conductive target D, higher values of q appear to soften the response of the symmetry filter, as it did in experiment #1 for the case of the symmetric target C.

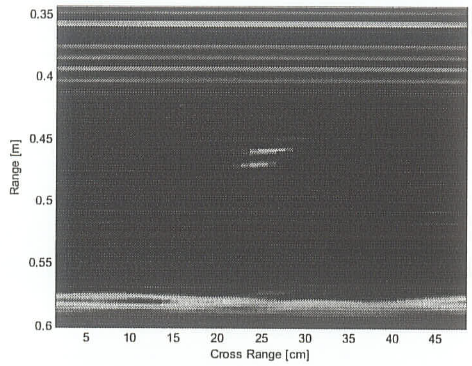

(a)

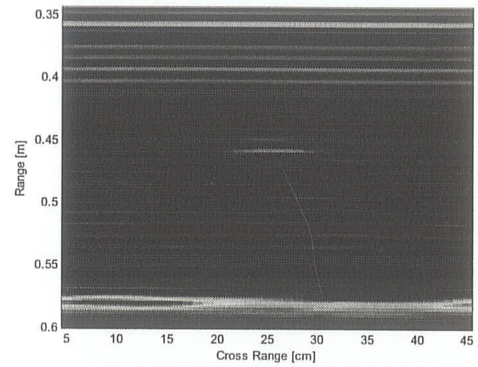

(b)

Figure 6.21 Results of Ω for experiment #2 (post F-K migration) for various filter window sizes: (a) q=2, (b) q=5

6.3 Performance of Ω on Symmetric and Asymmetric Conductor Targets (Mixed)

The efficacy of the proposed symmetry filter algorithm will now be tested for the case when two strong scatterers (symmetric and asymmetric) are located in close proximity to each other. The goal of this experiment is to verify that the algorithm can qualitatively ameliorate an observer's understanding of the symmetry of subsurface targets based on a symmetry filtered image.

6.3.1 Experiment #3

For this experiment, targets C and D are buried next to each other and the results of the filtering are observed to discover if or not the proposed algorithm can indeed yield useful qualitative information regarding target symmetry. The experiment particulars are given in Table 6.4 for this experiment. A corresponding depiction of the experiment is shown in Figure 6.22. The results follow.

Table 6.4 Conditions for experiment #3

Target	Scan Length (L×1cm) [cm]	Absolute Depth (range) [cm] C	Absolute Depth (range) [cm] D	Location (cross range) [cm] C	Location (cross range) [cm] D	B-scan separation [cm]	Output Power [dBm]
C+D	65	45	44	27	48	5	5

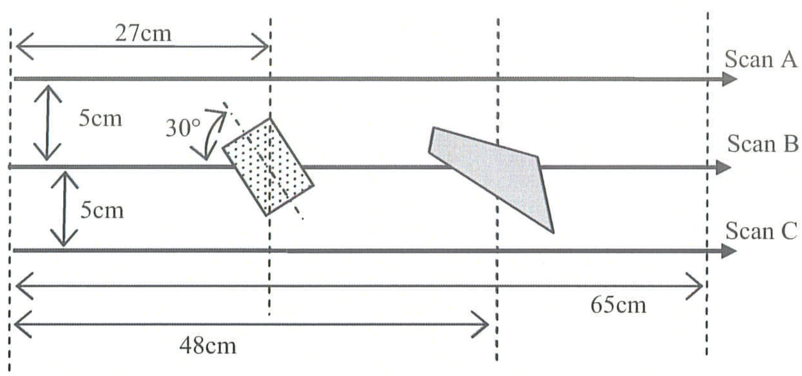

Figure 6.22 Experimental setup scheme for experiment #3

The resulting central B-scan (scan B) for this experiment as well as the results of F-K migration are shown in Figure 6.23.

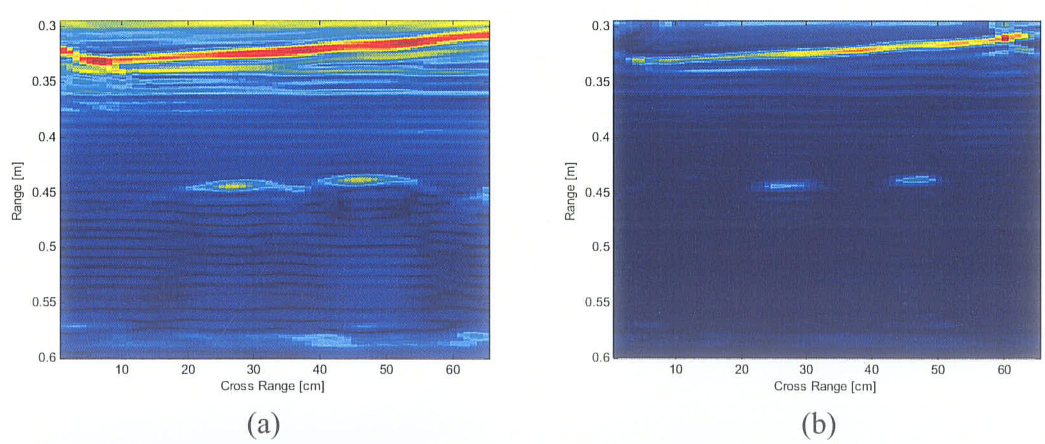

Figure 6.23 Centre scan for experiment #3, (a) raw B-scan, (b) F-K migration.

The two targets are clearly visible; however, no information regarding the symmetry of the buried scatterers is apparent. The application of the symmetry filter algorithm for various window size q are shown in Figure 6.24. In this figure, the post F-K migration results of the symmetry filtered data are given, which shows that the C_{2a} symmetric target C is now visibly dominant as compared to the asymmetric target D.

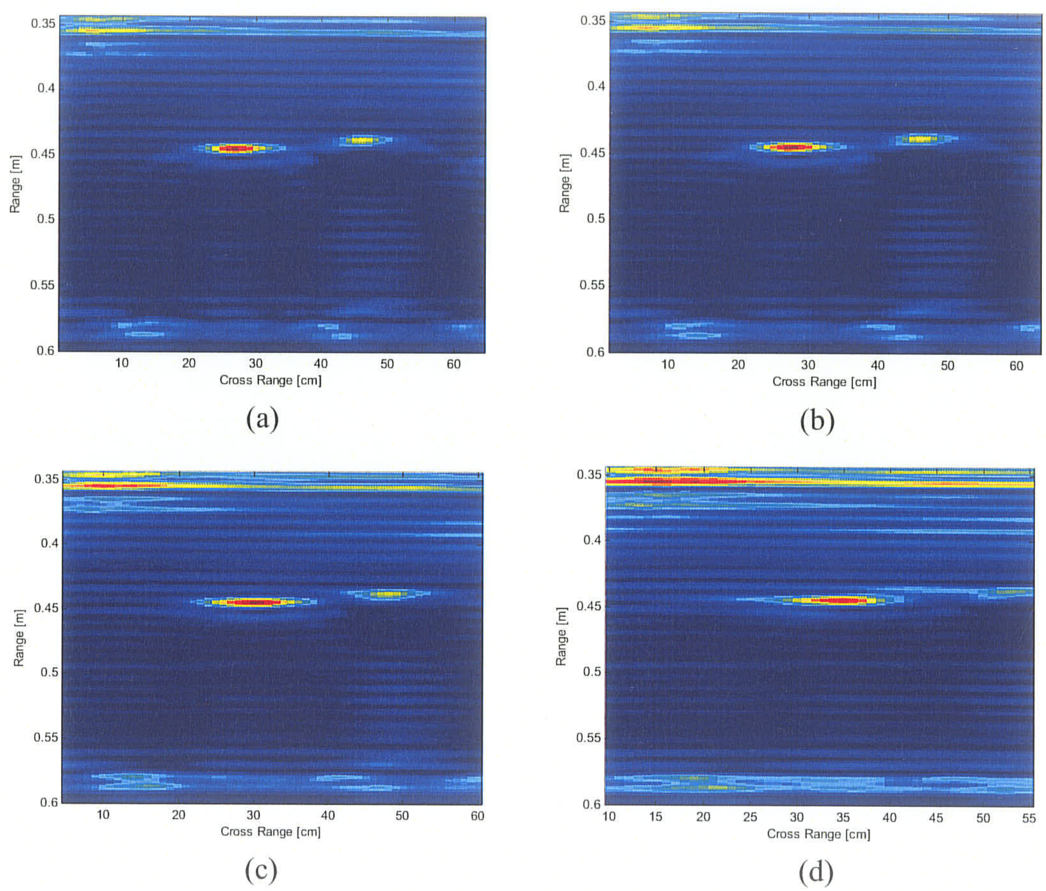

Figure 6.24 Results of Ω after F-K migration for various window sized q for experiment #3 (neglecting the ground reflection): (a) q=1, (b) q=2, (c) q=5, (d) q=10

The results indicate that the symmetry coefficient Ω favours the symmetric target over the asymmetric target. The strongest response for target C relative to the asymmetric scatterer target D appears to be in Figure 6.24(c) when the window size is q=5. This window size is approximately on the order of the target size. It can be seen in Figure 6.24(d) that for a window size of q=10, the image information regarding target D is clipped and some useful information is lost. However the general results from Figure 6.24 indicate that the symmetry filter has effectively enhanced the symmetrical target with respect to the asymmetric target for the case of strong subsurface scatterers.

6.4 Performance of Ω on Symmetric Mine-like Targets and Asymmetric Conductor Targets

The main goal of this thesis is to propose a method for improving subsurface GPR images by exploiting target symmetry for landmine clearance. In this section, the effectiveness of the symmetry filter for mine-like targets will be investigated, to discover whether or not Ω can differentiate between weak symmetrical mine-like scatterers and asymmetrical strong "clutter" scatterers.

6.4.1 Experiment # 4

In this experiment, targets A and B are buried in close proximity to each other and the asymmetric metallic scatterer target D is also buried to emulate typical metallic clutter that may present itself in GPR images. The experimental details are outlined in Table 6.5 and the setup is depicted in Figure 6.25.

Table 6.5 Conditions for experiment #4

Target	Scan Length (L×1cm) [cm]	Absolute Depth (range) [cm]			Location (cross range) [cm]			B-scan separation [cm]	Output Power [dBm]
		A	B	D	A	B	D		
A+B+D	100	41	42	45	23	52	73	5	5

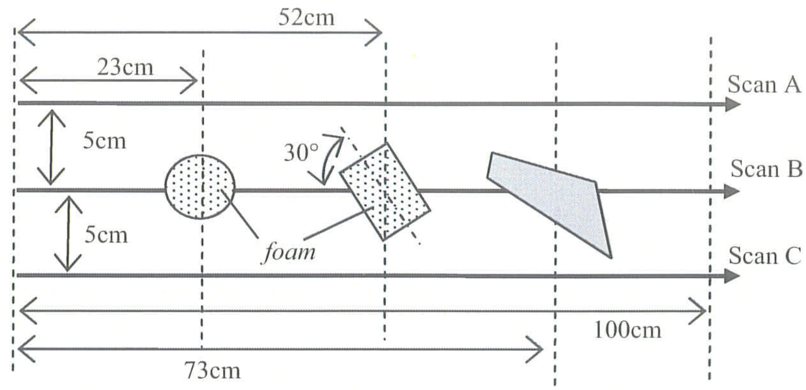

Figure 6.25 Experimental setup scheme for experiment #4

The results of the initial central B-scan are shown in Figure 6.26, both before and after F-K migration. As expected, the response from target D is dominant, because it is a strong scatterer while targets A and B are weak scatterers. Again, no evidence of symmetry (or lack thereof) is obvious in these images.

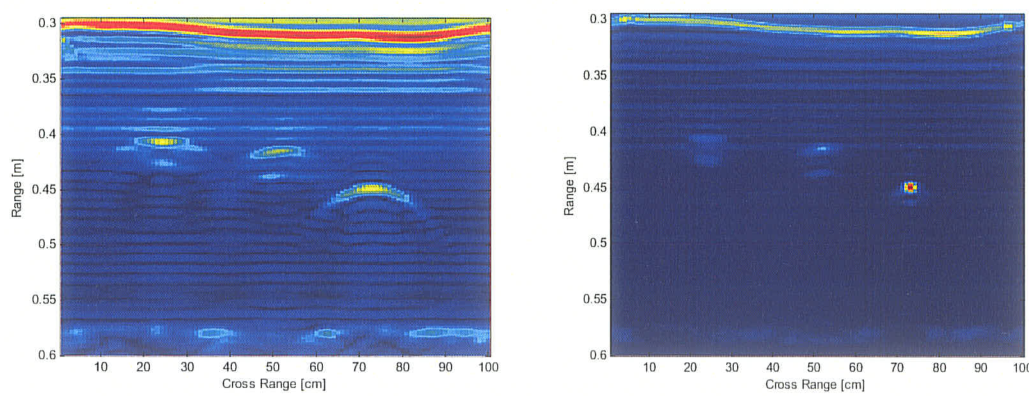

(a) (b)

Figure 6.26 Centre scan for experiment #4, (a) raw B-scan, (b) F-K migration.

The results of applying the symmetry filter are presented for this problem in Figure 6.27 where it can be seen that, for a window size of q=1, the dominance of the response from target D is no longer significant. When the window size is increased to q=5, the response from the strong scatterer is substantially subdued, and the response from the symmetric mine-like foam targets A and B are enhanced considerably with respect to target D.

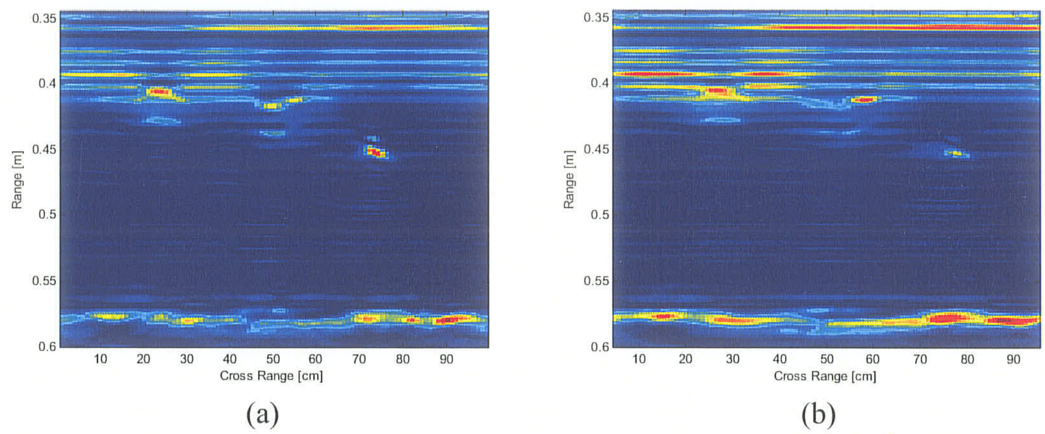

Figure 6.27 Results of Ω after F-K migration for various window sized q for experiment #4 (neglecting the ground reflection): (a) q=1, (b) q=5

This experiment was meant to replicate the problem of strong scattering random clutter betwixt symmetric mine-like targets. The proposed symmetry filter algorithm appears to successfully enhances the response of weak symmetric scatterers in the presence of strong asymmetric scatterers.

6.5 Performance of Ω on Symmetric Mine-like Targets and Asymmetric Rocks

Metallic objects are not the only scatterers that one might find in the subsurface. Another weaker scattering variety is far more prevalent and will be the focus of the following experiment. In this experiment, the validity of the proposed algorithm will be tested in the case when weak scattering, mine-like objects are in proximity to a rock.

6.5.1 Experiment # 5

In this experiment the rock, target E, is located in the subsurface next to the mine-like targets A and B as described in Table 3.1. The depiction of the experiment is shown in Figure 6.28. The purpose of this experiment is to verify the validity of the symmetry filter for the common case when mine-like targets are located near naturally occurring phenomena like target E.

Table 6.6 Conditions for experiment #5

Target	Scan Length ($L\times1$cm) [cm]	Absolute Depth (range) [cm] A	B	E	Location (cross range) [cm] A	B	E	B-scan separation [cm]	Output Power [dBm]
A+B+E	110	42	42	41	29	58	80	5	5

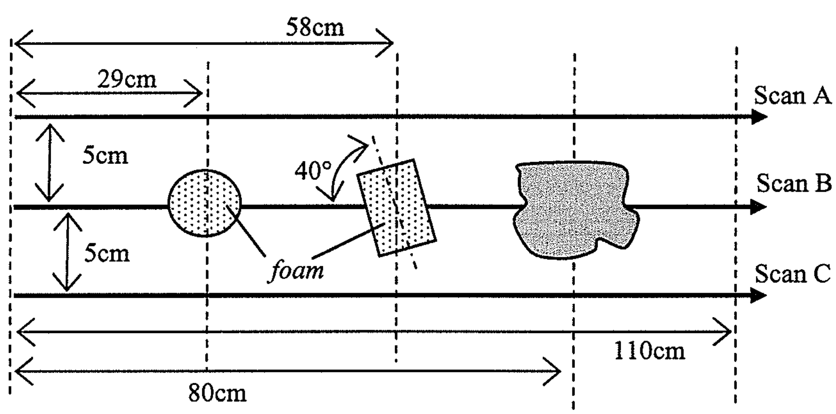

Figure 6.28 Experimental setup scheme for experiment #5

The central B-scan is shown in Figure 6.29, where it is observed that the mine-like targets A and B have signatures with similar amplitudes as the rock, target E. Also noticeable is the fact that target E appears to have two separate responses located one on top of the other. This can be attributed to scattering from the top and the bottom of the rock, which is somewhat larger in size than the targets A and B. This indicates that the rock initially reflects some of the impinging signal, but allows some signal to pass into it where it is again reflected at the bottom of the rock. Again, no noticeable symmetry evidence is apparent from these images.

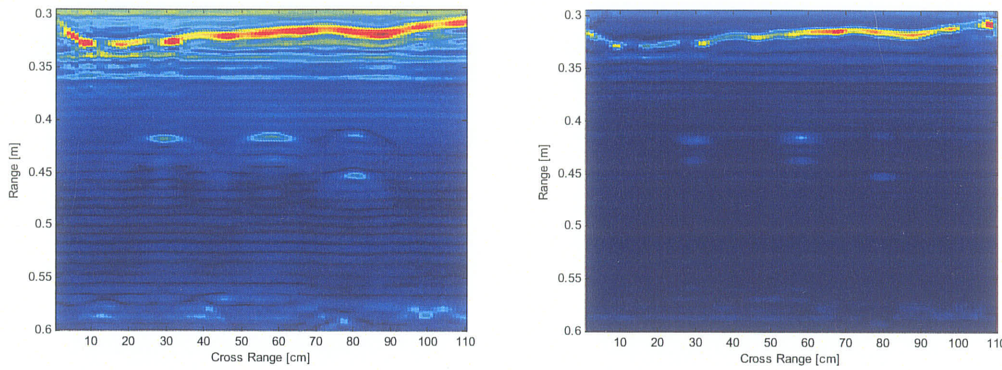

(a) (b)

Figure 6.29 Centre scan for experiment #4, (a) raw B-scan, (b) F-K migration.

In Figure 6.30 the effects of the symmetry filter after F-K migration can be seen for filter window sizes q=1 and q=5. It is apparent that target E is effectively eliminated from visual sight.

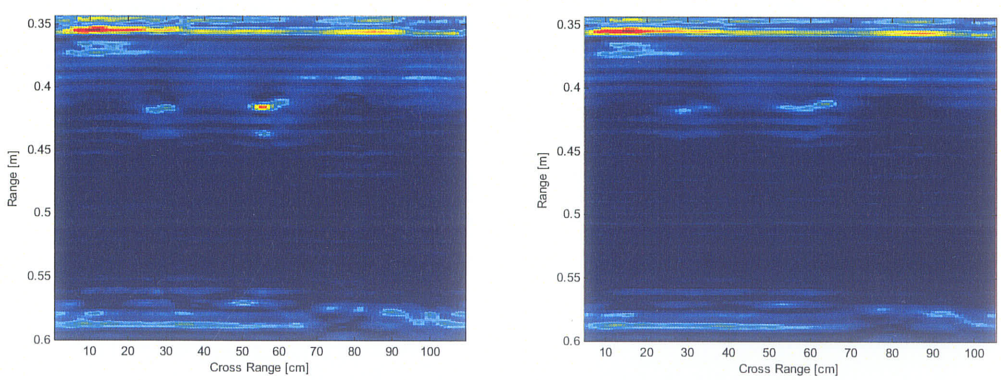

(a) (b)

Figure 6.30 Results of Ω after F-K migration for various window sized q for experiment #5 (neglecting the ground reflection): (a) q=1, (b) q=5

The effects of window size appear to be such that the mine-like responses are sharper for q=1 in Figure 6.30(c); however, the target signatures are still evident with the larger window q=5 in Figure 6.30(b). In both images, the existence of target E is virtually concealed. This experiment shows that the symmetry filter can effectively enhance the presence of mine-like targets in an image while successfully quelling asymmetric naturally occurring weak scatterers such as rocks.

CHAPTER 7
Conclusions

7.1 Summary of Theory

The main hypothesis of the research contained in this thesis as stated in (1.1) is that landmines are synthetic objects created in a human environment, they usually possess some spatial symmetry, whereas subsurface phenomena of less interest such as rocks and shrapnel are generally asymmetric in nature. The symmetry in landmines is invariant in size and composite materials and therefore presents itself as a potentially viable feature that may exploited effectively to differentiate between landmines and common subsurface clutter. An efficient method of analysing and exploiting symmetry is a mathematical tool called Group theory.

Group theory is not a new concept and its roots in applied and theoretical physics are well documented. It is a mathematical tool that allows for in depth analysis of symmetry and its physical ramifications. The application of group theoretical methods in classical electromagnetics is relatively new and its consequences in this field are promising. In this thesis, it has been shown that symmetry in electromagnetic scattering can be described in detail by considering its consequences in the dyadic Green's function. The group operations of the point symmetry groups that consist of reflections and rotations have particular relevance in radar scattering problems involving scattering from symmetric objects. Symmetrical operations implemented by matrix representations of symmetry groups that correspond to point symmetry groups can be implemented on the dyadic Green's function of a subsurface target problem, such that the measured response will be invariant with respect to the symmetry operation. In general, asymmetrical objects cannot be expected to be invariant to these operations. The distinction between the response of a symmetrical subsurface target and an asymmetrical subsurface target with respect to a group symmetry operation can be used to construct images from GPR data that reflect the symmetry or lack thereof in the subsurface scattering.

A symmetry filter algorithm has been formulated and implemented in Matlab© to compute images from the symmetry coefficient Ω, which quantifies symmetry in the subsurface, that is calculated from parallel B-scans according to the methods discussed in Chapter 5. The algorithm has several limiting requirements: targets must posses an even ordered axial symmetry C_{2Ka} (K= 1, 2,…,∞), and the symmetry axis must be perpendicular to a flat air/ground interface in order for the algorithm to work effectively. In addition, the symmetrical object must be centered perfectly between two parallel B-scans in order to extract the information required to construct the symmetry coefficient Ω. However, the proposed algorithm has several advantages over conventional GPR methods of landmine imaging. The symmetry filtered images are function of symmetry rather than of target reflectivity so that even asymmetric clutter with very strong signatures in GPR images are reduced so that the response from the much weaker, symmetric scatterers becomes dominant. Furthermore, no presumed knowledge about target location is required as long as it is centered between two parallel B-scans and has an axis of symmetry perpendicular to the air/ground interface. This assumption is limiting, however it is hoped that future research may relax this condition so that the position of the target is not needed to be known in any dimension.

7.2 Findings and Results

The symmetry filter algorithm was put to the test in Chapter 6 when several experiments designed to simulate a variety of GPR problems were performed. These included the analysis of symmetric and asymmetric metallic scatterers alone and in proximity to one another, weak scattering mine like symmetric objects in proximity to strong scattering metallic clutter and mine-like targets in the presence of natural phenomena in the form of a rock. In all cases, the symmetry filter algorithm enhanced the responses of symmetric targets while quelling the unwanted responses from asymmetric scatterers. The algorithm was implemented with various window sizes q and the results indicated that a dramatic improvement in the GPR image is obtained with the smallest possible window q=1. In some of the more complicated experiments, it appears that a window size on the order of the size of the symmetric scatterer yielded images with a more pronounced contrast between symmetric and asymmetric scatterers in the subsurface. If the window size q is too large, the results become somewhat dampened, and useful information is cropped from the extremities of the B-scans. However, in general, the results appear to confirm the theory and the resulting images appear to be a considerably telling story of the symmetry in the subsurface targets.

7.3 Future Work and Extensions

The inherent restrictions regarding the placement of symmetrical targets and the alignment of their symmetry axes is a significant hurdle in the quest for a fully functional GPR imaging system. The extension of the proposed algorithm to three dimensional imaging via measurements on a full 2D grid is a possible solution to this obstacle. Future research on the subject may lead to eliminating the restriction of target location by increasing the complexity of the algorithm to allow for a symmetric target to be placed arbitrarily under an $N \times N$ grid of B-scans. A more difficult problem will be to eliminate the requirement of the target symmetry axis being perpendicular to the air/ground plane, and for the ground to be smooth and flat. Possible solutions to these issues may require advanced signal processing and/or a deeper understanding of the physical and mathematical principles at work.

The work presented in this thesis has been focused on the particular problem of subsurface GPR imaging for landmine applications. The theory presented may find applications in other related fields where the information regarding the symmetry of observed targets may be useful. For example, in some satellite imagery applications, the observation of terrestrial man made objects may be enhanced through similar arguments. Images of buildings, military installations and ships may be improved by symmetry filter post processing. Another possible application is in sonar where SAR processing is also applicable. Much interest surrounds underwater exploration and the treasures that lie below, such as the dilapidated hulls of shipwrecks on the sea floor embedded betwixt a never ending maze of underwater clutter like rocks and corals.

The future of symmetry filter processing appears to have no shortage of applications and with further research aimed at alleviating its shortcomings, the symmetry filter might one day become an established tool in the imaging sciences.

References

[1] BBC News, "Asia pressed on landmine ban", http://news.bbc.co.uk/1/hi/world/asia-pacific/3109352.stm

[2] M. Soumekh, "Synthetic Aperture Radar Signal Processing With Matlab Algorithms", May 1999
John Wiley and Sons Ltd

[3] H. Blok, M. Oristaglio, "Wavefield Imaging and Inversion in Electromagnetics and Acoustics", (Course Notes), Laboratory of Electromagnetic Research, Delft University of Technology, June 1995

[4] O. M Bucci, L. Crocco, T. Isernia, V. Pasazio, "Subsurface Inverse Scattering Problems: Quantifying, Qualifying and Achieving the available Information", IEEE Trans. On Geoscience and Remote Sensing, Vol.. 37, No. 5, Sept. 1999

[5] N. Budko, R. Remis, P. van den Berg, "Advances in GPR Data Processing for Antipersonnel Landmine Detection", Geoscience and Remote Sensing Symposium, 2000. Proceedings. IGARSS 2000. IEEE 2000 International , Volume: 1 , 24-28 July 2000, Page(s): 19 -22

[6] P.M. van den Berg, A. Abubakar, N.V. Budko, R.F. Remis, "Imaging and Inversion of Buried Objects using GPR", Geoscience and Remote Sensing Symposium, 2001. IGARSS '01. IEEE 2001 International , Volume: 3 , 9-13 July 2001, Page(s): 1377 -1380

[7] P. D. Gader, B. Nelson, H. Frigui, G. Vaillette, J. Keller, "Landmine Detection in Ground penetrating Radar Using Fuzzy Logic", Fuzzy Logic Signal Processing, vol. 80, pp. 1069-1084, June 2000

[8] P. D. Gader, M. Mystkowski, Y. Zhao, "Landmine Detection with Ground Penetrating Radar Using Hidden Markov Models", IEEE Trans. on Geoscience & Remote Sensing, vol. 39, pp. 1231-1224, June 2001

[9] J. A. Craib, "Survey of Mine Clearance Technology for the United Nations University", BARIC (consultants) Ltd., Oct. 1994

[10] C. E. Baum, "Symmetry in Electromagnetic Scattering as a Target Discriminant", Interaction Note 523, Phillips Laboratory, Kirtland AFB, October 1996

[11] D. Collins, C. Gilmore, I. Jeffrey, S. Peters, "Design and Construction of a Ground Penetrating Radar System for use in Landmine Detection", B. Sc. Thesis, University of Manitoba, March 2001

[12] D. Lovelock, H. Rund, "Tensors, Differential Forms and Variational Principles", (Dover publications: New York, 1989)

[13] C. E. Baum, "Target Symmetry and the Scattering Dyadic", Interaction Note 507, Phillips Laboratory, Kirtland AFB, October 1994

[14] S. K. Cho, "Electromagnetic Scattering", (Springer-Verlag: Ney York, 1990)

[15] Morrow, I.L.; van Genderen, P. ,"Effective imaging of buried dielectric objects"; Geoscience and Remote Sensing, IEEE Transactions on , Volume: 40 Issue: 4 , April 2002, Page(s): 943 -949

[16] R.V. de Jongh, A.G.Yarovoy, L.P.Ligthart, I.V.Kaploun, A.D.Schukin, "Design and analysis of new GPR antenna concepts," Proc. 7th Int. Conf. On Ground-Penetrating Radar (GPR'98), May 27-30, 1988, Lawrence, Kansas, USA, Vol.1, pp.81-89.

[17] W. Cai , T. Yu, "Fast Calculations of Dyadic Green's Functions for Electromagnetic Scattering in a Multilayered Medium" Journal of Computational Physics, November, 1999. Revised April 27, 2000

[18] T. Søndergaard, D. Lenstra, B. Tromborg, "Near-fields and far-fields generated by sources in the presence of dielectric structures with cylindrical symmetry", Optics Letters, Vol. 26, No. 21, Nov. 1, 2001

[19] J. Appel-Hansen, "Comments on Dyadic Green's Functions and Induced Currents", Electrotechnical Conference, 1996. MELECON '96., 8th Mediterranean , Volume: 3 , 13-16 May 1996, Page(s): 1427 -1428

[20] H. F. Weinberger, "A First Course in Partial Differential Equations", Dover edition, Dover Publications, July 1995

[21] C. Tai, "Dyadic Green Function in Electromagnetic Theory", 2nd edition, IEEE Press, 1994

[22] Bojarski, N., "Electromagnetic inverse scattering", Antennas and Propagation Society International Symposium, 1971 , Volume: 9 , Sep 1971, Page(s): 356 -358

[23] L. Qi, Z. Hongfei, S. Xiaoquan, S. Zhongkang, "Analysis of position location with two coordinate measurements in bistatic system", Radar, 1996. Proceedings., CIE International Conference of , 8-10 Oct. 1996, Page(s): 539 -542

[24] S. A. Levin, "Stolt without artifacts? — dropping the Jacobian", Stanford Exploration Project, Rep. 80, May 15, 2001, pages 1–508

[25] G. F. Margrave, "Numerical Methods of Exploration Seismology with algorithms in MATLAB", Department of Geology and Geophysics, The University of Calgary, January 23, 2001

[26] I. A. Ruthenberg, "Curve Fitting and Migration of GPR Data for the Detection of Pipes and Cables", BSc. Thesis, Dept. of Comp. Sci. & EE, University of Queensland.

[27] I. El-Said, "Islamic Art and Architechture: The System of Geometric Design", (London: Garnet Publishing Ltd., 1993)

[28] R. S. Nelson, "Visuality before and beyond the Renaissance : seeing as others saw", Cambridge, U.K. (New York), NY, USA : Cambridge University Press, 2000

[29] A. V. Shubnikov and V. A. Kopstik, "Symmetry in Science and Art", New York: Plenum Press (Translated from Russian Eddition, Moscow: Nauka, 1972)

[30] S. Graham, "In Search of Antimatter", Scientific American, August 20, 2001

[31] Richman, M.S.; Parks, T.W.; Shenoy, R.G., "Features of a discrete Wigner distribution", Digital Signal Processing Workshop Proceedings, 1996., IEEE , 1-4 Sept. 1996 Page(s): 427 -430

[32] Rubin, H., "Symmetric basis functions for networks with arbitrary geometrical symmetries" Circuits and Systems, IEEE Transactions on (legacy, pre – 1988) , Volume: 18 Issue: 5 , Sep 1971, Page(s): 547-49

[33] C. E. Baum and H. N. Kritikos, Electromagnetic Symmetry. (New York), Taylor & Francis, 1995.

[34] J. M. Stiles et. al., "A group Theoretic Analysis of Symmetric Target Scattering With Application to Landmine Detection", IEEE Trans on Geoscience and Remote Sensing, Vol. 40, No. 8, August 2002

[35] J. F. Cornwell, "Group Theory in Physics", Academic press, Harcourt Brace & Company, 1997

[36] Roman, S., "An Introduction to Linear Algebra", Springer-Verlag, 1993

[37] C. E. Baum, "Interaction of Electromagnetic Fields with an Object which has an Electromagnetic Symmetry Plane", Interaction Note 63, Air Force Research Laboratory (Directed Energy Directorate), March 1971

[38] Baum, C. E., "Symmetry Analysis of Targets Near an Earth/Air Interface", Interaction Note 554, Air Force Research Laboratory (Directed Energy Directorate), March 1999

[39] C. E. Baum, "Target Symmetry and the Scattering Dyadic", Interaction Note 507, Phillips Laboratory, Sept. 1994

[40] Norwegian Peoples Aid Landmine Database, http://www.angola.npaid.org/

Appendix A

```
%Code for preparing data for symmetry filtering
clear all; close all; clc
%------------------------------
%------------------------------
%Relevent system parameters
y='filename1' %load relevent B-scan (must be repeated for each B-scan)
Bscan=load(y);
%Build B-scan image: the file is composed of interlaced real and imaginary
%parts that must be combined into the complex domain
[N_f  N_IQ]=size(Bscan);
n=1:2:(N_IQ-1);
m=2:2:N_IQ;
Bscan_I=Bscan(:,n);
Bscan_Q=Bscan(:,m);
Bscan_complex=Bscan_I+j*Bscan_Q;
 [Ns NL]=size(Bscan_complex);
%==================================
c=3e8;              %free space propagation velocity
Er=2.4;             %Dielectric constant of medium
c=c/sqrt(Er);         %medium propagation velocity
fl=1e9; fu=12.4e9;     %System frequency limits
BW=fu-fl;             %System bandwidth [Hz]
df=BW/Ns;              %frequency step [Hz]
dR=c/(2*BW);            %Range resolution
zeropad=8;             %zeropadding in the range direction
dd=.01;               %SAR measurement interval [m]
d=linspace(0,501*dR,zeropad*501);  %antenna position vector
Xmax=0.45; Xmin=0.15;     %Minimum and maximum distances of desired range swath
Nmax=ceil(Xmax/dR);    %Maximum range index
Nmin=floor(Xmin/dR);   %Minimum range index
%
%------------------------------
%------------------------------
%Read calibration measurement
Uncal_open=load('uncal_open2.txt');  %Open circuit measurement
[na nb]=size(Uncal_open);
Uncal_open=Uncal_open(:,1)+j*Uncal_open(:,2);
%===============================
%Calibration of RF cable
 [Nf_Uncal   Na]=size(Uncal_open);
D=sva_matrix(Uncal_open, Na ,Nf_Uncal);
[s I]=max(abs(D));
%=================================
```

```
%================================
Bscan_complex=Bscan_complex';
for V=1:NL;
   Bscan_complex2(V,floor(fl/df)+1:floor(fl/df)+Ns)=Bscan_complex(V,:);
end
Bscan_complex2=Bscan_complex2';
Bscan_complex=Bscan_complex';
%================================
%================================
 [Na Nb]=size(Bscan_complex2);
%Construction of GPR image
Bscan_image=(ifft(Bscan_complex2,zeropad*Ns));
Bscan_total_image=circshift(Bscan_image,-I*zeropad);     %Phase calibration of cable
%Reduction to desired range swath
Bscan_swath_image=Bscan_total_image(Nmin*zeropad:zeropad*Nmax,:);
save filename(2,3) Bscan_total_image; %Requires 2 B-scans: filename2 & filename3
%================================
%================================
%================================
%Symmetry Filter Code
%================================
load filename2; L5=Bscan_total_image;
load filename3; R5=Bscan_total_image;
scan_max=10*mean(mean(abs(R5+L5)));
[Range Xrange]=size(L5);
Fmax=1;     %Filter width [cm];
Sp=0; Sn=0; Ps=0;
for F=1:Fmax;
   for n= F : Xrange-F;
      Spos(:,n)=L5(:,n-F+1)+R5(:,n+F-1);
      Sneg(:,n)=L5(:,n-F+1)-R5(:,n+F-1);
      Psym(:,n)=(abs(Spos(:,n)));
   end
   Spos=Spos(:, F : Xrange - 2*Fmax+F);
   Sneg=Sneg(:, F : Xrange - 2*Fmax+F);
   Psym=Psym(:, F : Xrange - 2*Fmax+F);
   Sp=Sp+Spos;
   Sn=Sn+Sneg;
   Ps=Ps+Psym;
   clear Spos Sneg Psym;
end
%
figure; imagesc([Fmax Xrange-Fmax],[Nmin*dR+0.15
Nmax*dR+0.15],(abs(Ps(Nmin*zeropad:zeropad*Nmax,:)).^2)); %title('Ps');
xlabel('Cross Range [cm]');
ylabel('Range [m]')
```

```
figure; imagesc([Fmax Xrange-Fmax],[Nmin*dR Nmax*dR],
(abs(Ps(Nmin*zeropad:zeropad*Nmax,:)).^2));
xlabel('Cross Range [cm]');
ylabel('Range [m]')
%
%
%The following is required for migration only
clear Bscan_total_image
Ps=Ps';
for V=1:NL-2*Fmax+1;
   Ps2(V,floor(fl/df)*zeropad+1:floor(fl/df)*zeropad+Ns*zeropad)=Ps(V,:);
end
Ps2=Ps2';
Ps=Ps';
Bscan_total_image=(Ps);
Bscan_total_image(1:zeropad*Nmin-1,:)=0;
Bscan_total_image(zeropad*Nmax+1:Ns*zeropad,:)=0;
```